

# Theoretical and Experimental Investigations of the Interaction of Proteins and Nanoparticles with Biological Membranes

Zur Erlangung des akademischen Grades eines

DOKTORS DER NATURWISSENSCHAFTEN

von der Fakultät für Physik des  
Karlsruher Institut für Technologie (KIT)

genehmigte

DISSERTATION

von

Dipl.-Phys. Julia Christine Setzler  
aus Baden-Baden

Tag der mündlichen Prüfung: 8. November 2013

Referent: **Prof. Dr. Wolfgang Wenzel**

Korreferent: **Prof. Dr. Gerd Schön**



# Deutsche Zusammenfassung

Proteine sind hoch komplexe Biomoleküle, die viele biologische Prozesse in lebenden Organismen ermöglichen oder regeln. Sie bestehen aus einer Kette verschiedener Aminosäuren, die meist in eine einzigartige dreidimensionale Struktur faltet. Neben der Sequenz spielt bei der Faltung auch die physiologische Umgebung des Proteins eine entscheidende Rolle. Durch die einzigartige Struktur der Proteine bilden sich aktive Zentren und Oberflächen, die Wechselwirkungen mit anderen Proteinen oder Molekülen ermöglichen, welche wiederum Strukturveränderungen der Proteine hervorrufen können. Dadurch können Proteine viele verschiedene Funktionen wie beispielsweise die Katalyse von biochemischen Reaktionen, Signalübermittlung, Stofftransport oder die Bewegung von Muskeln ausführen. Fehlfaltungen oder Mutationen können die Funktion von Proteinen beeinträchtigen, was zum Beispiel zu Krankheiten wie Alzheimer oder Krebs führen kann. Um die Funktion oder auch Fehlfunktion von Proteinen zu verstehen, ist daher die Kenntnis ihrer Struktur von großer Bedeutung. Dies kann zur Entwicklung neuer Medikamente und Therapien genutzt werden.

Experimentelle Methoden wie NMR-Spektroskopie oder Röntgen-Kristallographie können zur Strukturaufklärung von Proteinen beitragen. Allerdings schränken notwendige experimentelle Bedingungen wie das Nachbilden physiologischer Bedingungen oder das Vorhandensein einer Kristallstruktur die Möglichkeiten ein. Außerdem liefern solche Experimente meist nur statische Momentaufnahmen und sind deshalb für das Verständnis dynamischer Prozesse unzureichend.

Computersimulationen stellen eine weitere Möglichkeit zur Untersuchung von Proteinstrukturen dar und können auch bei dynamischen Prozessen zu wertvollem Erkenntnisgewinn führen. Weit verbreitet sind dabei Verfahren der Molekulardynamik, die das Protein mit Hilfe eines klassischen Kraftfeldes

beschreiben. Solche Kraftfelder sind ein fundamentaler Bestandteil der 2013 mit dem Nobelpreis in Chemie gewürdigten Multiskalen-Modellierung atomarer Systeme. Ein Nachteil von Molekulardynamik-Simulationen sind die benötigten Zeitschritte, die normalerweise im Bereich einer Femtosekunde liegen. Da sich biologische Prozesse auf wesentlich längeren Zeitskalen abspielen, sind sehr viele Simulationsschritte nötig, um diese Zeitskalen zu erreichen. Die hohe benötigte Rechenleistung kann dabei durch implizite Lösungsmittelmodelle reduziert werden, welche die Wechselwirkungen eines Systems mit seiner Umgebung durch ein zusätzliches Potential modellieren.

Eine Alternative zu Molekulardynamik-Simulationen sind Monte-Carlo-Simulationen, mit denen sich thermodynamische Eigenschaften anhand eines repräsentativen Ensembles bestimmen lassen. Da diese Methode das Zeitschrittproblem von Molekulardynamik-Simulationen umgeht, kann sie zu einer erheblichen Einsparung von Rechenzeit führen.

Etwa 20 - 30% aller Proteine haben als physiologische Umgebung eine biologische Membran. Diese sind zusammengesetzt aus amphiphilen Lipiden, die eine Lipiddoppelschicht bilden. Membranen sind die natürliche Barriere einer Zelle und sorgen für den kontrollierten Austausch zwischen Zellinnerem und der äußeren Umgebung. Fehlfunktionen oder Beschädigung dieser natürlichen Barriere führen zum Tod der Zelle. Normalerweise ist die Zerstörung der Membran unerwünscht, jedoch basiert die Wirkung bakterizider Antibiotika oder antimikrobieller Peptide auf diesem Effekt. Letztere stellen eine vielversprechende Alternative zu Antibiotika dar, welche durch zunehmende Resistenz von Bakterien immer wirkungsloser werden.

Neben der natürlichen Barriere ist die selektive Struktur einer Membran überlebenswichtig, die durch bestimmte Membranproteine geregelt wird. Ein Beispiel für solch ein Protein ist der hERG-Kanal, der durch den geregelten Fluss von Kalium-Ionen für eine normale Herzaktivität beim Menschen sorgt. Da Nebenwirkungen vieler Medikamente auf die Beeinträchtigungen dieses Kanals zurückgeführt wurden, müssen potentielle neue Wirkstoffe vorklinisch auf Wechselwirkungen mit ihm untersucht werden. So zeigten Untersuchungen mit Goldnanoteilchen überraschenderweise, dass diese unter bestimmten Bedingungen diesen Kanal blockieren können. Da Goldnanoteilchen als Kontrastmittel, Wirkstofftransporter oder Therapeutika vielversprechende Kandidaten für biomedizinische Anwendungen darstellen,

---

---

müssen solche Nebenwirkungen näher untersucht werden, bevor Goldnanoteilchen ohne Bedenken angewandt werden dürfen.

Leider ist das Wissen über die Wechselwirkungen von Goldnanoteilchen oder anderen Molekülen mit Membranproteinen, oder auch Membranen selbst, noch sehr begrenzt, weshalb Experimente mit künstlichen Membranen, sogenannte Black Lipid Bilayer Experimente, das Verständnis vertiefen können.

Um auch die zugrunde liegenden atomaren Mechanismen zu verstehen, können Computersimulationen Experimente unterstützen und ergänzen. Doch auch hier stellt die komplexe Struktur einer Membran eine große Herausforderung bei der Simulation von Membranproteinen dar. Der hohe Rechenaufwand durch die Berücksichtigung jedes einzelnen Atoms einer Membran schränkt die Zahl der untersuchbaren Prozesse stark ein.

Das erste Ziel der hier vorliegenden Arbeit ist die Entwicklung neuer computergestützter Methoden, die die Beschränkungen aufgrund des enormen Rechenaufwands von Molekulardynamik-Simulationen umgehen. Neue Monte-Carlo basierte Simulationsprotokolle, an denen ich mitgearbeitet habe, werden in dieser Arbeit validiert. Zusammen mit Martin Brieg und Carolin Seith habe ich im Rahmen dieser Dissertation ein neues implizites Membranmodell entwickelt, parametrisiert und validiert.

Ein weiteres Ziel war die Kombination von experimentellen und theoretischen Untersuchungen, um Wechselwirkungen zwischen Wirkstoffkandidaten und Membranen oder Membranproteinen besser zu verstehen. Neben Black Lipid Bilayer Experimenten, in denen der Einfluss von Goldnanoteilchen auf Membrane untersucht wurde, habe ich auch die Blockierung des hERG-Kanals durch Goldnanoteilchen in Simulationen untersucht.

Alle Simulationen, die in dieser Arbeit beschrieben werden, wurden mit dem Monte-Carlo-Simulationspaket SIMONA durchgeführt. Im Vergleich zu expliziten Molekulardynamik-Simulationen werden in SIMONA nur Änderungen der Dihedralwinkel, aber keine Änderung der Bindungslängen oder Bindungswinkel als Freiheitsgrade genutzt. Nach der Implementierung eines Dihedralpotentials und zusätzlichen Dihedralfreiheitsgraden für die Seitenketten von Aminosäuren habe ich die Freie Energie-Landschaft für

Dipeptide untersucht. Diese Simulationen zeigen die erwarteten Minima in der Freien Energie, welche mit den charakteristischen Winkeln für die Sekundärstruktur in Proteinen korrespondieren und mit Daten aus der Literatur vergleichbar sind. Ein direkter Vergleich zu expliziten Molekulardynamik-Simulationen zeigt gute Übereinstimmung in der Nähe der Minima, jedoch steilere Barrieren in den Monte-Carlo-Simulationen, welche durch die zusätzlichen Freiheitsgrade der Änderung von Bindungslängen und Bindungswinkel in der Molekulardynamik erklärt werden können. Durch diese kann die Überlappung von Lennard-Jones-Radien vermieden werden.

Um die Stabilität der Tertiärstruktur im neuen SIMONA Kraftfeld zu testen, habe ich verschiedene kleine Proteine untersucht; erste Ergebnisse dieser Simulationen für das Villin Headpiece und die WW-Domäne werden in der Arbeit vorgestellt. Diese beiden Proteine wurden aufgrund ihrer unterschiedlichen Sekundärstruktur ausgewählt und zeigen beide eine Stabilisierung des nativen Zustandes bei niedrigeren Temperaturen und sowohl Entfaltungs- als auch Faltungseignisse bei höheren Temperaturen. Die Bestimmung der Faltungstemperatur hat sich dabei als schwierig herausgestellt, weshalb zukünftig Methoden wie „Parallel Tempering“ eingesetzt werden sollten, um diese Problem zu beheben. Weiterhin haben meine Simulationen gezeigt, dass zwischen experimentell ermittelter Faltungstemperatur und der aus Simulationen bestimmten Faltungstemperatur Unterschiede bestehen. Diese sollten in Zukunft genauer untersucht werden.

Eine mögliche Fehlerquelle, die diesen Temperaturunterschied verursachen kann, stellt dabei das implizite Lösungsmittel dar. Der letzte Abschnitt in Kapitel 3 beschreibt deshalb den Vergleich von drei verschiedenen Modellen für den nichtpolaren Anteil der freien Lösungsenergie bei der Berechnung von Hydratationsenergien kleiner Moleküle. Dieser Beitrag ist wichtig in Anwendungen der Medikamentenentwicklung und der Bestimmung der Bindungsaffinität eines Liganden zu seinem Zielprotein. Um einen fairen Vergleich der Modelle zu gewährleisten, wurden alle freien Parameter der Modelle optimiert. Meine Analyse zeigt, dass implizite Modelle sogar explizite Wassermodelle in der Genauigkeit übertreffen können und dass Elemente, die sowohl negative als auch positive Partialladungen in Molekülen tragen können, eine große Fehlerquelle für implizite Modelle darstellen [1]. Um diese Erkenntnisse in SIMONA nutzen zu können, sollte in weiteren Untersuchungen geklärt werden, ob die Genauigkeit der Modelle auch auf größere Moleküle wie Proteine übertragen werden kann.

---

---

Da Membranproteine für viele biologische Prozesse sehr wichtig sind, jedoch die komplexe hydrophobe Umgebung experimentelle und computergestützte Untersuchungen erheblich erschwert, haben wir ein neues implizites Membranmodell basierend auf dem verallgemeinerten Born-Modell entwickelt. SLIM (SIMONA layered implicit membrane) nutzt Vorteile verschiedener bereits etablierter Modelle und erzielt damit bessere Ergebnisse beim Modellieren elektrostatischer Effekte in der Membran. Kapitel 4 fasst die Idee, sowie Parametrisierung und Validierung dieses Modells zusammen. Anhand von Vergleichen zwischen dem verallgemeinerten Born-Modell aus dem impliziten Membranmodell zu Poisson-Boltzmann-Referenzrechnungen zeige ich die Genauigkeit von SLIM. Alle Eigenschaften der Poisson-Boltzmann-Ergebnisse werden trotz des viel geringeren Rechenaufwands für das verallgemeinerte Born-Modell wiedergegeben. Neben den Selbstenergietermen für einfache und komplexere Moleküle wird auch die Wechselwirkung von geladenen Ionen in der Membran im Vergleich zu Poisson-Boltzmann qualitativ und quantitativ richtig approximiert.

Für die Validierung des Modells habe ich im letzten Abschnitt dieses Kapitels Simulationsergebnisse und Vergleiche zu anderen Modellen oder experimentellen Untersuchungen zusammengefasst. Dafür habe ich zusammen mit der Diplomandin Carolin Seith drei gut untersuchte Membranproteine verwendet. Sowohl die Position des Melittin Proteins relativ zur Membran, als auch Neigungswinkel und Kreuzungswinkel für das M2-Protein und Glycophorin A wurden untersucht. Diese zeigen gute Übereinstimmungen mit Literaturwerten.

Das neue Membranmodell ist also in der Lage, Proteineigenschaften zu reproduzieren und kann deshalb künftig zur Untersuchung vieler interessanter Prozesse verwendet werden [2]. Damit rückt die Untersuchung von Prozessen wie der Proteinassamblierung oder die Wechselwirkung mehrerer Proteine in der Membran in greifbare Nähe und ist nicht mehr durch den zu hohen Rechenaufwand wie bei Molekulardynamik-Simulationen limitiert.

Im experimentellen Teil meiner Arbeit standen Black Lipid Bilayer Experimente mit Goldnanoteilchen im Fokus, die im Labor von Prof. Dr. Dr. h.c. Dr. h.c. Roland Benz in Würzburg durchgeführt wurden. Nachdem eine größenabhängige Toxizität für Goldnanoteilchen festgestellt wurde, ist ein besseres

Verständnis der Wechselwirkungen dieser Goldnanoteilchen mit biologischen Membranen essentiell. In den Experimenten habe ich unterschiedlich große und mit verschiedenen Liganden stabilisierte Teilchen untersucht. Nachdem der experimentelle Aufbau zusammen mit der Diplomandin Yvonne Klapper anhand antimikrobieller Peptide getestet war, habe ich bei Experimenten mit Goldnanoteilchen einen Anstieg der Membranleitfähigkeit in Abhängigkeit der Größe der Nanoteilchen festgestellt. Zusätzlich konnte ich zeigen, dass neben der Größe auch die Liganden, die zur Stabilisierung genutzt werden, einen Einfluss auf die Membranleitfähigkeit haben. Für die Interpretation der Ergebnisse wird in Kapitel 5 neben den experimentellen Ergebnissen ein von mir entwickeltes Modell zur Liganden-Verdrängung vorgestellt, das die experimentellen Beobachtungen erklärt und in ersten weiterführenden Experimenten meiner Kooperationspartner bestätigt werden konnte.

Der letzte Teil der Arbeit beschreibt Simulationen, die das Andocken von bestimmten Goldnanoteilchen an den hERG-Kanal untersuchen. Simulationen mit Goldnanoteilchen, die unterschiedlich viele Liganden tragen, wurden genutzt, um den Blockierungsmechanismus, der in Experimenten meiner Kooperationspartner beobachtet wurde, besser verstehen zu können. Dafür wurden zwei verschiedene Parametrisierungen des Kanals verwendet, bei denen ich das Andocken von Nanoteilchen mit einer unterschiedlichen Anzahl von Liganden untersucht habe. Die Simulationsergebnisse zeigen, dass das Andocken mit abnehmender Zahl von Liganden auf der Goldoberfläche wahrscheinlicher wird. Diese Ergebnisse ergänzen experimentelle Beobachtung, bei denen ein Überschuss von Liganden eine Blockade verhindern [3].

Insgesamt konnte gezeigt werden, dass das Bindungsverhalten der Goldnanoteilchen von den funktionellen Gruppen auf der Goldoberfläche abhängt. Sicherheitsbestimmungen für die Nutzung von Goldnanoteilchen in industriellen oder medizinischen Produkten sollten deshalb überdacht und angepasst werden [3].

# Contents

<b>Deutsche Zusammenfassung</b>	<b>iii</b>
<b>1. Overview and Outline</b>	<b>1</b>
<b>2. Introduction to Biomolecular Systems</b>	<b>7</b>
2.1. Proteins . . . . .	7
2.1.1. Amino Acids . . . . .	7
2.1.2. Protein Structure . . . . .	10
2.2. Protein Folding . . . . .	13
2.3. Biological Membranes . . . . .	15
2.3.1. Membrane Composition . . . . .	15
2.3.2. Membrane Proteins . . . . .	16
<b>3. Atomistic Simulation of Biomolecular Systems</b>	<b>17</b>
3.1. Methods . . . . .	17
3.1.1. Molecular Dynamics . . . . .	17
3.1.2. Monte Carlo Simulations . . . . .	18
3.2. SIMONA - A Monte Carlo Simulation Package . . . . .	20
3.2.1. Force Fields . . . . .	20
3.2.2. Using Non-Proteinogenic Amino Acids in SIMONA . . . . .	23
3.3. Validation of Dihedral Angle Distributions of Dipeptides in Monte Carlo Simulations . . . . .	24
3.4. Protein Stability in Monte Carlo Simulations . . . . .	28
3.4.1. Villin Headpiece . . . . .	29

3.4.2. WW Domain . . . . .	32
3.5. Small Molecule Hydration Free Energies . . . . .	34
3.5.1. Solvation Free Energy . . . . .	34
3.5.2. Nonpolar Solvent Interaction Models . . . . .	35
3.5.3. Data Set and Model Parametrisation . . . . .	35
3.5.4. Assessment of Nonpolar Solvent Interaction Models . . . . .	36
<b>4. An Improved Generalized Born Implicit Membrane Model - SLIM: Model, Simulations and Results</b>	<b>41</b>
4.1. Generalized Born Based Implicit Membrane Models . . . . .	42
4.2. SLIM - SIMONA Layered Implicit Membrane . . . . .	43
4.3. Comparison with the Poisson-Boltzmann Model . . . . .	46
4.4. Melittin . . . . .	49
4.5. M2 Protein . . . . .	55
4.6. Glycophorin A . . . . .	61
4.7. Summary . . . . .	64
<b>5. Black Lipid Bilayer Experiments</b>	<b>65</b>
5.1. Experimental Setup . . . . .	65
5.1.1. Conductivity Measurements . . . . .	68
5.1.2. Selectivity Measurements . . . . .	69
5.2. Antimicrobial Peptides . . . . .	69
5.2.1. Introduction . . . . .	69
5.2.2. Experimental Results and Discussion . . . . .	71
5.3. Gold Nanoparticles . . . . .	75
5.3.1. Introduction . . . . .	75
5.3.2. Experimental Results . . . . .	76
5.3.3. Discussion . . . . .	83
<b>6. Interaction Between the hERG Ion Channel and Gold Nanoparticles</b>	<b>87</b>

6.1. The hERG Channel and the Long QT Syndrome . . . . .	88
6.2. Experimental Results . . . . .	89
6.3. Docking Simulations . . . . .	90
6.3.1. Gold Nanoparticles . . . . .	90
6.3.2. Homology Model for the hERG Channel . . . . .	91
6.3.3. Docking Results . . . . .	92
6.3.4. Summary . . . . .	93
<b>7. Summary</b>	<b>95</b>
<b>A. PBEQ-Solver Settings</b>	<b>101</b>
<b>B. SIMONA Simulations</b>	<b>103</b>
<b>C. Additional Software Used in This Thesis</b>	<b>105</b>
<b>Bibliography</b>	<b>110</b>
<b>Acknowledgments</b>	<b>133</b>



# 1. Overview and Outline

Proteins are highly complex biomolecules involved in many biological processes in every living organism. They are composed of a sequence of different amino acids encoded in the DNA and mostly fold into a unique three dimensional structure. For many proteins, this structure depends only on the amino acid sequence and the physiological environment of the protein. Functional groups or binding interfaces in these structures allow interactions with other molecules or proteins, which can cause structural changes. Mediated by these changes, proteins can fulfil various functions: They catalyse biochemical reactions, exert physical forces by muscle contraction, are responsible for the structural integrity of cells, skin and hairs, act as transport proteins or guide other transport mechanisms. This years Nobel Prize in Physiology or Medicine was awarded to three scientists who investigated how cells organize their transport systems, a process in which proteins play a crucial role.

While experimental structure investigations like NMR spectroscopy or X-ray crystallography result in a large database of known protein structures, the protein database (PDB), the experimental methods still possess several limitations. Experimental conditions, such as the need for crystallization of a protein in X-ray experiments, can influence the protein structure. Other conditions, such as the native environment, can render experiments near impossible, which is especially true for membrane proteins. Although a known protein structure is a valuable starting point for investigating its function, experiments mostly provide static snapshots or ensembles of snapshots of these functions, while the processes underlying these functions are dynamic. Where experimental methods fail to provide a complete picture of the processes that govern protein function, computational methods provide the means to fill these gaps in our knowledge.

A widely used technique is Molecular Dynamics simulation, which solves Newton's equations of motion. Therefore, the protein energy landscape has to be described by a classical force field. These simula-

tions have become one of the fundamental building blocks of multi-scale modelling, a field which was recognized with the Nobel Prize in Chemistry this year. The time step used in Molecular Dynamics simulations is typically in the low femtosecond range, wherefore many iterations are necessary to reach biologically interesting timescales. One possibility to reduce the computational cost is the use of implicit solvent models. In these models, interactions between a system and its environment are captured by an additional potential of mean force, and not by computation of the interactions with every single atom of the environment. Another possibility to accelerate simulations is the use of Monte Carlo methods instead of Molecular Dynamics simulations. Monte Carlo methods estimate thermodynamic properties by a representative conformational ensemble of the molecule in question. Although these methods eliminate the time step problem of Molecular Dynamics simulations, Monte Carlo simulations have not been used extensively in the last decades to study the thermodynamic properties of biomolecular systems.

A substantial part of 20 to 30 % of all proteins is embedded in biological membranes. These membranes are composed of amphiphilic phospholipids and form a bilayer. Membranes are a hydrophobic barrier to prevent soluble particles to enter or leave the cell. Damage or malfunction of this natural barrier causes the death of the cell. One application that exploits intentional cell death is the treatment of bacterial diseases or cancer. Antimicrobial peptides can cause the destruction of bacterial membranes and are a promising alternative to antibiotics which are becoming increasingly ineffective due to the emergence of resistant bacteria.

Another important property of membranes is the selectively permeable structure, which is mediated by special membrane proteins. An example for such a protein is the hERG potassium ion channel, whose function is crucial for normal activity of the human heart and is used in pre-clinical testing for essentially all drug candidates. Recent experimental investigations for two different gold nanoparticles showed that the channel function is influenced by one of them under certain conditions. Since gold nanoparticles in general have promising biomedical applications as drug carriers, therapeutics or contrast agents, side effects like the influence on the hERG channel are undesired and must be investigated before gold nanoparticles can safely be used in these applications. In general, the knowledge about the interaction of nanoparticles or other chemical compounds with membrane bound proteins, or even

---

---

membranes themselves, is still limited. A first step characterizing interactions of therapeutics, drug candidates or proteins with membranes is the use of artificial membranes, so called black lipid bilayers, in experiments. These allow tests of the membrane's hydrophobic barrier by conductivity and selectivity measurements.

For investigations on a molecular level, computational studies represent an increasingly attractive approach to complement experiments. Unfortunately, the complex biological environment of membrane proteins poses a significant challenge for explicit membrane studies. The high computational effort of all atom membrane representations severely limits the processes that can be studied with presently available techniques. To overcome this obstacle, implicit membrane models can be used.

The first objective of the work presented here is to establish new computational methods to reduce the limitations caused by the high computational cost of explicit Molecular Dynamics simulations. Therefore, I participated in implementing a new Monte Carlo based simulation protocol for proteins, which I validate in this thesis. Together with Martin Brieg and Carolin Seith I developed and parametrized a new implicit membrane model, for which I show different tests and validations. The second objective is a combined experimental and theoretical investigation of the interactions of drug candidates with membranes and membrane embedded proteins. Therefore, I have performed black lipid bilayer experiments. The results of these experiments presented here characterize the influence of antimicrobial peptides and gold nanoparticles on the membrane's hydrophobic barrier. Based on these results, I have developed a simple model that can explain my experimental observations. Additionally, I have studied the blocking of the hERG ion channel by coated gold nanoparticles in simulations. From these simulations I deduce a general requirement for a stable complex formation between gold nanoparticles and the hERG ion channel.

This thesis is structured as follows: I provide a short introduction to proteins and biomolecular membranes in Chapter 2, which summarizes the basics to understand the investigations and results reported in the following chapters.

The third chapter introduces Monte Carlo methods and the force fields used in the software package SIMONA. I summarize the new degrees of freedom which I have added to the simulation protocol, together with the diploma student Carolin Seith, and describe how I validate them by simulations of small peptides. The free energy landscapes of these peptides show the expected minima, which are essential to describe the secondary structure of proteins. I have performed Monte Carlo simulations based on the new protocol to test the stability of the tertiary structure of several small proteins. My simulations allow me to compare the computational effort required for such studies to that of other methods. After that, I present an investigation on how to further enhance the accuracy of implicit solvent models, where I analysed the performance of three implicit solvent models that use different methods to treat nonpolar solvation effects. My analysis shows that one of these models can match the accuracy of the explicit water TIP3P model with a minimal set of optimized parameters. It also points out a general problem of many commonly used implicit solvent models. Therefore, my analysis provides valuable insights on how to improve implicit solvent models in the future.

Chapter 4 introduces a new implicit membrane model to study orientation, folding or assembly of membrane proteins. This SLIM (SIMONA layered implicit membrane) model combines advantages of other previous published models regarding the accurate modelling of electrostatic effects inside membranes. I demonstrate this by performing comparisons to PB reference calculations, which also fix the free parameters of this model. Afterwards, I present results of Monte Carlo simulations for three well studied membrane proteins, Melittin of bee venom, the transmembrane domain of the M2 protein and the transmembrane domain of Glycophorin A. They are compared to other computational and experimental studies to demonstrate that the SLIM model is able to reproduce known properties of these proteins.

Gold nanoparticles are possible drug candidates, wherefore their interactions with membranes have to be understood. In Chapter 5 I explain the experimental investigations with the black lipid bilayer method, which I used to characterize such interactions. The experimental setup for the bilayer experiments, which I used together with the diploma student Yvonne Klapper, is validated by measurements

---

---

for antimicrobial peptides, also presented in this chapter. My bilayer experiments characterize the effects of differently sized and coated gold nanoparticles on the membrane's hydrophobic barrier. I present a simple model that explains my experimental observations and provide a foundation to better understand the interaction of the membranes with gold nanoparticles.

Gold nanoparticles may not only interact with a biological membrane, but also with the proteins embedded in that membrane. I investigated a mechanism that is known to cause cytotoxicity, the blocking of the hERG channel by specifically coated gold nanoparticles with atomistic simulations. Chapter 6 describes the channel parametrisation at different environmental conditions and how I generated gold nanoparticles coated with different numbers of ligands. Afterwards, I estimate the probability for complex formation between the gold nanoparticles and the hERG channel using docking simulations. The conclusion I present highlights the important role of the ligands coating the nanoparticle to form a stable complex and complement the experimental findings of my co-workers.

This thesis closes with a summary of the results I have achieved and a discussion of their relevance for future investigations and applications.



## 2. Introduction to Biomolecular Systems

This chapter provides an introduction into the relevant background on proteins and biological membranes, which are crucial for understanding the investigations reported in this thesis. The composition and function of proteins is summarized in Section 2.1, while folding into their distinct structure is described in Section 2.2. Biological membranes, their function and composition, as well as the function of membrane proteins are explained in Section 2.3.

### 2.1. Proteins

Proteins are the nano-scale machinery of living cells and involved in many biological activities. Proteins catalyse chemical reactions, transport ions or metabolites across membranes, act as signal receptors or are involved in energy conversion [4–6]. While some proteins exist in solvent, others are partially or fully embedded in membranes. The three-dimensional structure, which many proteins spontaneously assume is important for their function. Functional groups or binding interfaces in these structures allow interactions with other proteins or molecules. Protein function often entails structural changes that are difficult to characterize by static structures, such as those obtained from x-ray crystallography. To understand processes in which proteins are involved, the knowledge of their structure and dynamics is crucial.

#### 2.1.1. Amino Acids

Amino acids are the fundamental building blocks of peptides and proteins. They have two common functional groups, the amine- and the carboxyl-group, but differ in the side chains. Amine-group, carboxyl-group as well as the specific side chain are bound to the  $C_\alpha$ -atom of the amino acid. A

sequence of different amino acids, also called residues, specifies a peptide or protein. The single amino acids are linked via the peptide bond displayed in 2.1.

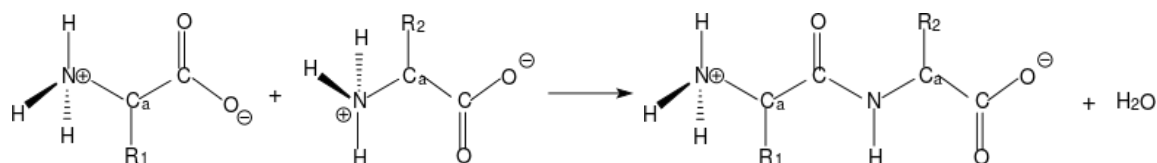


Figure 2.1.: Peptide bond formation. The carboxyl group of the first amino acid reacts with the amino group of the second one to form a peptide bond.

The periodic occurring units, NH-C<sub>α</sub>-CO, are the backbone that build the main chain of the peptide. The carboxyl group of the previous amino acids reacts with the amino group of the following one, thus only the amino group of the first amino acid (N-terminus) and the carboxyl group of the last one (C-terminus) remain.

Proteinogenic amino acids, displayed in Figure 2.2, are encoded by the universal genetic code and can be grouped into charged, polar, hydrophobic amino acids and special cases. For every amino acid there are abbreviations for their names, a three letter and a one letter code. In context of this thesis the three letter code will be used. The human body is able to synthesize only some amino acids, all others have to be consumed and are therefore called essential amino acids.

- **Non-essential amino acids:**

alanine=ALA, arginine=ARG, aspartic acid=ASP, asparagine=ASN, cysteine=CYS, glutamine=GLU, glycine=GLY, proline=PRO, serine=SER, tyrosine=TYR.

- **Essential amino acids:**

histidine=HIS, isoleucine=ILE, leucine=LEU, lysine=LYS, methionine=MET, phenylalanine=PHE, threonine=THR, tryptophane=TRP, valine=VAL.

Non-natural amino acids like norleucine and peptide caps used for simulations in this thesis are described later in the corresponding chapters.

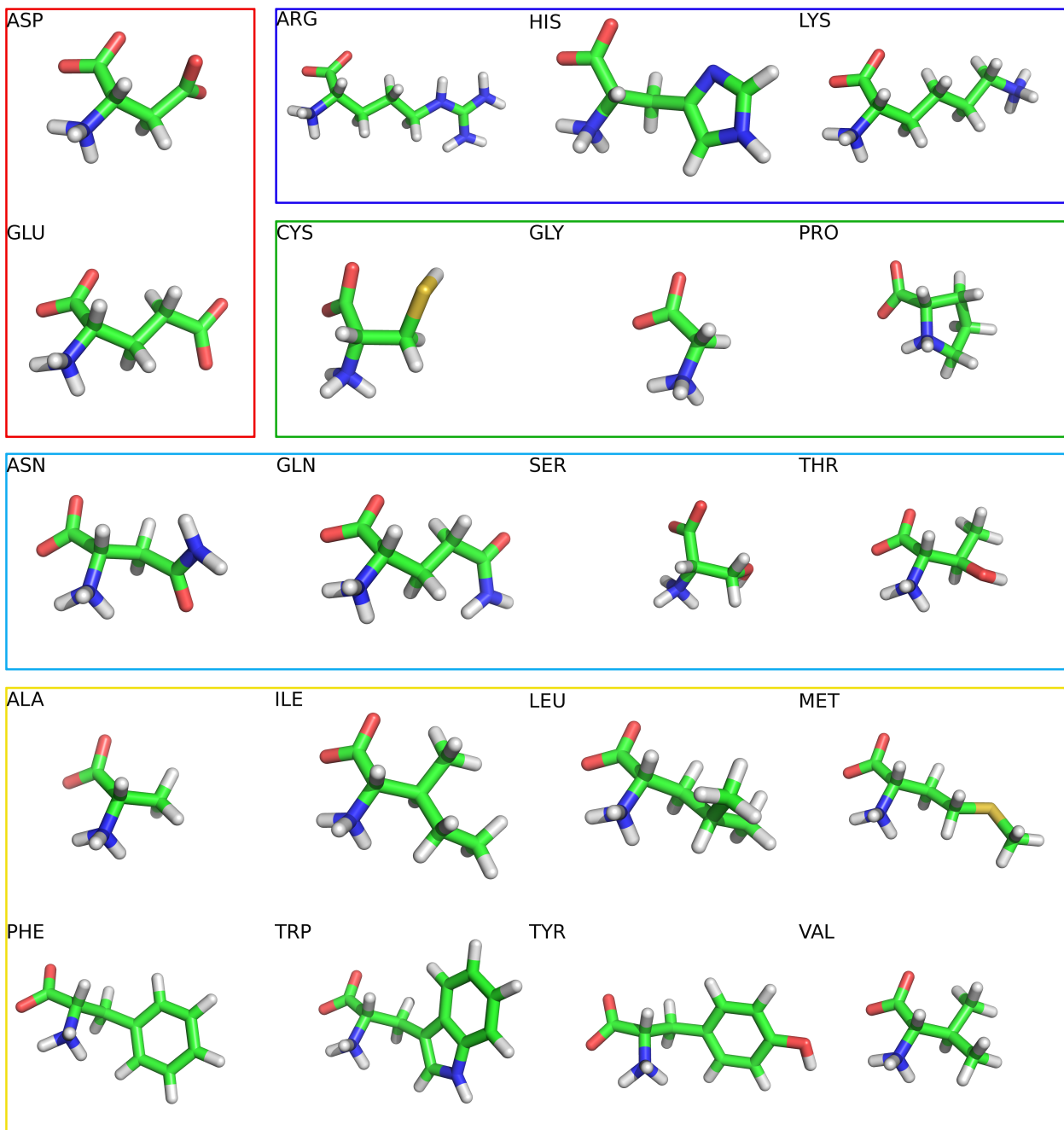


Figure 2.2.: 20 proteinogenic amino acids: positive or negative charged amino acids, special cases and polar or hydrophobic amino acids.

### 2.1.2. Protein Structure

The physiological environment together with the amino acid sequence determines the three-dimensional structure of many proteins [7]. For the protein structure, four different classes can be distinguished. These are the sequence, formation of secondary structure elements like helices or  $\beta$ -sheets, a global three-dimensional structure and the agglomeration of different single chains. They are summarized in the following sections.

Experimentally determined structures can be found in the protein database ([www.pdb.org](http://www.pdb.org) [8]). The provided files with atoms, residues and coordinates can be used as input files for simulations.

#### Primary Structure

The primary structure describes the sequence of the amino acids (residues) along the main chain (see also Section 2.1.1). The first known sequence was determined 1949 by Sanger et al. for the essential hormone insulin [9].

Covalent bonds in the main chain and the dihedral angles they form are the same for each residue. An dihedral angle is defined by four atoms and describe the angle between two planes. The first three atoms span the first plane the second, third and fourth atom the second plane. To a large extend main chain dihedrals can be used to characterize the three-dimensional structure of a protein. The three main chain dihedrals are defined by the following atoms with atoms indicating atoms of a neighbouring amino acid.

- **Dihedral angle  $\Phi$ : C' - N - Ca - C**

The covalent bond between N and Ca is one of the main degree of freedom of the main chain.

- **Dihedral angle  $\Psi$ : N - Ca - C - N'**

This dihedral is also flexible and a second main degree of freedom.

- **Dihedral angle  $\Omega$ : Ca - C - N' - Ca'**

This bond is a partial double bond due to mesomerism of the free electron pair of the nitrogen atom. Therefore the dihedral is not very flexible. In some models  $\Omega$  is therefore treated as rigid, but simulations of this thesis were performed with flexible  $\Omega$ .

Although  $\phi$  and  $\psi$  are very flexible, some combinations for dihedral angles are not possible due to steric restraints. Ramachandran et al. visualised the backbone dihedrals in the so called Ramachandran Plot [10], where allowed dihedral angle combinations are displayed. The most populated regions refer to the secondary structures  $\alpha$ -helix and  $\beta$ -sheet.

## Secondary Structure

In proteins, regular structures can be found, which are called secondary structure elements. The dihedral angles of the residues in these structures have similar values. Two major types of secondary structure,  $\alpha$ -helix and  $\beta$ -sheet, can be distinguished [5]. They are stabilized by hydrogen bonds between the polar atom groups NH and CO of the backbone. Pauling and Corey first proposed these structures in 1951 and used them to characterize protein structures [11–17]. To get a better understanding of a three-dimensional protein structure, they are usually depicted in a reduced representation of the molecule, where only the backbone is represented by a tube. Secondary structure elements, such as  $\alpha$ -helices or  $\beta$ -sheets are usually highlighted in this representation as depicted in Figure 2.3. The picture shows the cartoon representation for an  $\alpha$ -helix and a  $\beta$ -sheet where hydrogen bonds are displayed with dashed red lines.

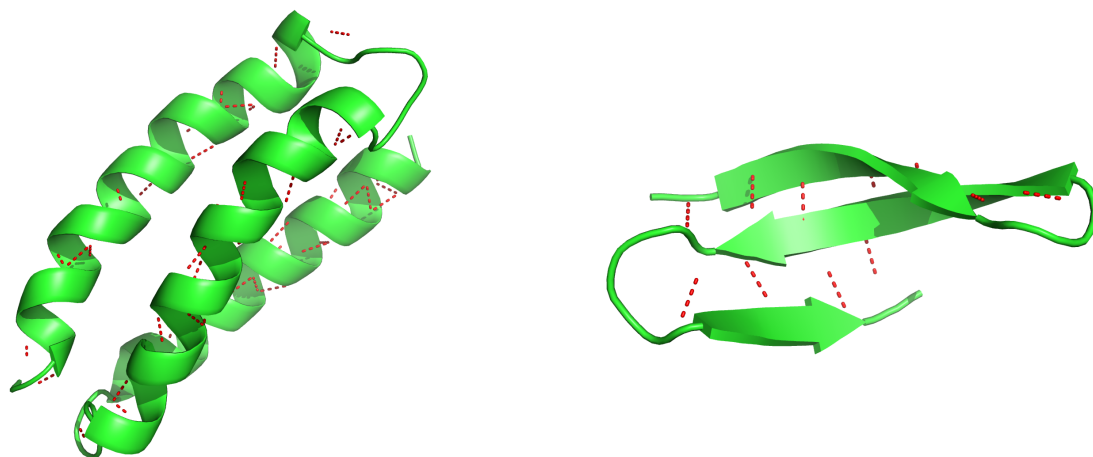


Figure 2.3.: Secondary structure elements: (a)  $\alpha$ -helix (PDB-code: 2A3D [18]) and (b)  $\beta$ -sheet (PDB-code: 2F21 [19]) in the cartoon representation. Hydrogen bonds are shown with dashed, red lines.

### Tertiary Structure

The global three-dimensional structure is the tertiary structure of a protein. Proteins with similar amino acid sequences often show similar tertiary structures. Therefore known structures can be used for homology models of unknown structures, if the sequences match well [20]. The three-dimensional structure can form binding pockets or active sites which are important for the interactions with other molecules and therefore crucial for the protein function. An example for a tertiary structure is shown in Figure 2.4. Secondary structure elements of Myoglobin [21] are coloured differently and merge into global three-dimensional structure with a binding pocket.

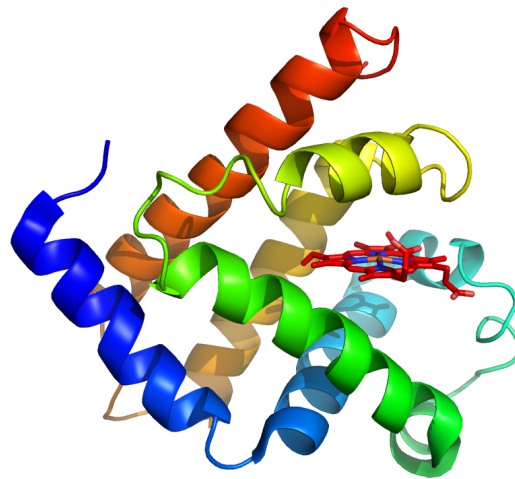


Figure 2.4.: Secondary structure elements (colored differently) of Myoglobin (PDB-code: 1MBN [21]) fold into a global three-dimensional structure, the tertiary structure of the protein.

### Quaternary Structure

The quaternary structure describes how different amino acid chains of a single protein are orientated with respect to each other. Different chains in one protein are not covalently bound.

Figure 2.5 shows one protein, haemoglobin [22], consisting of four different chains colored in blue, red, purple and orange.

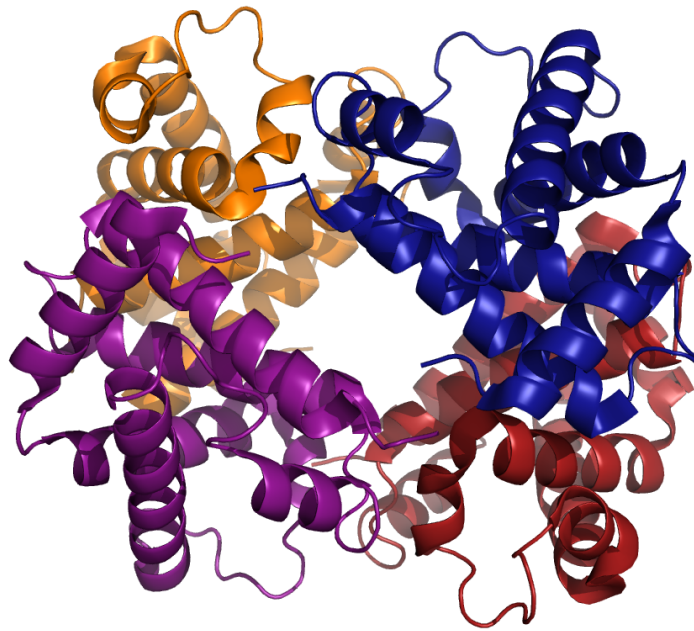


Figure 2.5.: Different chains (colored differently) of Haemoglobin (PDB-code: 1HDA [22]) form the quaternary structure of the protein.

## 2.2. Protein Folding

In contrast to many other polymers, many proteins spontaneously assume a three-dimensional structure. For this reason, a large number of models and investigations have been devoted to elucidate this mechanism. Levinthal noted that the large number of degrees of freedom excludes folding by diffusive search of the energy landscape. There exists an astronomical number of possible conformations for the protein chain, which leads to the finding that proteins do not sample their conformational space randomly [23].

Today our understanding of protein folding is based on Anfinsen's thermodynamic hypothesis, which was awarded with the Nobel Prize in 1972. It postulates that the folding of a protein in its physiological environment occurs by minimizing the Gibbs free energy and depends only on the amino acid sequence. Anfinsen et al. showed in their experiments that proteins refold into their native structure after denaturation [7].

As solution to Levinthal's paradox is the funnel theory based on Anfinsen's hypothesis: The free energy landscape, displayed in Figure 2.6, of a protein consists of funnels with an energy gradient pointing towards the native structure [24, 25]. How fast a protein folds depends on the channel.

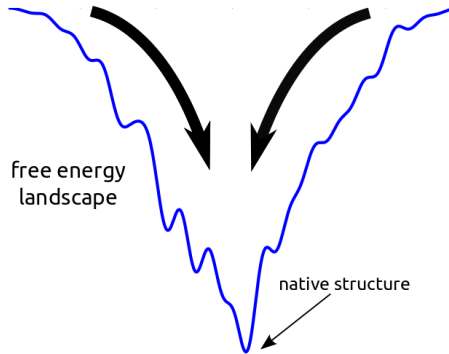


Figure 2.6.: The minimum of the free energy landscape of a protein is the native structure. The folding funnel shows an energy gradient pointing towards the native structure.

For the folding mechanism three different models are established [26]:

- **Framework model** [27]:

1. The secondary structure elements are formed.
2. Secondary structure elements diffuse and form the tertiary structure.

- **Hydrophobic collapse** [28]:

1. A hydrophobic core is formed.
2. Local secondary structure elements further stabilize the hydrophobic core.

- **Nucleation model** [29]:

1. A local segment folds into its secondary structure.
2. Subsequently the folding in a tertiary structure is permitted.

Framework model and hydrophobic collapse require intermediate states which were found to be necessary [30]. Therefore the nucleation model was enhanced to a nucleation-condensation model which combines all models described above [26].

## 2.3. Biological Membranes

Biological membranes are selective barriers around a cell. They are composed of a bilayer of amphiphilic lipids which shield the cell from the exterior [31]. A hydrophobic core prohibits the diffusion of solved particles through the membrane. Transport through this barrier is mainly established by membrane proteins.

### 2.3.1. Membrane Composition

Biological membranes are composed of lipids, proteins and carbohydrates [32]. The lipids show an amphiphatic structure with a polar headgroup and a hydrophobic core. The lipids form a bilayer (Figure 2.7) with the hydrophobic tails in the membrane center and the polar groups facing the aqueous solution both in the cell interior and outside the cell.

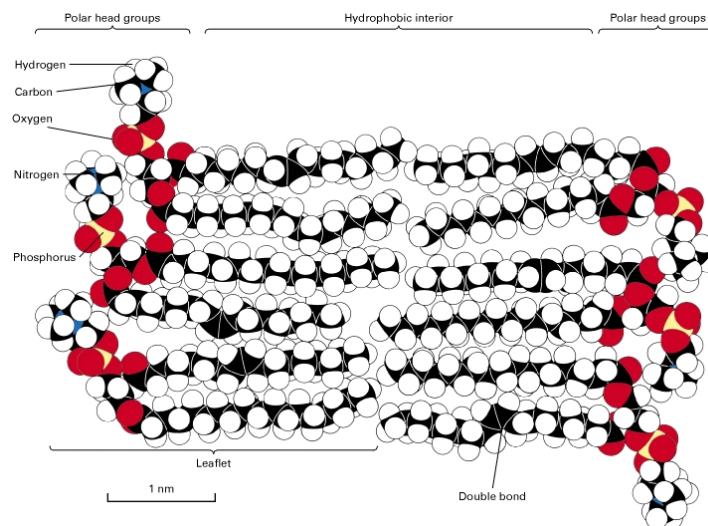


Figure 2.7.: A bilayer is composed of two layers of lipids. The polar heads facing the aqueous phases and the hydrophobic lipid tails are in the interior of the bilayer. (Image source: [31])

The lipid tails, which are fatty acid chains, show a varying number of carbon atoms and therefore have a different length. Unsaturated fatty acids have double bonds which cause bends in the tails and therefore are responsible for a bigger distance between the lipids [33]. Most membrane lipids are phospholipids which contain diglyceride, a phosphate group and e.g. choline or glycerol as the head-group. Diglycerides are two fatty acids bound to a glycerol.

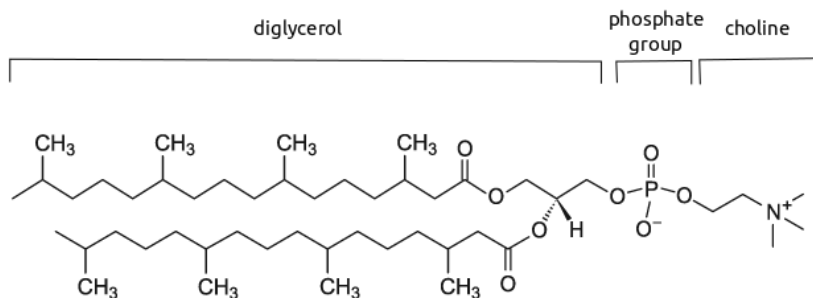


Figure 2.8.: Chemical structure of diphytanoyl-phosphatidylcholine (DiphPC). Labeled are the three different building blocks of the lipid: a diglyceride, a phosphate group and choline.

An examples for a phospholipid is shown in Figure 2.8.

In contrast to phospholipids in glycolipids the phosphate group is replaced by a sugar molecule. These lipids have important roles in cell signalling and the immune system [34].

Varying composition, head groups and lengths of lipid tails result in many different biological membranes. All these membranes have a hydrophobic core and a polar headgroup with varying sizes.

### 2.3.2. Membrane Proteins

Membrane proteins can be divided into two main classes: Peripheral proteins, which do not interact with the membrane core and integral proteins, which penetrate or span the bilayer [35]. Depending if they are membrane spanning or bound to the surface, their composition of hydrophobic and hydrophilic residues varies. Membrane proteins very often show an amphiphilic character. While the part inside the membrane mainly consists of hydrophobic residues, regions ranging into the headgroup region or the solvent have hydrophilic residues. The transmembrane region of a membrane protein shows mainly helical structures, since hydrophilic parts of the main chain are shielded in a helix [6].

Membrane proteins fulfil different functions: They are involved in biological energy conversion, enable the specific transport of metabolites and ions across the membrane, act as signal receptors and catalyze biochemical reactions [4]. Antimicrobial peptides can destroy bacterial membranes and are an alternative to antibiotics [36, 37]. Their structure and the mode of action are discussed in Chapter 5.2, where their effects on artificial bilayer experiments are presented.

## 3. Atomistic Simulation of Biomolecular Systems

The increasing availability of computational resources allows simulations to supplement experimental investigations. In life- and material science, simulations can be used to understand or predict properties of molecular or nano-scale systems, like structural changes of proteins, drug binding or self-assembly [38–41].

This chapter summarizes computational methods like Molecular Dynamics and Monte Carlo methods in general (Section 3.1) and introduces the Metropolis Monte Carlo based software package SIMONA as well as the force fields relevant for protein simulations (Section 3.2). The parametrization of non standard residues, such as non-proteinogenic amino acids, is explained. Furthermore the results of testing newly implemented force fields and additional degrees of freedom (Section 3.3 and 3.4) are shown. In the last paragraph an outline to model the solvation free energy of very small, drug-like molecules (Section 3.5), published in Brieg et al. [1], better, is given.

### 3.1. Methods

#### 3.1.1. Molecular Dynamics

A very common tool are Molecular Dynamics (MD) simulations, which solve Newton's equations of motion (equation 3.1) numerically for every atom  $i$  with mass  $m_i$  and position  $\vec{r}_i$  [42–44].

$$\vec{F}_i(t) = m_i \cdot \frac{\partial^2 \vec{r}}{\partial t^2} \quad (3.1)$$

To simulate a system of particles, for instance a molecule, it has to be described by a classical force field. This approximation requires that the processes of interest are not governed by quantum mechanical

effects. Calculating the forces and using numerical integration techniques results in a time-resolved trajectory of the system. The Verlet-Störmer integration algorithm is widely used [45]. For every time step  $\Delta t$  the positions and velocities are calculated. To avoid instabilities, the time step has to be chosen carefully with respect to the shortest timescales processes occurring in the system of interest. These are typically atomic oscillations and require a time step in the low femto second range, so  $\Delta t = 1fs$  is very common in MD simulations.

Most biological processes happen on a time scale of microsecond ( $ms$ ) to second range ( $s$ ) [46], so about  $10^{12}$  iterations are necessary to reach biologically interesting timescales. With increasing system size or longer timescales, the computational cost increases rapidly and despite recent progress in hard- and software, only expensive specialised computers are able to reach the low millisecond range [47–51].

One possibility to reduce the computational effort is the use of implicit solvent models. Interactions between system and environment are captured by an additional potential of mean force, where the surrounding water or biological membrane may be represented by different dielectric regions instead of every single atom. While losing some accuracy, it is possible to reduce the large number of atoms and to avoid the need of periodic boundary conditions. Figure 3.1A illustrates the immense number of explicit water molecules in a simulation box or in an explicit representation of a Dipalmitoylphosphatidylcholine (DPPC) membrane embedded in water.

Using an implicit environment, only the forces between atoms within the molecule in question have to be computed, thus drastically decreasing the computational cost.

#### 3.1.2. Monte Carlo Simulations

An alternative to MD simulations are Monte Carlo (MC) simulations, which are used to estimate thermodynamic properties by a representative ensemble of conformations. A chain of conformations is generated by randomly disturbing the prior conformation and rejecting or accepting the new conformation according to an acceptance criterion. This approach eliminates the time step problem at the expense of losing information about the timescales at which the processes occur.

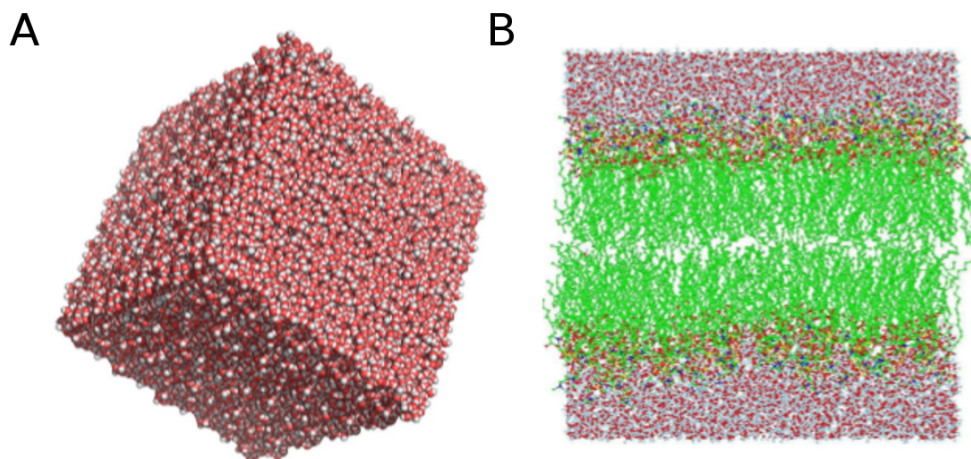


Figure 3.1.: Simulations with explicit water molecules or with an explicit membrane representation require a simulation box with periodic boundary conditions. Panel A shows a cubic box filled with TIP3P water molecules. Panel B (image source: [52]) shows a DPPC-membrane with more than 30.000 atoms.

### Metropolis Monte Carlo

MC methods rely on a chain of random conformations. The sampling with Metropolis MC allows to evaluate thermodynamic expectation values according to an equilibrium distribution [53].

Starting from a conformation  $R^{(i)}$ , a new conformation  $R^{(p)}$  is generated by a random perturbation. If the transition probability  $\Pi_{i \rightarrow j}$  between conformation  $i$  and  $j$  is larger than a random number  $r \in [0, 1]$ , the new conformation  $R^{(p)}$  will be accepted (see also Figure 3.2).

The conformations of the ensemble are Boltzmann distributed because of the used acceptance criterion for Metropolis MC:

$$\Pi_{i \rightarrow j} = \begin{cases} e^{-\frac{\Delta E_{ij}}{k_B T}} & \Delta E_{ij} > 0 \\ 1 & \Delta E_{ij} < 0 \end{cases} \quad (3.2)$$

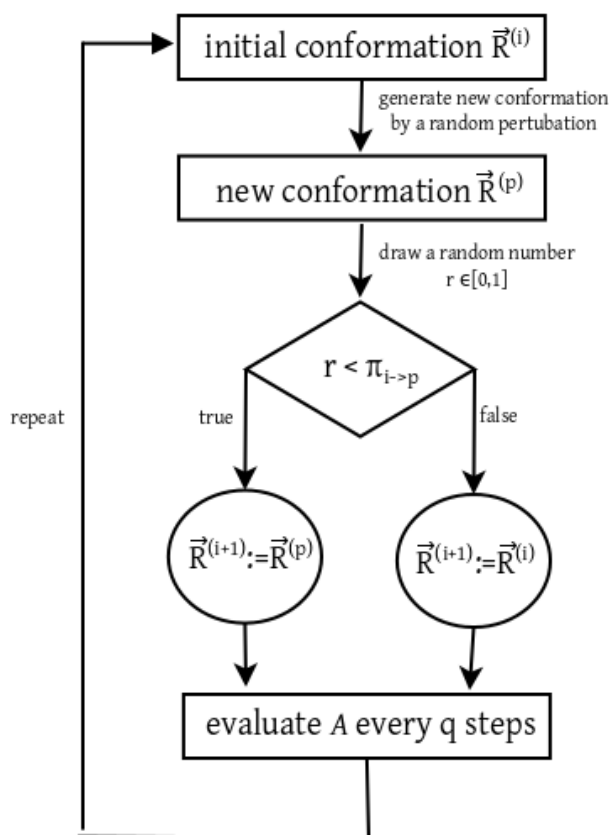


Figure 3.2.: Metropolis Monte Carlo algorithm: new conformations are generated by random perturbations and accepted depending on the transition probability  $\Pi_{i \rightarrow p}$ .

## 3.2. SIMONA - A Monte Carlo Simulation Package

SIMONA - **S**imulation of **M**olecular and **N**anoscale systems - is a Metropolis MC simulation package which combines force fields and algorithms to simulate protein conformational changes, protein-protein association, small-molecule protein docking and the growth of nanoscale clusters of organic molecules [54]. The program was developed in our group in the last decade and includes former programs like POEM (Protein Optimization with free Energy Methods) [55, 56], FlexScreen [57] or Deposit.

### 3.2.1. Force Fields

In all computational studies of molecular systems, potential functions that approximate the motion of atoms, so called molecular force fields, are very common. This section introduces the force fields

currently implemented in SIMONA which are relevant for protein simulations. The force field terms can be divided in bonded and non-bonded interactions respectively:

- **Non-bonded interactions:**

- Lennard-Jones Potential: Van der Waals interaction and Pauli repulsion
- Electrostatic interactions (Coulomb Potential)
- Solvation free energy: Polar part and nonpolar part

- **Bonded interactions:**

- Dihedral Potential

Non-bonded interactions are typically long range interactions and the atoms are not necessarily bound. Unless stated otherwise, no cut-offs for the computation of these potentials are used. Very often MD simulations have two additional potentials for bonded interactions: bond angles and distances. These potentials take into account that angles can bend and bonds can be stretched. Investigating proteins and large conformational changes, it is assumed that these degrees of freedom can be neglected. Due to the higher sampling efficiency they are not modelled in SIMONA.

All SIMONA force fields terms are described by equations 3.3 - 3.7.

$$\sum_{i \neq j}^{N_{atoms}} 4\epsilon_{ij} \left\{ \left( \frac{\sigma_{ij}}{r_{ij}} \right)^{12} - \left( \frac{\sigma_{ij}}{r_{ij}} \right)^6 \right\} \quad \text{Lennard-Jones Potential} \quad (3.3)$$

$$\sum_{i \neq j}^{N_{atoms}} \frac{q_i q_j}{4\pi\epsilon_p\epsilon_0 r_{ij}} \quad \text{Coulomb Potential} \quad (3.4)$$

$$-\frac{\alpha}{2} \left( \frac{1}{\epsilon_p} - \frac{1}{\epsilon_w} \right) \sum_{i,j}^{N_{atoms}} \frac{q_i q_j}{\sqrt{r_{ij}^2 + R_i R_j} \exp\left(-\frac{r_{ij}^2}{4R_i R_j}\right)} \quad \text{Solvation Free Energy - Polar Part} \quad (3.5)$$

$$\gamma \sum_i^{N_{atoms}} A_i \quad \text{Solvation Free Energy - Nonpolar Part} \quad (3.6)$$

$$\sum_i^{N_{angles}} \sum_{n=1}^3 V_{n_i} (1 + \cos(n_i \Theta - \gamma_{n_i})) \quad \text{Dihedral Potential} \quad (3.7)$$

### Lennard-Jones Potential

The Lennard-Jones 6-12 potential (equation 3.3) proposed by John Lennard-Jones in 1924 models the interaction between two uncharged atoms and is comprised of two terms. The  $r_{12}$  summand models the Pauli repulsion due to overlapping electron orbitals, the  $r_6$  summand is the attractive van der Waals term that models dispersion interactions between these atoms. The Lennard-Jones parameters  $\sigma$  and  $\epsilon$  are taken from the widely used AMBER99SB\*-ildn force field [58–60].

### Coulomb Potential

The electrostatic interactions between atoms carrying partial charges are modeled via the common Coulomb potential, first published 1785 by Charles Augustin de Coulomb. The potential depends on the partial atomic charges  $q_i$  and  $q_j$  and the distance between the two atoms  $r_{ij}$ . Further parameters are the permittivity  $\epsilon_0$  and the relative permittivity  $\epsilon_r$  of the material. The charges  $q_i$  are also taken from the AMBER99SB\*-ildn force field [58–60].

### Solvation Free Energy

#### *Polar Part*

Implicit solvent models treat the solvent as a continuous dielectricum that can be described with Poisson-Boltzmann (PB) theory [61]. PB theory is further approximated by the less computational demanding generalized Born (GB) model. Equation 3.5 is the GB formula proposed by Still et al. [62]. Beside the permittivities of the protein  $\epsilon_p = 1$  and the surrounding water  $\epsilon_w = 80$ ,  $\alpha = 331.84 \text{ kcal/mol}$  is a third constant. Other parameters are the partial charges  $q_i$  and  $q_j$ , the distance between the atoms  $r_{ij}$  and the Born radii  $R_i$  and  $R_j$ . The Born radii are computed with PowerBorn, a fast and accurate method by Brieg et al. [63] and are a measure for the polarization of the solvent induced by the charges of the solute.

#### *Nonpolar Part*

The nonpolar part penalizes cavity formation in water and is usually described by a solvent accessible surface area (SASA) based term [64]. Different nonpolar models are discussed as well in the literature

[64–72] as in Section 3.5. In SIMONA the constant  $\gamma = 5.42\text{cal}/(\text{mol}\text{\AA}^2)$  is used [73].

## Dihedral Potential

The dihedral potential models energy changes by torsion of dihedral angles in SIMONA and is adapted from the AMBER dihedral potential. The proper dihedral angles are defined by four atoms joined through covalent bonds (see also Section 3.3). Improper dihedral angles penalize the distortion of rings and other planar groups. The list of the dihedral angle terms is generated automatically using GROMACS [74].

### 3.2.2. Using Non-Proteinogenic Amino Acids in SIMONA

New residues like non-proteinogenic amino acids (e.g. norleucine), peptide caps (e.g. ACE or NME) or other molecules not implemented in SIMONA can be added with a few steps. Since force field parameters are taken from GROMACS [74], all needed residues must be known to GROMACS as well. If the residue already exists in GROMACS, step 1 can be skipped.

- **Step 1:** Adding a new residue in GROMACS

Each force field has an own folder, p.e. for the AMBER99SB\*-ildn [58–60] the folder *amber99sb-star-ildn.ff/* which is by default in */usr/share/gromacs/top/*. In addition to this force field folder a file *residuetypes.dat* with a list of all residues exists. The complete force field folder and the file *residuetypes.dat* should be copied to the working directory to avoid major changes in the program. Using the GROMACS program *pdb2gmx* [74] in the same working directory will automatically use the modified force field files for the parametrization.

First of all, a new label for the residue is necessary. The labeling should be done very carefully! A label with three characters should work without trouble, otherwise correct spacing in all files is required. E.g. the label “NLE” for norleucine could cause problems because of the N-terminus leucine with the name “NLEU”. With the wrong spacing, the molecule will be parametrized wrongly, so the label “ZLE” was used in this case. This label and appropriate specification like “protein” needs to be added to the list in *residuetypes.dat*. Then a list with the atom names, atom types, charges and a counter, as well as a list with bonds, dihedrals and impropers has

to be added to the file *aminoacids.rtp*. Charges can be generated with other programs like e.g. Yasara [75] or DFT calculations using Turbomole [76]. If the option *-ignh* is used in the parametrization step with GROMACS, a list of the residues hydrogen atoms needs to be added in the file *aminoacids.hdb*. Useful hints and explanations can be found on the GROMACS manual and webpage ([www.gromacs.org](http://www.gromacs.org)).

- **Step 2:** Adding a new residue in SIMONA

Each residue has an own amino acid xml in the folder *simona/python/configs/poem\_residues*. Beside the atomlist (alternate names can be skipped), the main- and side-chain dihedrals must be listed with up to four anchor atoms. “Right” and “left” specifies the connections to neighbouring residues. Bond distances and coordinates are not necessary, but the first and second atom of the bond must be declared in the bond list. At the end of the file, C and N terminus atoms can be specified.

For SIMONA, the formatting of the file is instrumental in order to correctly parse the file. It is recommended to copy the amino acid xml of a similar residue and to adapt that file.

### 3.3. Validation of Dihedral Angle Distributions of Dipeptides in Monte Carlo Simulations

The thermodynamicly most accessible degrees of freedom in proteins are the dihedral angles. In simulations with the former program POEM [56], only the backbone dihedrals  $\phi$  and  $\psi$  were moved (see Figure 3.3B). In SIMONA [54] it is also possible to move  $\Omega$ ,  $\chi$  and  $\nu$  dihedrals.  $\Omega$  is the dihedral angle between two amino acids and belongs to the backbone dihedral group.  $\chi$  and  $\nu$  are side chain dihedrals.

- Backbone dihedrals:  $\phi$ ,  $\psi$ ,  $\Omega$
- side chain dihedrals:  $\chi$  and  $\nu$

$\psi$  is defined by the atoms N, CA, C and the N' atom of the prior amino acid. For the  $\phi$  angle definition the C' atom of the following amino acid and N, CA and C are necessary.  $\Omega$  is the dihedral of the peptide bond and defined by CA and C as well as N' and CA' of the prior amino acid.  $\chi$  and  $\nu$  dihedrals depend

on the amino acid side chain. An example for angle definition of the amino acid leucine is summarized in table 3.1 and Figure 3.3.

Table 3.1.: Definitions of the dihedral angles for the leucine residue. Each dihedral is defined by four atoms. Primed atoms belong to the neighbouring residues, the first three dihedral angles have the same definition in each amino acid.

$\phi$	C'	N	CA	C
$\psi$	N	CA	C	N'
$\Omega$	CA	C	N'	CA'
$\chi_1$	N	CA	CB	CG
$\chi_2$	CA	CB	CG	CD1
$\nu_1$	CB	CG	CD1	HD11
$\nu_2$	CB	CG	CD2	HD21

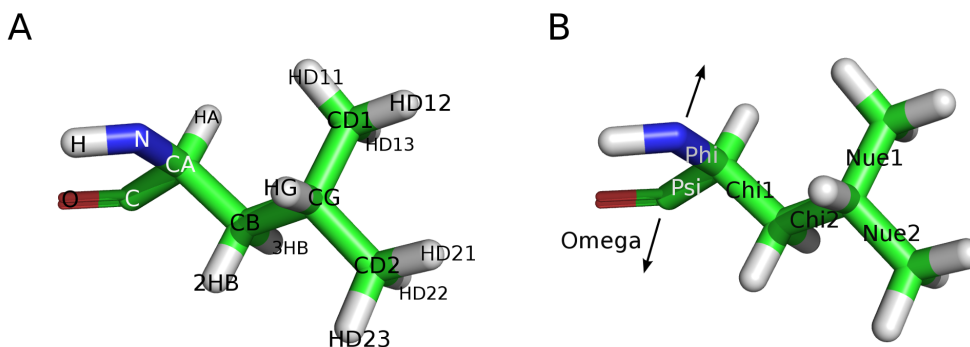


Figure 3.3.: Four atoms of an amino acid define a dihedral angle. Panel A shows the leucine residue with its atoms and the corresponding dihedral angles (Panel B).  $\phi$ ,  $\psi$  and  $\Omega$  are the backbone dihedrals (same definition in all residues), while  $\chi$  and  $\nu$  describe side chain dihedrals and are amino acid specific. The connections to neighbouring amino acids are indicated by arrows in panel B.

The  $\nu$  dihedrals (number in brackets) were missing in SIMONA and have been added to the following amino acids:

alanine (1), arginine (1), asparagine (1), cysteine (1), glutamine (1), isoleucine (2), leucine (2), lysine (1), methionine (1), serine (1), threonine (2), tyrosine (1), valine (2).

### Dipeptide Simulations

To test the force field in the reduced conformation space by choosing rigid bond lengths and bond angles, I have examined dipeptides by performing MC simulation to sample their free energy landscapes. The 20 dipeptides are composed out of the 20 amino acids respectively with neutral peptide caps ACE (acetyl) and NME (N-methyl) on either end. The system has two peptide bonds, hence the name dipeptide. ACE and NME are displayed in Figure 3.4 and in the context of this thesis added to the available residues in SIMONA. Section 3.2.2 summarizes how this can be done in SIMONA.

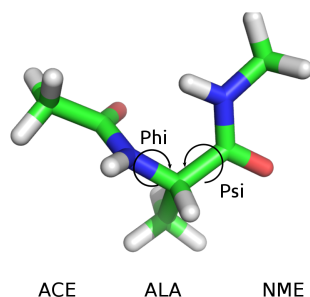


Figure 3.4.: An alanine dipeptide is composed out of the alanine amino acid with neutral peptide caps ACE and NME on both sides. The free energy landscape is sampled and projected onto the phi and psi backbone dihedrals.

For each dipeptide, MC simulations with 20 million steps and all dihedrals as degrees of freedom were performed at 300K. The dihedral space  $[-\pi/+ \pi]$  for  $\Phi$  and  $\Psi$  was divided into 50 equal sized bins. The free energy could be calculated with the occurrence  $Z$  of a given dihedral pair in the generated ensemble:

$$\Delta G(\Phi, \Psi) = -RT \ln(Z(\Phi, \Psi)). \quad (3.8)$$

In SIMONA energies are given in kcal/mol. For the comparison with other free energy plots of dipeptides computed by others, the values are converted to kJ/mol with the factor 4.1868. The plots in Figure 3.5 are generated with matplotlib [77]. Free energies above  $40 \text{ kJ/mol}$  are coloured white. These energetically disfavoured regions arise mainly due to Lennard-Jones clashes when different van der Waals radii overlap.

---

### 3.3. Validation of Dihedral Angle Distributions of Dipeptides in Monte Carlo Simulations

---

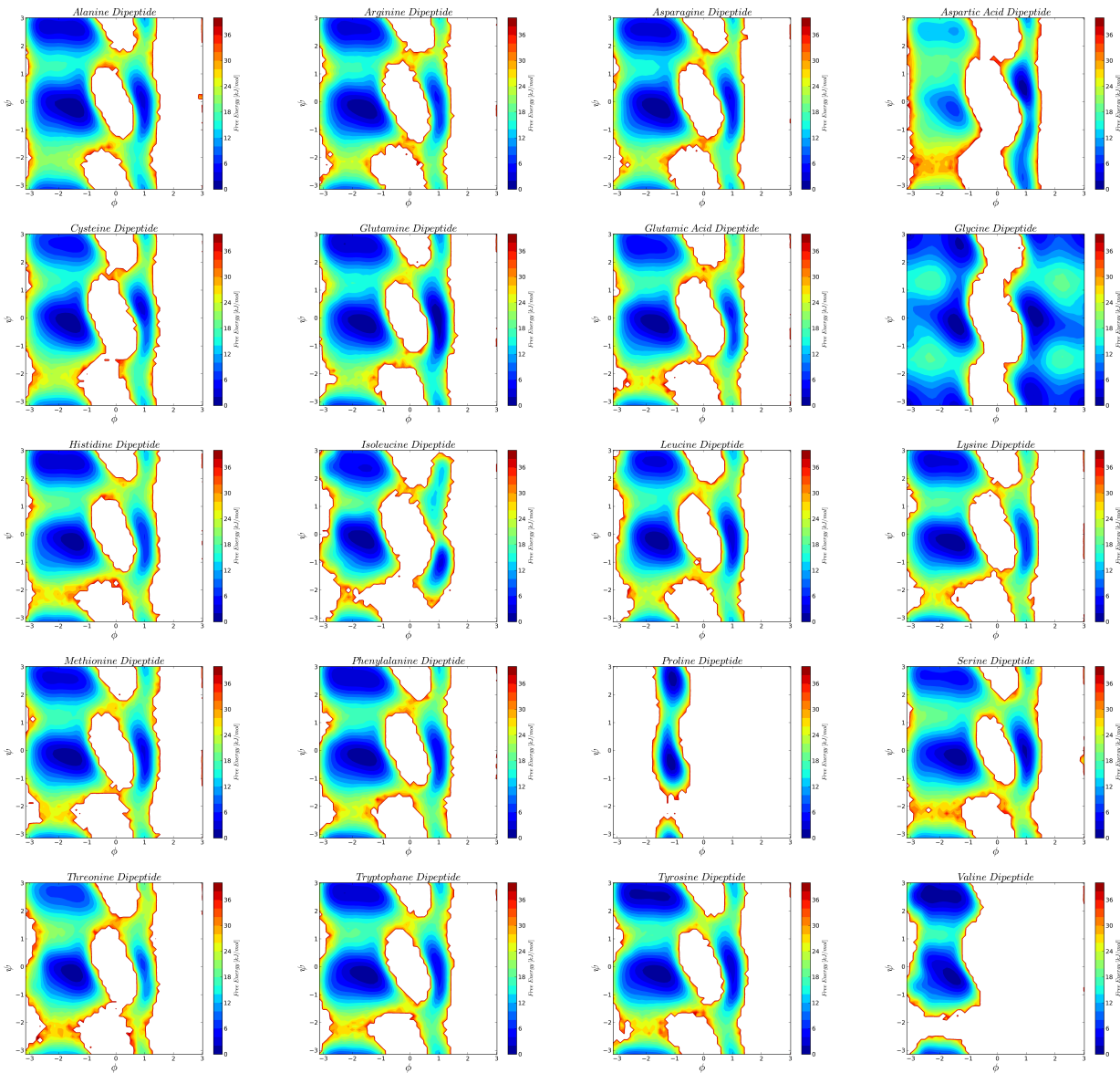


Figure 3.5.: Free energy landscape of dipeptides. Most of the plots show the typical minima for  $\alpha$ -helices,  $\beta$ -sheets and left-handed helices.

Vymetal et al. [78] performed dipeptide MD simulations with GROMACS [74] and used the AMBER99SB force field [58].

A comparison of the alanine dipeptide, Figure 3.6, shows reasonable agreement. MD simulations with additional degrees of freedom (see also Section 3.2) have smaller forbidden areas. Bonds can be stretched and angles can bend, so the peptide can avoid Lennard-Jones clashes, which results in a smoother in-

crease of the energy towards prohibited areas. In general, the computed free energy landscapes show that all dipeptides possess their typical minima in the free energy landscape:  $\alpha$ -helix,  $\beta$ -sheet and left-handed helix. Noticeable are aspartic acid, glycine, isoleucine, proline and valine (see Figure 3.5).

The amino acid proline has a covalent bond between the side chain and the nitrogen of the peptide backbone. Therefore the dihedral angle  $\phi$  is in a five-membered ring and rather rigid. Proline has the largest energetically disfavoured regions. In contrast, the amino acid glycine, with only a hydrogen atom as side chain, shows the least restricted free energy landscape. Valine has a very compact form, with a methyl group as side chain. Clashes with the side chain are likely. Beside valine, isoleucine never samples regions of a left-handed  $\alpha$ -helix. These findings are in agreement with the results of Feig et al. who reported that isoleucine and valine never sample the area of left-handed helices due to unfavourable side chain backbone interactions [79].

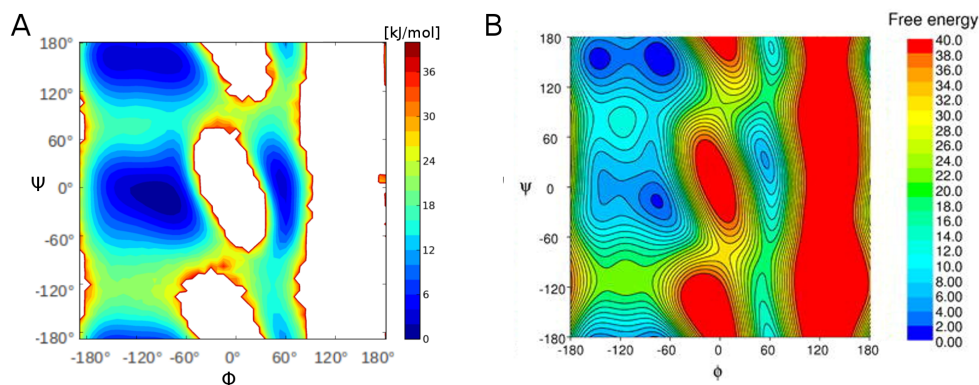


Figure 3.6.: Comparison of alanine dipeptide free energy landscapes generated with SIMONA MC simulations (panel A) and MD simulations by Vymětal et al. (panel B) [78] (copyright (2011), Elsevier) show agreeing minima, but steeper transitions to prohibited areas. MC simulations are performed without degrees of freedom for bond length and bond angles (see Section 3.2).

### 3.4. Protein Stability in Monte Carlo Simulations

Proteins are involved in almost all biological processes, so their structure and conformational changes are of great interest to deduce their functions. Recent progress in hard- and software enables folding studies of small proteins with MD simulations [39, 80]. Unfortunately, the high costs and need for specialized hardware, only available for a few scientists, generates demand for an alternative method.

We believe that MC simulations with SIMONA will be such an alternative, because they do not suffer from the timestep problem of MD and are computationally efficient due to implicit solvent. To test the method, protein stability studies have been carried out.

First stability simulations with SIMONA show promising results. Reproducible folding and unfolding events could be observed using single CPU core MC simulations. These results suggest that MC methods could provide a widely accessible alternative, but have to be investigated further. First results are summarized here for the villin headpiece mutant 2f4k [81] and the WW-domain 2f21 [19].

### 3.4.1. Villin Headpiece

The chicken villin headpiece is known as a fast folding three helix bundle [81] (Figure 3.7). Nana Heilmann investigated mainly the folding of the PDB structure 1vii [82] in her diploma thesis [83] while I studied the mutant with the PDB code 2f4k [81].

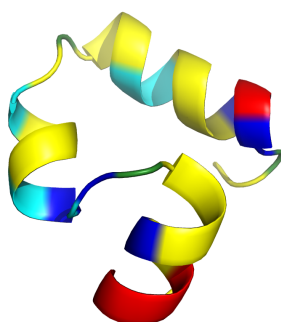


Figure 3.7.: Villin headpiece is comprised of 35 amino acids and folds into a three helix bundle. Positive or negative charged amino acids are coloured in blue and red, special cases and polar or hydrophobic amino acids in green, cyan and yellow. The sequence of the mutant 2f4k contains a histidine residue, by default uncharged in SIMONA simulations.

The substitution of two lysine residues with norleucine stabilizes the protein by 1 kcal/mol and increases the folding rate [81]. Differences between the mutants are displayed in Figure 3.8. Norleucine is a non standard amino acid and an isomer of leucine used for experimental studies.

Figure 3.9 shows the different chemical structures of leucine (panel A) and the norleucine isomer (panel B). The parametrization of the new residue is discussed in Section 3.2.2.

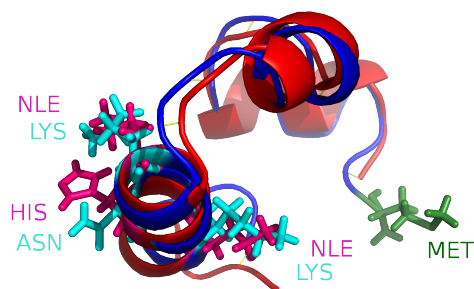


Figure 3.8.: Comparison of the villin headpiece structure (PDB 1vii) in blue and a mutant (PDB 2f4k) in red. Three residues are substituted (two lysine residues and an asparagin). The coil region is shorter by one residue.



Figure 3.9.: Chemical structure of the amino acid leucine (A) and its isomer norleucine (B).

The experimental folding temperature of the villin mutant is 361K [81]. Simulations with SIMONA show a completely stable protein around the experimental folding temperature, so simulations at higher temperatures (between 380K and 480K) were carried out. Simulations of other proteins as well as the villin simulations by Nana Heilmann [83] also show such differences between the computed and experimental folding temperatures. Since this was not observed in explicit water MD simulations [39, 80], possible explanations are the implicit solvent model or the missing degrees of freedom in SIMONA. This has to be investigated further.

To analyse protein folding or stability simulations, calculating the root mean square deviation (RMSD) [84] of each conformation compared to the native state of the protein is very common. Structures with low RMSD values are folded, while higher RMSD values indicate that a protein is partially or fully unfolded. Another possibility is to define a reaction coordinate  $Q$  [85], e.g. the number of native contacts. These can be calculated based on the method proposed by Noel et al. [86]. The protein in its

native conformation has a high fraction of native contacts (around 0.7). The number decreases when the protein unfolds. Piana et al. reported that a reaction coordinate based on the formation of native contacts is a good variable to study the folding of complex proteins like ubiquitin [87].

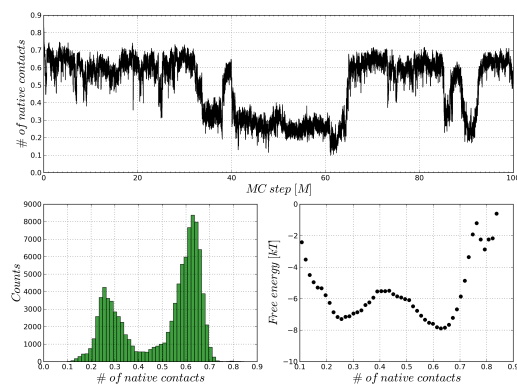


Figure 3.10.: Q-values (native contacts) based on a shadow-map [86] and free energy landscape for a villin mutant simulation at 440K.

Figure 3.10 shows the free energy plot in combination with a q-plot for a simulation at 440K and all dihedrals as degrees of freedom. The plots show a slight preference of the folded state and some transitions between folded and unfolded conformations. Analysing the corresponding RMSD-plot in Figure 3.11, five snapshots illustrate the transitions.

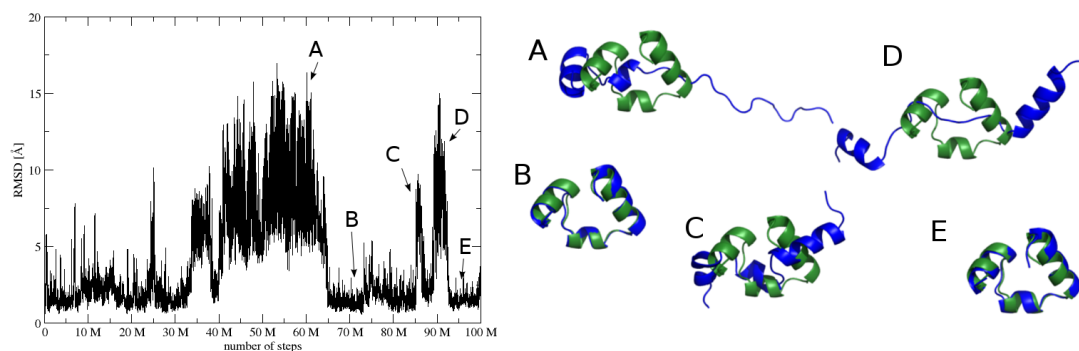


Figure 3.11.: RMSD plot for a simulation at 440K of the villin mutant 2f4k. The native conformation is coloured in green, snapshots out of the simulation in blue. Unfolding (conformation A, C, D) and refolding (conformation B, E) can be observed.

The unfolded structures, snapshots A, C and D in Figure 3.11, have RMSD values of  $8.79\text{\AA}$  (snapshot C - step 83.992.000) or  $16.11\text{\AA}$  and  $14.99\text{\AA}$  (snapshot A - step 60.165.000 and D - step 90.495.000).

Refolding events like snapshot B (step 72707) or snapshot E (step 938949) show a  $C_\alpha$ -backbone RMSD of 0.59 or 0.91Å.

### 3.4.2. WW Domain

The WW domain folds into a three stranded  $\beta$ -sheet (Figure 3.12) and is comprised of 35 amino acids [19].

100 million MC steps at simulation temperatures between 460K and 500K and all dihedrals as degrees of freedom were carried out. The analysis in this section is performed with 20 simulations at 490K.

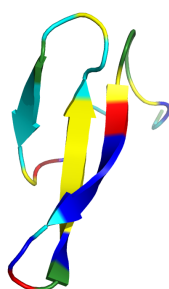


Figure 3.12.: The 35 amino acid protein WW domain folds into a three stranded  $\beta$ -sheet. Positive or negative charged amino acids are coloured in blue and red, special cases and polar or hydrophobic amino acids in green, cyan and yellow.

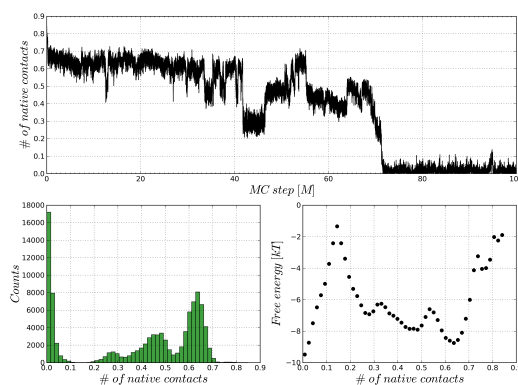


Figure 3.13.: Free energy and q-plot for a WW domain simulation at 490K.

Figure 3.13 shows the free energy plot and the q-plot for the native contacts. The plots suggest that the simulation temperature is above the folding temperature where folded and unfolded structures are equally likely. Copies with the same simulation set up show similar results. While some of the simulation show unfolding and refolding events, most of the simulations show a complete absence of secondary structure after several million steps. In all simulations, unfolding intermediates could be observed.

Analysing the RMSD plot for the WW domain at 490K (Figure 3.14), different intermediates can be identified. Conformation B (step 43.525.000) with an RMSD value of 11.93Å has only two  $\beta$ -strands left and a kink in the loop between the remaining sheets. The main contribution to the RMSD of 10.34Å of conformation D (step 59.003.000) is due to the coil regions of both termini. The refolded conformation C (step 53.449.000) shows an RMSD of 1.47Å while the completely unfolded conformation E (step 77.222.000) has an RMSD of 29.02Å.

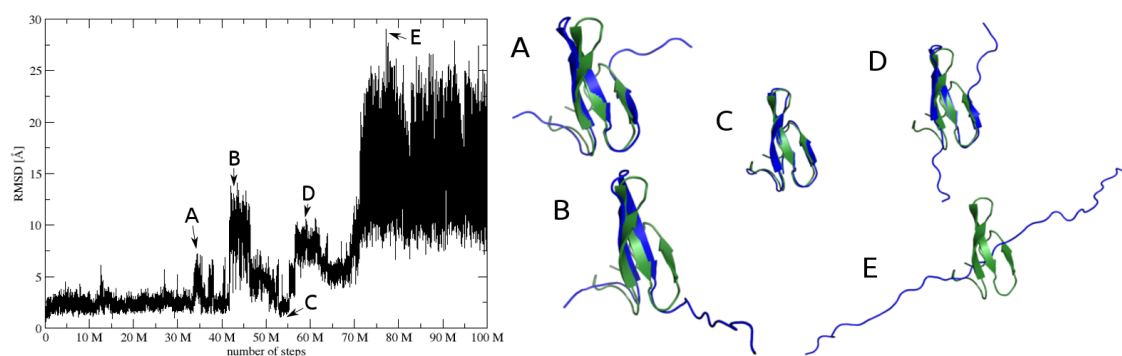


Figure 3.14.: RMSD plot for a simulation at 490K of the WW domain 2f21. The native conformation is coloured in green, snapshot out of the simulation in blue. Unfolding (conformation A, B, D) and refolding (conformation C) can be observed. The simulation temperature is too high, wherefore the protein ends with a completely unfolded structure with no contacts left (conformation E).

Simulations with lower temperatures are more promising, but the right temperature must be found in additional simulations in the future or with advanced techniques like parallel tempering (PT) [88].

Nevertheless protein stability simulations with SIMONA show first promising results. A protein folding process can be also sampled using conventional computer architectures. Investigations of other fast-folding proteins and additional simulations with proteins having a mixed sheet/helix structure are still ongoing.

## 3.5. Small Molecule Hydration Free Energies

*This work will be published in [1] and is used here in agreement with all authors.*

The correct estimation of hydration free energies (HFE) is very important, for instance, for drug discovery and the prediction of binding affinities [89–91]. Furthermore force fields for simulations of molecules in solution should be able to reproduce HFEs with reasonable accuracy, thus providing a good test case.

Unfortunately, recent studies show a gap in the errors of estimating HFEs between explicit TIP3P solvent and implicit solvent models [72, 92].

How to improve this situation is an open question. To address this question, we provide a thorough performance comparison of three GB models with different nonpolar terms to estimate HFEs. We have optimized parameters for these models for two sets of atom types. The results published in Brieg et al. [1] show that implicit models are able to reproduce experimental HFEs with the same or higher accuracy than explicit TIP3P simulations [1].

### 3.5.1. Solvation Free Energy

The solvation free energy can be separated in an electrostatic and a nonpolar contribution [93] also mentioned in the force field Section 3.2:

$$\Delta G = \Delta G_{GB} + \Delta G_{NP} \tag{3.9}$$

GB models like GBMV [94] or GB models using PowerBorn radii offer the same accuracy like Poisson-Boltzmann calculations [63]. Therefore the focus of this study was the contribution of the nonpolar part. Nonpolar solvation effects are often described by a SASA term. This term describes the work required to form a cavity for the solute inside the solvent and the dispersion interactions between solvent and solute [62].

In the literature, extensions of the SASA based energy evaluation, like including the volume of the cavity or explicit modelling of dispersion interactions, are proposed to improve the accuracy of nonpolar

models [67–71, 95–97].

### 3.5.2. Nonpolar Solvent Interaction Models

- NP1 is a simple nonpolar model that penalizes cavity formation in water based on a SASA term. The penalty is proportional to the surface area of the cavity via the surface tension  $\gamma$  [97].

$$\Delta G_{NP1} = \gamma \sum_{i=1}^N A_i \quad (3.10)$$

- Eisenberg et al. and Ooi et al. suggested to replace the global surface tension value with one for each atom type [65, 66].

$$\Delta G_{NP2} = \sum_{i=1}^N \gamma_i A_i \quad (3.11)$$

- Additional to the SASA term, a repulsion and an attractive dispersion term are used in the most complex model [67, 68, 70, 71, 95–97].

$$\Delta G_{NP3} = \gamma \sum_{i=1}^N A_i + p \sum_{i=1}^N V_i - \sum_{i=1}^N \frac{\alpha_i}{(R_i + B)^3} \quad (3.12)$$

In addition to the free parameters of the NP part, summarized in table 3.2, each parameter set contains the  $1+N$  parameters of the GB part.  $N$  is the number of atomtypes, in this case the number of elements.

Table 3.2.: Different nonpolar solvent models and their number of free parameters.

	NP1	NP2	NP3
number of parameters	1	N	N+2

### 3.5.3. Data Set and Model Parametrisation

For this study, a database provided by David Mobley [92] with 499 small molecules was used. The data includes vacuum and implicit solvent trajectories, generated with AMBER, and the experimental HFEs.

According to Mobley et al., the energy for the lowest energy snapshots from the vacuum trajectory

should be in good agreement with the HFE resulting from the whole trajectory [92].

To find the lowest energy snapshot, all energies for the vacuum trajectories were recalculated using the general AMBER force field (GAFF) [98, 99] with AMBER11 [43].

For the parametrisation the solvation free energy (equation 3.9) for the lowest energy vacuum snapshot was calculated using AM1-BCC charges [100, 101] and the model parameters. Optimization goal was the minimization of the root mean square error (RMSE) to the experimental HFEs by finding suitable parameters for the different GBNP models.

$$RMSE_{fit} = \sqrt{\frac{1}{N} \sum_i^N (\Delta G_{GB}^i + \Delta G_{NP}^i - \Delta G_{exp}^i)^2} \quad (3.13)$$

The parametrisation was performed 81 times in two steps, one global optimization with the particle swarm optimization method by Kondov et al. [102], followed by a local minimization using Powells method [103] implemented in the SciPy package.

#### 3.5.4. Assessment of Nonpolar Solvent Interaction Models

Knight et al. showed in their survey that a gap between hydration free energies of implicit solvent and explicit TIP3P simulations exists [72]. For the explicit TIP3P simulations, Mobley et al. found a root-mean-square error (RMSE) of  $RMSE_{HFE} = 1.26 kcal/mol$  and a correlation coefficient of  $R^2 = 0.888$  [104]. In the survey, it turned out that the GBSW model [105] has the lowest RMSE with  $1.52 kcal/mol$ , GBMV [94] the best correlation coefficient  $R^2 = 0.809$  [72].

For a comparison between the NP models (Section 3.5.2) with explicit TIP3P simulations [104] or the GBSW [105] and GBMV [94] model, the HFEs are computed using the Multistate Bennett acceptance ratio method [106]. Besides vacuum trajectory energies, the method requires energies of the implicit solvent trajectories, which are calculated using AMBER [43].

HFEs computed with the models GBNP1, GBNP2 and GBNP3 are summarized in table 3.3.

While GBNP1 still shows a gap between the accuracy of implicit and explicit HFEs, GBNP2 outper-

Table 3.3.: RMSE of the solvation free energy parametrisation and the HFEs of the trajectories for the different nonpolar models in comparison to the explicit TIP3P results by Mobley et al.[104]. The last column shows the correlation coefficient of the hydration free energies.

	$RMSE_{Fit}[kcal/mol]$	$RMSE_{HFE}[kcal/mol]$	$R^2$
GBNP1	1.32	1.30	0.826
GBNP2	1.00	0.99	0.900
GBNP3	1.21	1.19	0.853
TIP3P [104]	–	1.26	0.89

forms the results of the TIP3P and the implicit competitor models with a smaller  $RMSE_{HFE}$  and a higher correlation coefficient. Although GBNP3 is the most complex model in the study and has the highest number of parameters, it performs worse than GBNP2. All GBNP models perform better than the implicit models investigated by Knight et al. [72].

Figure 3.15 shows the HFEs for the GBNP2 model, compared to the experimental HFEs.

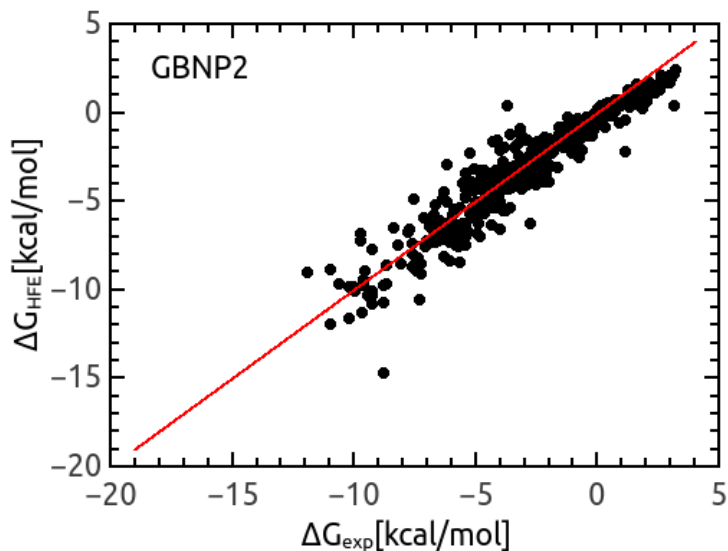


Figure 3.15.: Comparison of computed HFEs to experimental HFEs for a set with 499 small molecules. The RMSE for the data calculated with the GBNP2 model  $RMSE_{HFE} = 0.99kcal/mol$  and the result of fitting single conformation solvation free energies to experimental HFEs  $RMSE_{fit} = 1.00$  are nearly identical. The GBNP2 model outperforms the results of explicit TIP3P HFEs. The correlation coefficient of the GBNP2 model is with  $R^2 = 0.900$  slightly higher than the  $R^2$  of the explicit calculations [1].

To investigate the possibility of adding more parameters by additional atomtypes, the molecules were grouped by the elements they are comprised of and the RMSEs were calculated for these groups (see table 3.4).

Table 3.4.: Root-mean-square errors for each element for the GBNP3 model.

	N	F	O	I	S	P	Br	Cl
$RMSE_{HFE}$ [kcal/mol]	1.76	1.56	1.41	1.18	0.84	0.82	0.56	0.24

Molecules containing nitrogen, fluorine and oxygen show the largest RMSEs. The largest outlier for fluorine molecules is hexafluoropropene, which also shows large deviations of the explicit HFE estimate to the experimental values. Since both models use the same partial charges, this could be one reason for the large error. The RMSE for the fluorine molecules discarding hexafluoropropene leads to an RMSE of  $1.04\text{kcal/mol}$ . Very often outliers with oxygen also contain nitrogen atoms, so that a new nitrogen atom type could lead to an improved accuracy. To further examine molecules with nitrogen atoms, different AMBER atomtypes [98, 99] can be distinguished. Figure 3.16 shows the HFEs for molecules containing nitrogen atoms.

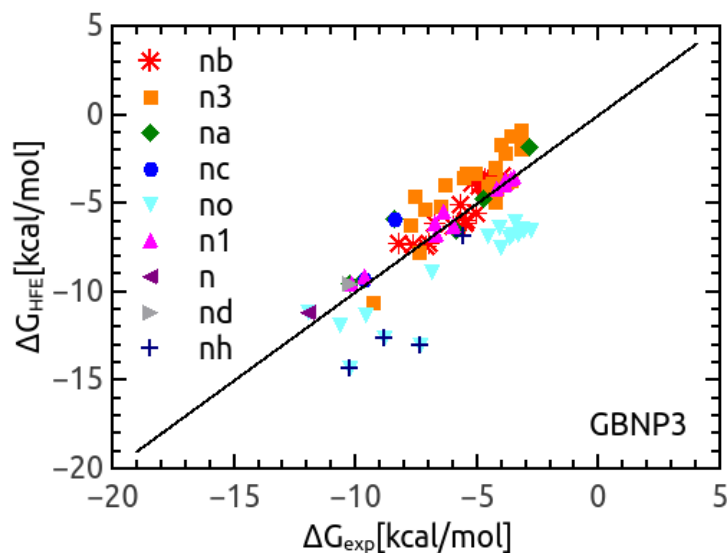


Figure 3.16.: Hydration free energies of molecules containing nitrogen atoms. The energies are calculated with the GBNP3 model [1].

The “no” atoms (triangle down, cyan, in Figure 3.16) show a strikingly low agreement with systematic

more negative computed HFEs than experimental HFEs. This can be understood by looking at the partial charges of the nitrogen atoms. While all other nitrogen atom types are negatively charged, “no” atoms carry a positive partial charge. This difference influences the solvation properties and is known as the asymmetry of water [107–109]. In our first parametrization, all nitrogens have the same parameter, but an additional nitrogen atom type to distinguish between these two opposite charged nitrogen atom types can be established.

Repeating the parametrization procedure with two nitrogen atom types, “nn” for negatively charged nitrogens, “np” for positively charged atoms, the RMSE for the molecules with nitrogen atoms decreases from  $1.76\text{kcal/mol}$  to  $1.13\text{kcal/mol}$ . Improved RMSEs for the comparison of computed and experimental HFEs of the GBNP\* models with a second nitrogen atom type are summarized in table 3.5.

Table 3.5.: RMSEs of the solvation free energy parametrization and the HFEs computed from the trajectories for the different nonpolar solvent models with a second atomtype for nitrogen in comparison to the explicit TIP3P results by Mobley et al.[104]. The last column shows the correlation coefficient of the HFEs.

	$RMSE_{Fit}[\text{kcal/mol}]$	$RMSE_{HFE}[\text{kcal/mol}]$	$R^2$
GBNP1*	1.17	1.16	0.860
GBNP2*	1.00	0.96	0.903
GBNP3*	1.04	1.01	0.894
TIP3P [104]	–	1.26	0.888

The GBNP2\* model still performs better than GBNP1\* or GBNP3\*, although GBNP3\* comes very close to its performance with the new parameterization. All three models show lower RMSEs than the explicit TIP3P water model, but the squared correlation coefficient of GBNP1\* is still worse than that of TIP3P [1].

The comparison of the performance of three generalized Born based implicit solvent models with different nonpolar contributions to estimate experimental hydration free energies shows that the gap [72] in the errors between explicit TIP3P solvent and implicit models can be closed. It turns out that the most common nonpolar term (GBNP1) performs worst in combination with our optimized parameters. The most complex model in the investigation (GBNP3) improves the accuracy of the HFEs but has also a much larger set of free parameters. The best performing model is GBNP2 with an atom

type dependent surface tension coefficient as proposed by Eisenberg et al. [65] and Ooi et al. [66]. For the future, studies should investigate how these models and parameters, which are optimized for small molecules, perform for macromolecules like proteins. Accounting for the asymmetry of water in the parameterization via a new atom type resulted in better agreement between estimated HFEs and experimental values for all models, suggesting this as a general strategy for improving any GB based implicit solvent model [1].

## 4. An Improved Generalized Born Implicit Membrane Model - SLIM: Model, Simulations and Results

*Part of this work is accepted for the publication in the Journal of Computational Chemistry [2] and used here in agreement with all authors.*

Simulations of complex biological environments, such as lipid bilayers remain a very challenging task. Due to the complexity and size of such systems, most of the computer time is spent on computing the surrounding environment instead of the membrane protein which is of scientific interest. Although explicit membrane simulations provide a very detailed representation, implicit membrane models offer a computational less expensive alternative.

SLIM [2] is a generalized Born (GB) based implicit membrane model, which combines advantages of other previous published models and therefore outperforms these models regarding the accuracy of electrostatics in the membrane. While implicit and explicit simulations in general are discussed in Chapter 3, section 4.1 describes GB based implicit models. The implementation of the model itself and differences to other GB based models are summarized in section 4.2. To validate energies calculated with SLIM, a comparison to Poisson-Boltzmann (PB) reference calculations is presented in section 4.3. The effects of our model parameters are investigated in Monte Carlo simulations of three well studied membrane proteins: Melittin of bee venom (section 4.4), the transmembrane domain of the M2 protein (section 4.5) and the transmembrane domain of Glycophorin A (section 4.6). Comparisons to other

computational and experimental studies show reproducibility of properties and behavior in simulations using the SLIM model for these three proteins.

## 4.1. Generalized Born Based Implicit Membrane Models

In implicit models, the solvation free energy (see also section 3.2) can be modeled by separating it into a polar part, describing electrostatic effects, and a nonpolar part [93]:

$$\Delta G = \Delta G_{elec} + \Delta G_{np} \quad (4.1)$$

While the nonpolar part of equation 4.1 is usually modeled by a SASA term (see also Chapter 3.2 and 3.5), the electrostatic interactions between the environment and the molecule can be approximated via the PB equation [61]. Due to the high computational cost of solving the associated partial differential equations, it is common to model the electrostatic interactions with a GB model, using Still's formula (equation 3.5) [62].

GB models are limited to two dielectric regions. For a model of the membrane environment in addition to implicit water, consideration of more than two regions with different dielectric constants is required. In addition to the protein and the water region, at least one low dielectric membrane region is necessary. Spassov et al. [110] avoid the problem of only two dielectric regions by treating membrane and protein as one region with the same dielectric constant. Electrostatic effects caused by the membrane are encoded in the Born radii, so all atom positions relative to the membrane are considered. Im [111] and Ulmschneider [112] also published implicit membrane models based on this work.

Tanizaki et al. [113] proposed another method to incorporate the membrane in the GB approach. They use a local dielectric constant  $\epsilon(r)$  which varies between the dielectric constant of the membrane and that of the surrounding water. In contrast to the Spassov model, they can include any number of additional dielectric regions, also with different dielectric constants. A disadvantage of the model is that some features of PB electrostatics cannot be modeled. This will be discussed in section 4.3).

The possibility to include more than two dielectric regions while membrane induced electrostatic effects are encoded in the Born radii turns the SLIM model to a promising alternative to other implicit

membrane models. The implementation in the MC package SIMONA [54] will provide an easy accessible tool free of charge for the scientific community.

## 4.2. SLIM - SIMONA Layered Implicit Membrane

SLIM [2], an improved GB based implicit membrane model, was developed together with Martin Brieg and Carolin Seith as part of this thesis. As mentioned in the previous section, SLIM combines the advantages of the models by Spassov et al. [110] and Tanizaki et al. [113]: Accurate GB energies close to PB energies and the possibility to include several dielectric slabs to model the membrane.

For the implicit membrane three different dielectric slabs are used:

- The **membrane core region**  $V_c$  with a dielectric constant  $\epsilon_c$  and a thickness  $h_c$
- Next to the core region **two headgroup regions**  $V_h$  with  $\epsilon_h$  and  $h_h$
- A infinite **implicit water region**  $V_w$  with  $\epsilon_w$  encloses the membrane

In the literature, membrane models with different numbers of dielectric slabs are discussed: They vary between only one slab for the membrane [110–113] or multi layer dielectric profiles [114]. In between, models with for instance two (core and headgroup region) or four (hydrocarbon tail, ester group, head group, interfacial region) can be found [113]. Tanizaki et al. investigated membrane models with

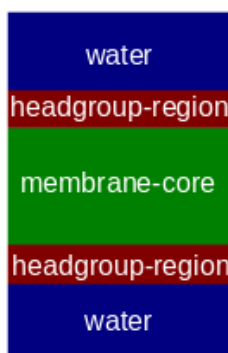


Figure 4.1.: In a three dielectric continuum model of a membrane-water system, a membrane core region, a headgroup region and the bulk water region can be distinguished.

different numbers of additional layers and showed that three different dielectrics (see Figure 4.1) are sufficient to model a biological membrane and the surrounding water [113].

To model these three different slabs in the SLIM model, the polar part of the solvation free energy  $\Delta G_{elec}$  can be described by a sum of two GB terms.

$$\Delta G_{elec}(\epsilon_c, V_c; \epsilon_h, V_h; \epsilon_w, V_w) \approx \Delta G_{GB}(\epsilon_c, V_c; \epsilon_h, V_h \cup V_w; \{R\}_1) + \Delta G_{GB}(\epsilon_h, V_c \cup V_h; \epsilon_w, V_w; \{R\}_2) \quad (4.2)$$

This approach is also depicted in Figure 4.2 and offers the possibility to consider membrane effects on electrostatic interactions with the assumption by Spassov et al. encoded in the Born radii.

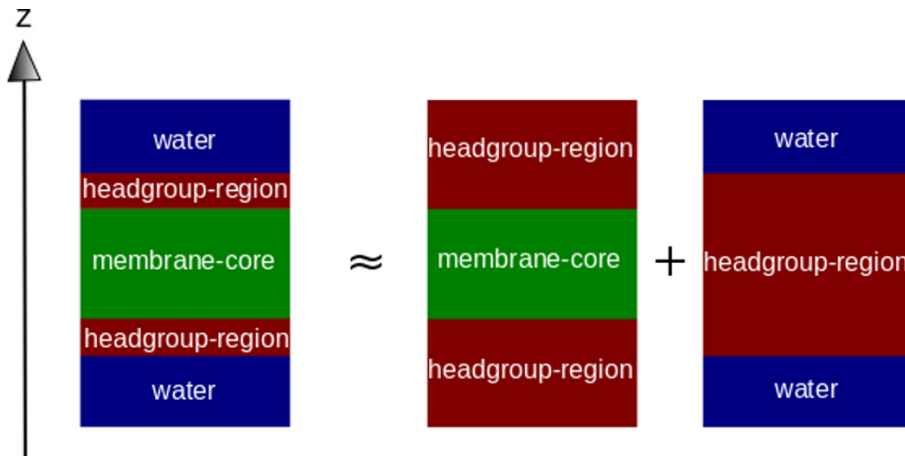


Figure 4.2.: Sketch of decomposing a biological membrane model with regions of three different dielectric constants into a sum of two models with only two different dielectric regions each, for which the electrostatic part of the solvation free energy can be computed using a standard generalized Born model [2].

For every single GB term a different set of Born radii  $\{R\}_i$  is necessary. They can be computed with the fast and accurate PowerBorn method [63] implemented in SIMONA [54]. The necessary modifications and extensions of the PowerBorn algorithm are summarized in Setzler et al. [2]. Furthermore, values for the dielectric constants and dimensions of the two membrane regions are required for computing the polar part of the solvation free energy. For the first summand of equation 4.2 (see also fig. 4.2), protein and membrane core have the same dielectric constant  $\epsilon_p = \epsilon_c$ , the headgroup and water region are merged  $V_h \cup V_w$  and have the same dielectric constant  $\epsilon_h$ . For the second summand (fig. 4.2 and

equation 4.2), the dielectric constant for protein and membrane core are set to the dielectric constant of the headgroup region  $\epsilon_p = \epsilon_c = \epsilon_h$  and both membrane regions are merged  $V_c \cup V_h$ .

When the protein is far away from the membrane, the SLIM model converges into an implicit GB water model, due to the fact that contributions by the membrane to the Born radii are negligible and therefore all terms of the right hand side of equation 4.2 will have the same set of Born radii and Still's formula (equation 3.5) is additive if the same set of Born radii is used [2].

Using only one dielectric for the membrane, the SLIM model resembles that of Spassov et al. [110], but uses a different underlying method to compute the Born radii.

To model membranes composed of different lipids, the parameters (thickness and dielectric constant) for the slabs have to be adapted. Standard settings for the SLIM model are discussed in section 4.3. The total membrane thickness  $h_m$  is the sum of the core and two headgroup regions:  $h_m = h_c + 2h_h$ . The membrane normal is the direction of the z-axis and the membrane center is taken to be  $z=0$  in the following.

To complete the solvation free energy, the nonpolar part of equation 4.1 needs to be modeled. Normally a SASA based term is used, which can be adapted by a scaling function  $S(z_i)$  like proposed by Tanizaki et al. [113]:

$$\Delta G_{np} = \gamma \sum_{i=1}^n S(z_i) A_i \quad (4.3)$$

$$S(z) = \begin{cases} c(|z| - z_a)^2(3z_b - 2|z| - z_a)/(z_b - z_a)^3 & (0 \leq |z| < z_b) \\ (1 - c)(|z|^2 - z_b^2)^2(3z_c^2 - 2|z|^2 - z_b^2)/(z_c^2 - z_b^2)^3 & (z_b \leq |z| < z_c) \\ 1 & (\text{otherwise}). \end{cases} \quad (4.4)$$

with the parameters  $c = 0.32$ ,  $z_a = 0.5$ ,  $z_b = 9.2$  and  $z_c = 25\text{\AA}$ .

They use a membrane with a thickness  $h_m = 30\text{\AA}$  and for membranes with  $h_m \neq 30\text{\AA}$  the scaling function  $S(z)$  in equation 4.3 will be stretched or compressed in the SLIM model:

$$\tilde{S}(z_i) = S\left(\frac{30.0}{h_m} \cdot |z_i|\right) \quad (4.5)$$

### 4.3. Comparison with the Poisson-Boltzmann Model

Solving the PB equation is an accurate but also computationally very expensive way of computing the electrostatic component of solvation free energies. SLIM uses the less expensive GB alternative, therefore comparative calculations should be performed to ensure reasonable errors with respect to PB calculations.

The simplest test is to pull a single ion through the membrane and to compare the profiles of the electrostatic self-energy. Self-energy terms are described by terms with  $i=j$  in equation 3.5.

PB calculations were performed with the PBEQ solver [115, 116]. All settings for the PBEQ-solver can be found in the Appendix A. The membrane geometry for PB calculations was chosen as proposed by Tanizaki et al. [113], with  $\epsilon_c = 2$ ,  $h_c = 20\text{\AA}$  for the membrane core and a headgroup region with  $\epsilon_h = 7$ ,  $h_h = 5\text{\AA}$  on both sides of the core. The membrane has a total thickness of  $h_m = 30\text{\AA}$  and is embedded in implicit water with  $\epsilon_w = 80$ . To compare SLIM energies with the PB profile, the same parameters as for the PB calculations were used. Additional modified parameters for the SLIM model were tested. A calculation with only one membrane dielectric to resemble Spassov's model completes the PB comparison. The profiles are shown in Figure 4.3, all parameters are summarized in table 4.1.

For the Spassov like model (blue) a much steeper transition compared to the PB energies (black) can

Table 4.1.: Different membrane parameters used for the PB and GB comparison.

model	$h_c[\text{\AA}]$	$h_h[\text{\AA}]$	$\epsilon_c$	$\epsilon_c$	$\epsilon_w$	color and style
PB	20	5	2	7	80	solid black line
GB	20	5	2	7	80	dotted red line
GB	22	4	2	6	80	dashed orange line
GB	30	-	2	-	80	dot-dashed blue line

be observed. The GB model with the same parameters as in the PB calculation provides a smoother transition (red). Deviations to the PB results occur mainly near the slab interfaces around  $z = 10\text{\AA}$ . Using modified parameters  $h_c = 22\text{\AA}$  and  $\epsilon_c = 6$  results in good agreement between PB calculations and the SLIM model.

The second test uses a more complex structure. A protein with all charges set to zero except one allows

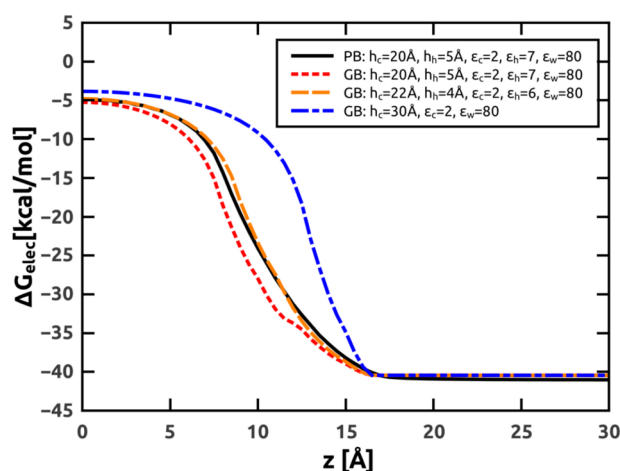


Figure 4.3.: Comparison of the electrostatic solvation free energy profile from PB calculations (solid black line) to our proposed GB based SLIM model with the same membrane parameters as in PB (dotted red line), with modified membrane parameters (dashed orange line), and with only one low dielectric slab resembling the model of Spassov et al. [110] (dot-dashed blue line) for pulling a single ion through a membrane [2]

a more advanced test. The native conformation of Magainin (pdb code: 2MAG [117]) in three different orientations was pulled through the membrane.

The helices are oriented more or less horizontally (blue helix) or vertically (green and magenta helices) in the membrane as displayed in Figure 4.4A. The charge is located at the  $C_\alpha$ -atom of residue *Asn22* and displayed in Figure 4.4 as a red sphere between the three helices. The  $z$ -values of the profile always correspond to the location of the charge. The profiles in 4.4B show that conformations with the uncharged part of the protein inside the membrane and the charge close or in the headgroup region are energetically favoured compared to the other orientations with the charge at the same position. A comparison of the green and magenta helix with the charge located at  $z = 10\text{\AA}$  (Figure 4.4A) illustrates this. Moving the charge deeper into or out of the membrane results in the disappearance of the energy differences between the different orientations.

Implicit membrane models with a dielectric profile, like proposed by Tanizaki et al. [113], are unable to account for such energy differences, because their self-energy depends only on the  $z$ -position of the charged atom and not on the overall orientation of the other atoms with respect to the membrane. Another basic test is to compare the interaction terms of equation 3.5 by calculating the total polar

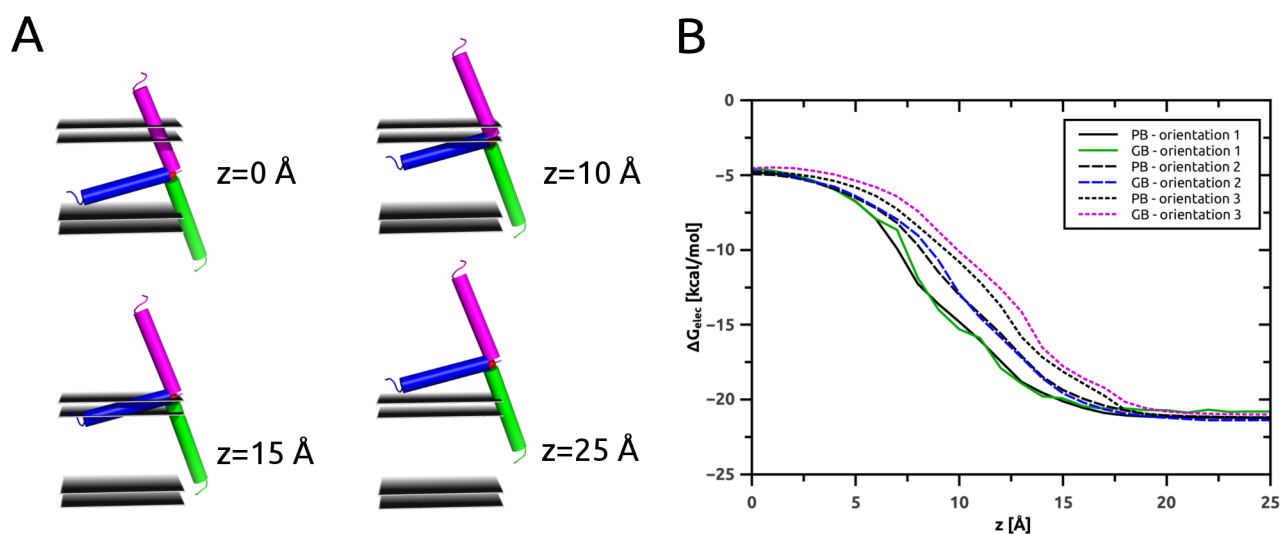


Figure 4.4.: (A) Four snapshots of pulling three different oriented native Magainin conformations through the membrane. The  $z$ -values denote the  $z$ -position of the only charged atom used in this test, which is located in between the helices at the same position for all three orientations (red sphere). (B) Resulting GB based SLIM and PB electrostatic free energy of solvation profiles. Colors of the GB graphs correspond to the colors of the helices in (A) [2].

solvation free energy of two ions and subtracting their self-energies. The ions carry a proton charge and are placed in the membrane center and  $4\text{\AA}$  apart along the  $x$ -direction. One ion is pulled out of the membrane along the  $z$ -direction. The same parameters as summarized in table 4.1 are used. The corresponding profiles are shown in Figure 4.5.

The model with only one dielectric slab (dot dashed blue line) underestimates the energy compared to the PB model (solid black line). The SLIM model with the same parameters as the PB model overestimates the energy up to  $2.19 \text{ kcal/mol}$  (dotted red line) and the SLIM model with improved parameters (dashed orange line) reduces the error to a maximum of  $1.03 \text{ kcal/mol}$ .

The results presented so far show that electrostatic solvation free energies show good agreement between PB calculations and energies calculated with the SLIM model with improved parameters. These parameters are used from now on, unless mentioned otherwise. Remaining variable membrane parameters are the total thickness and surface tension coefficient for the nonpolar part (equation 4.2). The following protein studies and comparisons to experimental results should provide a guide for the right

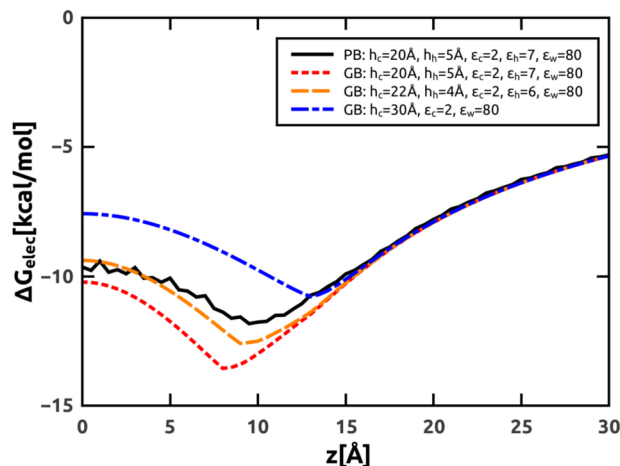


Figure 4.5.: Comparison of the interaction energy between two ions with proton charge placed 4 Å apart along the x-direction in the center of the core region. One is pulled out of the membrane along the z-direction for PB (solid black line), GB with same membrane parameters as PB (dotted red line), GB with improved membrane parameters (dashed orange line) and GB with only one low dielectric slab (dot-dashed blue line) [2]

choice of these parameters, to respect the desired membrane type.

## 4.4. Melittin

Melittin of bee venom is a small, helical, amphipatic membrane protein, which frequently serves as a test system for membrane models [111, 113, 118–120]. For simulations the structure with the PDB-code 2MLT [121–123] composed of the following 26 amino acids was used:

**GLY**<sub>1</sub>- **ILE**<sub>2</sub>- **GLY**<sub>3</sub>- **ALA**<sub>4</sub>- **VAL**<sub>5</sub>- **LEU**<sub>6</sub>- **LYS**<sub>7</sub>- **VAL**<sub>8</sub>- **LEU**<sub>9</sub>- **THR**<sub>10</sub>- **THR**<sub>11</sub>- **GLY**<sub>12</sub>- **LEU**<sub>13</sub>-  
**PRO**<sub>14</sub>- **ALA**<sub>15</sub>- **LEU**<sub>16</sub>- **ILE**<sub>17</sub>- **SER**<sub>18</sub>- **TRP**<sub>19</sub>- **ILE**<sub>20</sub>- **LYS**<sub>21</sub>- **ARG**<sub>22</sub>- **LYS**<sub>23</sub>- **ARG**<sub>24</sub>- **GLN**<sub>25</sub>-  
**GLN**<sub>26</sub>.

The color code corresponds to the code used in Figure 2.2 and in most of the 3D representations of the molecules: **positive** or **negative** charged amino acids in blue and red, **special cases** and **polar** or **hydrophobic** amino acids in green, cyan and yellow. The majority of the Melittin residues is hydrophobic. A few charged residues are located close to the C-terminus, wherefore the protein has an amphiphilic character. The proline residue, known to destroy helical structures [124, 125], in the center of the

sequence causes a kink [126, 127]. The definition of the Melittin kink angle and the structure with coloured residues is shown in Figure 4.6.

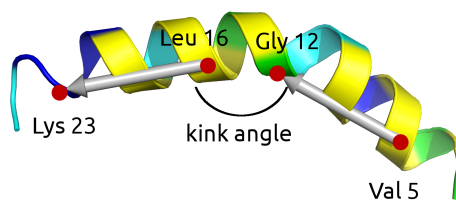


Figure 4.6.: The kink angle for Melittin is defined as the angle between the vectors connecting the  $C_{\alpha}$  atoms of residues Val<sub>5</sub> and Gly<sub>12</sub> as well as Leu<sub>16</sub> and Lys<sub>23</sub>.

While Melittin, an antimicrobial peptide (see also Chapter 5.2), is predominantly bound to the membrane interface with an orientation perpendicular to the membrane normal, a transmembrane orientation parallel to the membrane normal exists as well. The orientation depends on peptide concentration and protonation, membrane composition and thickness. The membrane spanning conformation plays a crucial role in the membrane lytic process [120, 122, 126, 128–132]. Due to the amphiphilic structure Melittin can cover the membrane surfaces or stabilizes pores with the hydrophilic surface facing the pore interior (see also Figure 5.4). These pores make the bacterial membrane permeable and causes the breakdown of the cell. Computer simulations of Melittin should be able to reproduce or predict such a behaviour.

Melittin simulations with the SLIM model are performed to predict the position and orientation of Melittin relative to the membrane. To test the SLIM model the computed values can then be compared to experimental results. Simulations with a total membrane thickness of  $h_m = 30\text{\AA}$  and a surface tension of  $\gamma = 30\text{cal/mol}\text{\AA}^2$  were performed. Three different starting conformations as displayed in Figure 4.7 were chosen:

- A: Conformation similar to an explicit MD simulation result of Bernèche et al. [118] (Figure 4.7A)
- B: Melittin in a orientation perpendicular to the membrane normal in the membrane center (Figure 4.7B)

- C: The peptide in a starting conformation parallel to the membrane normal (Figure 4.7C)

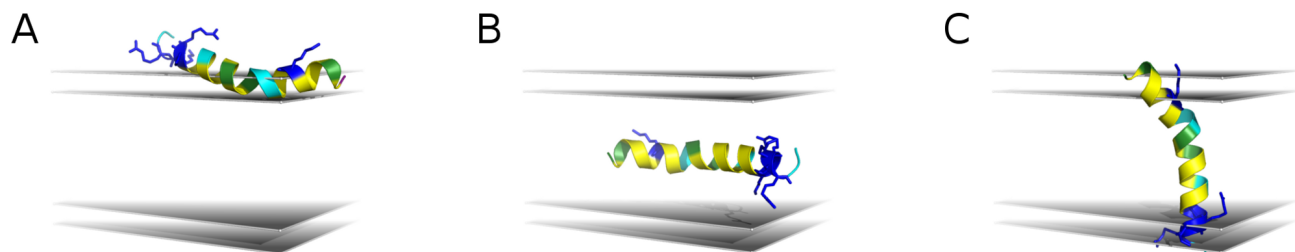


Figure 4.7.: Different starting conformations for Melittin simulations with the SLIM model. The conformations are (A) similar to an explicit MD result, (B) horizontal in the membrane center and (C) parallel to the membrane normal.

20 independent MC simulations with 20 million steps each were performed for all three starting conformations, simulation temperature was 300K. The first one million steps were discarded for the data analysis regarding the sampled orientation and center of mass positions. Figure 4.8 shows histograms for the center of mass probability, the starting conformation is depicted in each histogram.

Starting conformation A remains at the membrane interface and is distributed around  $z = 15.11 \pm 0.9\text{\AA}$ , while conformation C remains parallel to the membrane normal with a center of mass around  $z = 3.75 \pm 0.59\text{\AA}$ . Conformation B, at the beginning completely buried in the membrane, can be found on both interfaces  $|z| = 15.55 \pm 1.0\text{\AA}$  and in a membrane spanning conformation with  $z = 3.77 \pm 0.59\text{\AA}$ . Panel D shows two exemplary conformations corresponding to the two peaks C1 and C2 in the histograms. Similar orientations were also observed in other studies [111, 118, 120, 129].

Hristova et al. showed in x-ray experiments that Melittin in DOPC membranes is gaussian distributed around  $z = 17.5\text{\AA}$  with a width of  $z = 4.3\text{\AA}$  [129]. At a first glance, these findings seems to contradict the SLIM results, but according to Nagle et al., the core of a DOPC membrane is  $27.1\text{\AA}$  thick [133]. The core of the SLIM membrane is with  $22\text{\AA}$  much thinner. Taking this into account, the shift of the peak position can be explained.

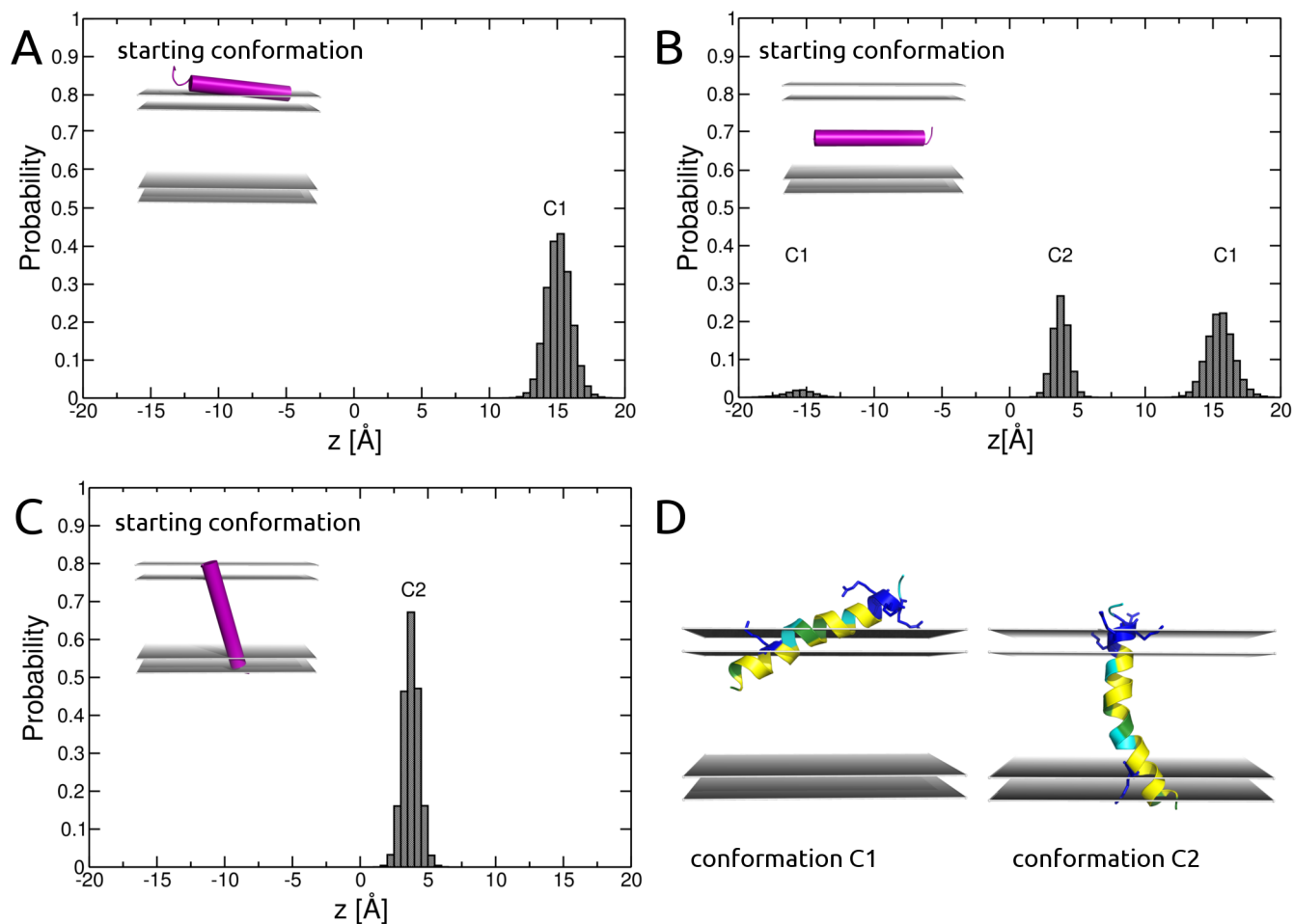


Figure 4.8.: Histograms (A-C) for the center of mass probability for Melittin simulations using our proposed membrane model. The corresponding starting conformation is depicted in each histogram. Panel (D) shows exemplary conformations for C1 and C2 peaks in the histograms [2].

The kink angle of the Melittin peptide, Figure 4.6, is defined as the angle between the vectors of the  $C_{\alpha}$  atoms Val<sub>5</sub> and Gly<sub>12</sub> as well as Leu<sub>16</sub> and Lys<sub>23</sub>. In simulations, excessively kinked helices can be observed, therefore two different regions for the kink angle were defined: excessively kinked helices with a kink angle  $\leq 60^{\circ}$  and normally kinked helices with kink angles  $> 120^{\circ}$ . Table 4.2 summarizes the kink angles for the end conformations of the simulations at 300K. Simulations with further temperatures are summarized in the diploma thesis of Carolin Seith [134] and show the same behaviour in general. Snapshots for the normally kinked and excessive kinked peptides are depicted in Figure 4.9. While in

Table 4.2.: Kink angle occurrence for the 300K Melittin simulations with three different starting conformations.

starting conformation	kink angle $\leq 60^\circ$	kink angle $> 120^\circ$
A - membrane interface	3	17
B - horizontal in the membrane centre	4	16
C - membrane spanning	1	19

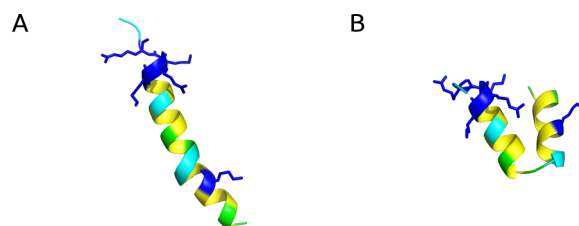


Figure 4.9.: Example for a normally kinked Melittin (A) and an excessively kinked conformation (B) taken from simulations with a starting conformation similar to explicit molecular dynamics results [2]

experiments no excessively kinked helices were observed, the measured kink angles vary between  $120^\circ$  in x-ray structures or in methanol [122, 135],  $140^\circ$  and  $160^\circ$  in the lipid bilayer [136] and  $160^\circ$  in water [135]. Other implicit membrane simulations also found a kink angle of  $48^\circ$  [111].

To understand why Melittin occurs excessively kinked in simulations but not in experiments, for three out of the 60 simulations the energies were analysed. Histograms for all energy contributions, Figure 4.10, show the energies of a simulation with an excessive kinked helix (red histograms) in comparison to energies of simulations with normally kinked helices (green and blue histograms) respectively.

The Lennard-Jones energies, Figure 4.10E, show significant differences larger than  $10[kcal/mol]$  between simulations of excessively kinked (red) and normally kinked helices (green and blue). This suggest kinked helices are energetically favoured.

Because proteins in water or membranes form a densely packed system, the Lennard-Jones minima of an atom are usually occupied by its nearest neighbours. Therefore large energy differences are not to be expected. In contrast to this expectation, large energy differences were observed in the Melittin simulations, wherefore the modelling of solute-solvent Lennard-Jones interactions in implicit solvent models seem to be insufficient by the current nonpolar term.

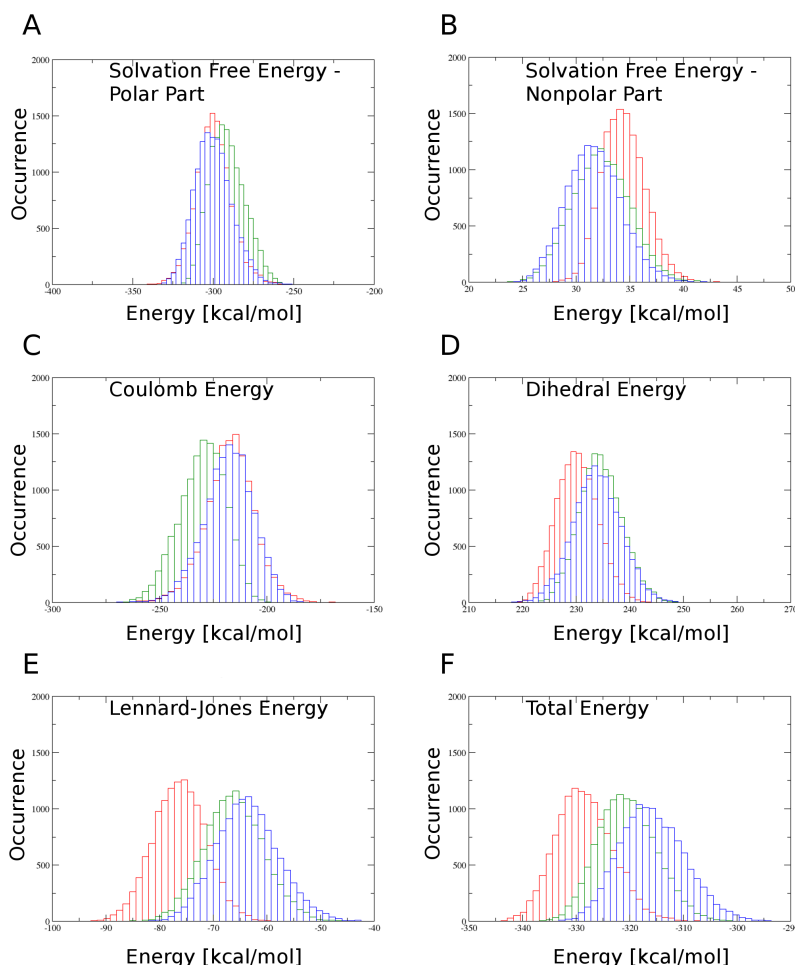


Figure 4.10.: Histograms of three Melittin simulations, one simulation with an excessively kinked protein in the end (red) and two with a normal kink angle (green and blue). Panel A-E show the different energy contributions, panel F the total energy. Conspicuously is the energy gap larger than  $10[kcal/mol]$  in the Lennard-Jones energy between the two different conformations.

To test this hypothesis, a simple Melittin model is discussed in the diploma thesis by Carolin Seith [134]. The results of this test in table 4.3 show that explicitly accounting for solute-solvent Lennard-Jones interactions energetically favours normally kinked Melittin conformations, while discarding these interactions favours excessively kinked conformations.

This problem of current implicit solvent models has to be investigated further. Solutions for this problem must be found, discussed and implemented.

Table 4.3.: Lennard-Jones energies for a simple Melittin model with and without accounting for solute-solvent Lennard-Jones interactions. Summarized are the energies of the normally kinked helices and the excessively kinked protein. The last column shows the energy difference  $\Delta E$  between the normal and the kinked structure [134].

	normally kinked helices	excessively kinked helices	$\Delta E$
without solvent-solute LJ interactions	-0.02 [kcal/mol]	-30.5 [kcal/mol]	-30.48 [kcal/mol]
with solvent-solute LJ interactions	-33.71 [kcal/mol]	-30.54 [kcal/mol]	+3.17 [kcal/mol]

## 4.5. M2 Protein

The SLIM model has two main parameters which can be used to adjust the model membrane to that in related studies or experiments. These are the membrane thickness  $h_m$  and the surface tension coefficient  $\gamma$ . To examine the influence of both, we simulated the M2 protein, another well-studied membrane protein [111, 137, 138]. The protein from *Influenza A* virus forms a tetrameric proton channel [139] activated by low pH [140]. For simulations with the SLIM model, a single transmembrane domain (see Figure 4.11), structurally characterized by Wang et al. (PDB code: 1MP6) [141], was used:

SER<sub>22</sub>- SER<sub>23</sub>- ASP<sub>24</sub>- PRO<sub>25</sub>- LEU<sub>26</sub>- VAL<sub>27</sub>- VAL<sub>28</sub>- ALA<sub>29</sub>- ALA<sub>30</sub>- SER<sub>31</sub>- ILE<sub>32</sub>- ILE<sub>33</sub>-  
 GLY<sub>34</sub>- ILE<sub>35</sub>- LEU<sub>36</sub>- HIS<sub>37</sub>- LEU<sub>38</sub>- ILE<sub>39</sub>- LEU<sub>40</sub>- TRP<sub>41</sub>- ILE<sub>42</sub>- LEU<sub>43</sub>- ASP<sub>44</sub>- ARG<sub>45</sub>-  
 LEU<sub>46</sub>.

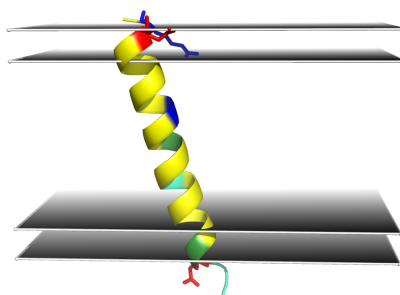


Figure 4.11.: The transmembrane domain of the M2 protein consists mainly of *hydrophobic* amino acids (yellow) flanked by *positive* (blue) or *negative* (red) charged amino acids as well as *polar* (cyan) residues on either end of the hydrophobic part.

Membrane spanning proteins show normally an amphiphilic character. Residues in the membrane are hydrophobic, while residues in the headgroup or water region are polar or charged. Energetically it is

unfavourable when a hydrophobic surface reaches into a hydrophilic environment. If a protein is too long to match the membrane, the proteins can kink or tilt to reach more favourable conformations. This effect is also known as hydrophobic mismatch [142]. For instance, in NMR experiments it is possible to investigate tilt angles of membrane proteins, as done by Kovacs et al. for the M2 protein [143], wherefore this property was used as a test parameter for the influence of our model parameters.

Since the surface tension value  $\gamma$  is an empirical parameter, 80 simulations with four different values between  $\gamma = 20\text{cal}/(\text{mol}\text{\AA}^2)$  and  $\gamma = 50\text{cal}/(\text{mol}\text{\AA}^2)$  were performed with a membrane thickness of  $h_m = 30\text{\AA}$  and a simulation temperature of 300K. For the analysis, the first one million steps out of 20 million MC steps were discarded.

The starting conformation (see Figure 4.12A) was horizontal in the membrane center. In addition to the expected membrane spanning conformation, some kinked proteins similar to the excessively kinked Melittin peptides (see Section 4.4), could be found.

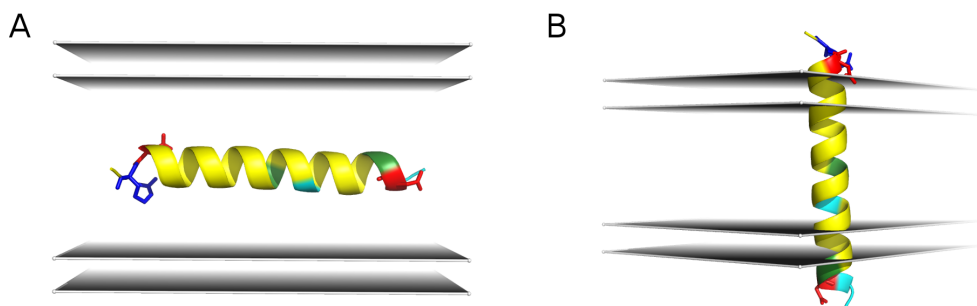


Figure 4.12.: Starting conformation for M2 protein simulations with  $h_m = 30\text{\AA}$  horizontal in the membrane center and for simulations with  $h_m = 25\text{\AA}$  parallel to the membrane normal.

For the M2 simulations, the kink angle was defined as depicted in Figure 4.13. Due to a missing helix breaker in the middle of the helix, like proline in Melittin, and a varied breaking residue, the kinks occur at various positions. The choice of the vector spanning  $C_\alpha$  atoms of residues  $Leu_{26}$  and  $Ile_{33}$  as well as  $Ile_{33}$  and  $Leu_{40}$  is made by visual inspection of kinked proteins.

The analysis for the 80 simulations yields an averaged kink angle for an unkinked M2 protein of  $171^\circ$ . Kinked helices can be identified by outliers in histograms of the minimum kink, Figure 4.14, or in the standard deviation, Figure 4.15. Both figures show histograms of four different surface tension values

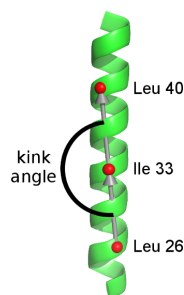


Figure 4.13.: The kink angle for the M2 protein is defined as the angle between the vectors connecting the  $C_\alpha$  atoms of residues *Leu*<sub>26</sub> and *Ile*<sub>33</sub> as well as *Ile*<sub>33</sub> and *Leu*<sub>40</sub> [2].

$\gamma$  ranging from 20 to 50  $\text{cal}/(\text{mol}\text{\AA}^2)$ . Each panel shows the data for 20 simulations averaged over 19 million Monte Carlo steps. Simulations in which the protein does not kink in the first steps show a higher minimum kink angle than proteins kinking from the very beginning.

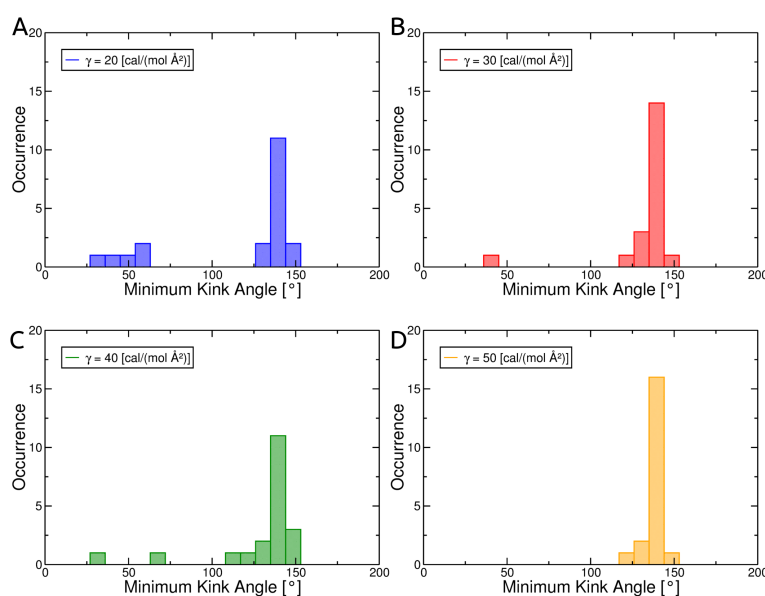


Figure 4.14.: Occurrence of the minimum kink angle for simulations with  $h_m = 30\text{\AA}$  and  $\gamma = 20\text{cal}/(\text{mol}\text{\AA}^2)$  (Panel A),  $\gamma = 30\text{cal}/(\text{mol}\text{\AA}^2)$  (Panel B),  $\gamma = 40\text{cal}/(\text{mol}\text{\AA}^2)$  (Panel C),  $\gamma = 50\text{cal}/(\text{mol}\text{\AA}^2)$  (Panel D) is shown in this figure. The starting structure was parallel to the membrane interface in the membrane center. Kinked helices can be distinguished by the outliers in panels A-C.

Analysing the data for the different surface tension values  $\gamma$ , it can be observed that the minimum, maximum and average kink angles for unkinked helices are in the same range (see table 4.4).

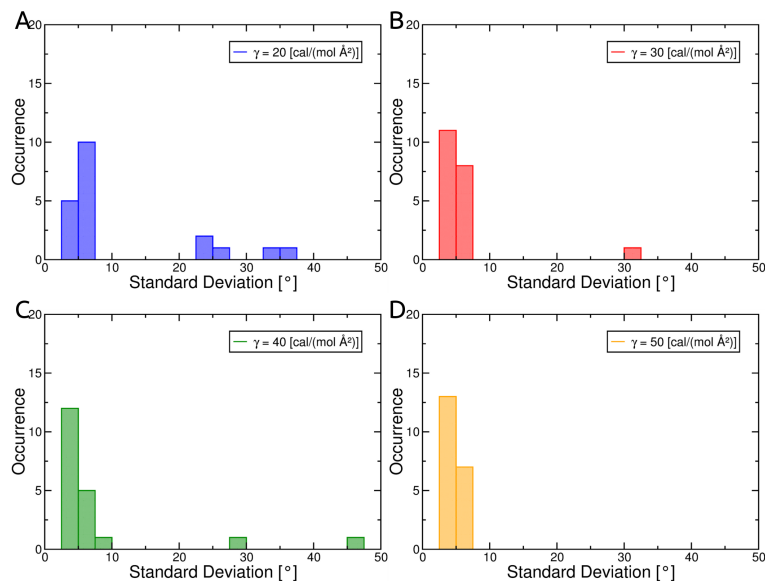


Figure 4.15.: The standard deviation of the kink angle is depicted here. Kinked helices in simulations with  $h_m = 30\text{\AA}$  and  $\gamma = 20\text{cal}/(\text{mol}\text{\AA}^2)$  (Panel A),  $\gamma = 30\text{cal}/(\text{mol}\text{\AA}^2)$  (Panel B),  $\gamma = 40\text{cal}/(\text{mol}\text{\AA}^2)$  (Panel C) can be identified by high standard deviations. Simulations with  $\gamma = 50\text{cal}/(\text{mol}\text{\AA}^2)$  (Panel D) show no kinked helices.

In the following, the data of simulations with kinked helices having a minimum kink angle smaller than  $100^\circ$  are discarded, since a tilt angle analysis is only possible for more or less unkinked helices. Again the assumption that the reason for the kinks is a general problem of implicit models (see also Section 4.4) can be made and should be investigated in the future.

Beside kink angle analysis,  $\Phi - \Psi$  plots are another possibility to check the helix stability. The backbone dihedrals  $\Phi$  and  $\Psi$  in proteins with a helical structure usually have repeating constant values (see also Section 2.1.2). Calculating these dihedral angles as a function of the residue number for the remaining 72 unkinked simulations with  $h_m = 30\text{\AA}$  results in the graphs of Figure 4.16. The average angles and their standard deviation are shown. The values agree with those of the native M2 protein conformation. Only the residues near the headgroup regions show larger fluctuations.

For the comparison of computed tilt angles with experimental data, the tilt angle is defined as the angle between the membrane normal and the principal axis of the backbone heavy atoms with the lowest moment of inertia. The latter corresponds to the axis of the  $\alpha$ -helix for not too strongly kinked helices [2]. For the 72 simulations, the first one million steps are also discarded, thus the tilt angle is averaged

Table 4.4.: The average values for 20 replica for each surface coefficients  $\gamma$  show that the kink angles are all in the same range. The starting structure for all M2 protein simulations was horizontal in the membrane center in a  $h_m = 30\text{\AA}$  membrane with surface tension coefficients  $\gamma = 20 - 50\text{cal}/(\text{mol}\text{\AA}^2)$ . Kinked simulations are discarded.

$\gamma[\text{cal}/(\text{mol}\text{\AA}^2)]$	minimum [°]	maximum [°]	average [°]	standard deviation [°]
20	139.6	179.9	171.1	5.2
30	137.6	179.9	171.4	5.0
40	137.5	179.9	171.4	5.1
50	138.4	179.9	171.6	5.0

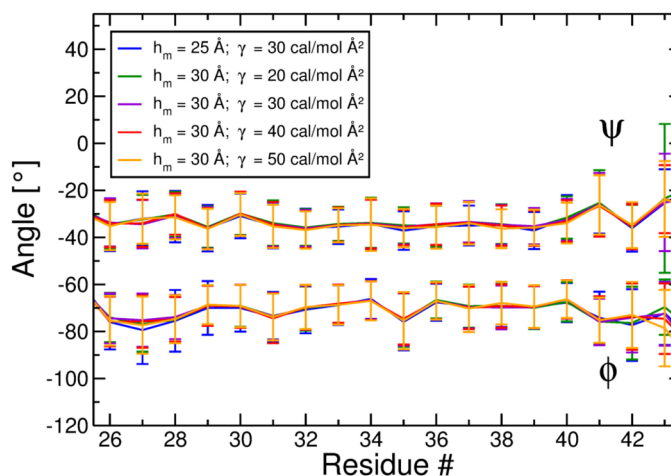


Figure 4.16.: Averaged  $\phi$  and  $\psi$  backbone dihedral angles with standard deviations for the transmembrane domain (Leu26 to Leu43) of the M2 protein as a function of the membrane thickness  $h_m$  and the surface tension  $\gamma$ . Data basis for  $h_m = 30\text{\AA}$  are the 72 simulations with un-kinked helices and for  $h_m = 25\text{\AA}$  the 20 simulations with  $\gamma = 30\text{cal}/(\text{mol}\text{\AA}^2)$ , where no kinked helices are present in the simulations [2].

over the remaining 19 million MC steps. Figure 4.17 shows the tilt angle dependence on different surface tension values  $\gamma$  for the simulations with  $h_m = 30\text{\AA}$  (Panel A red squares and Panel B). With increasing  $\gamma$ , the tilt angle increases from  $15.8^\circ$  up to  $30.0^\circ$ . The large variation of the tilt angles is explained by the shifted balance between nonpolar and electrostatic solvation effects due to the increasing surface tension  $\gamma$ . This forces the polar termini regions of the M2 transmembrane domain deeper into the headgroup regions as depicted in 4.17B. The protein accommodates this tension through a higher tilt angle [2].

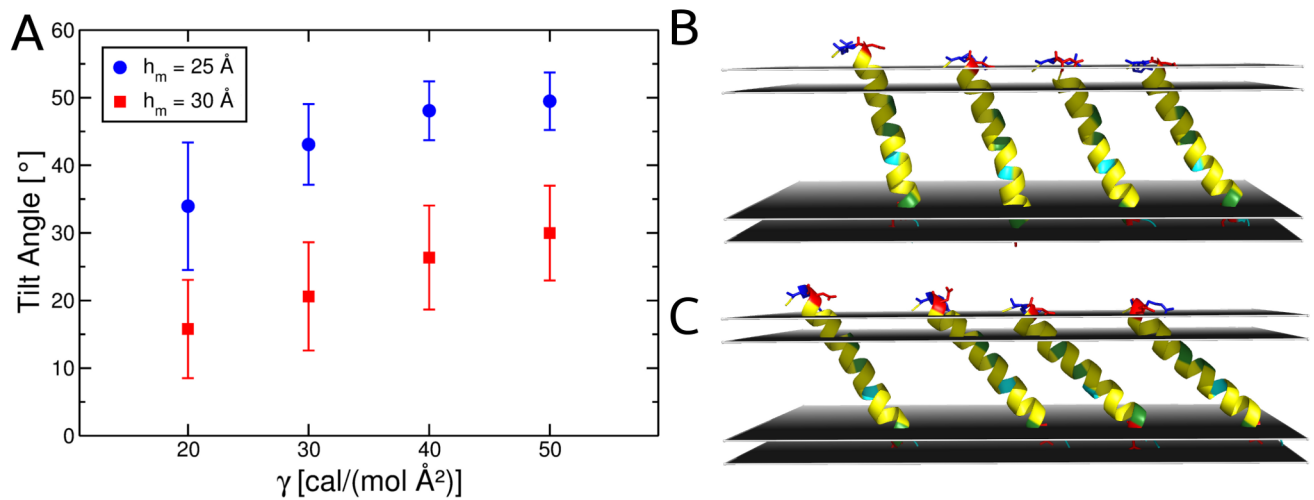


Figure 4.17.: Tilt angle dependence of the transmembrane domain of the M2 protein on the membrane thickness  $h_m$  and the surface tension parameter  $\gamma$  in the SLIM model (A). Exemplary conformations (from left to right  $\gamma = 20, 30, 40, 50 \text{ cal}/(\text{mol}\text{\AA}^2)$ ) with the average tilt angle in a membrane with  $h_m = 30\text{\AA}$  thickness (B) and  $h_m = 25\text{\AA}$  (C) [2]

These findings are in agreement with those of Im et al. [111], who also observed an increasing tilt angle for larger  $\gamma$ , but the values are much smaller than the experimental ones by Kovacs et al. [143] (see also table 4.5). Regarding the concept of hydrophobic mismatch, a thinner membrane should lead to higher tilt angles. To test this, simulations with  $h_m = 25\text{\AA}$  were performed. The starting conformation was parallel to the membrane normal in the membrane center (see Figure 4.12B). No kinked helices could be observed in the simulations. The tilt angle increases from  $34^\circ$  up to  $49.5^\circ$  and is also shown in Figure 4.17 and table 4.5. Figure 4.17A shows the averaged tilt angles for simulations in a membrane with  $h_m = 25\text{\AA}$  and surface tension values of  $\gamma = 20$  up to  $50 \text{ cal}/(\text{mol}\text{\AA}^2)$  (blue dots). Panel C shows that the proteins have higher tilt angles in thinner membranes, as expected before.

Analysing the  $\Phi - \Psi$  plot for simulations with  $h_m = 25\text{\AA}$  leads to the same conclusions as for the thicker membrane. The helix is stable and the values are in agreement with those of the native conformation. A graph for 20 simulations with  $h_m = 25\text{\AA}$  and  $\gamma = 30 \text{ cal}/(\text{mol}\text{\AA}^2)$  is also displayed in Figure 4.16.

The tilt angles in table 4.5 display a correct behaviour of the SLIM model with respect to the concept of hydrophobic mismatch and show good agreement with the angles calculated by Im et al. [111] using a different implicit membrane model.

Table 4.5.: Tilt angles of the M2 protein. Summarized are values derived from NMR experiments by Kovacs et al. [143], values from implicit membrane simulations by Im et al. [111] and tilt angles calculated with the SLIM model. For the implicit models, the surface tension values  $\gamma$  and  $\tilde{\gamma}$  as well as the membrane thickness  $h_m$  is specified.

Membrane	NMR [143]	SLIM				Im [111] 40[cal/molÅ <sup>2</sup> ]
		20[cal/molÅ <sup>2</sup> ]	30[cal/molÅ <sup>2</sup> ]	40[cal/molÅ <sup>2</sup> ]	50[cal/molÅ <sup>2</sup> ]	
$h_m = 25\text{Å}$	–	34.0° ± 9.4°	43.1° ± 6.0°	48.1° ± 4.4°	49.5° ± 4.3°	43.1° ± 3.3°
$h_m = 29\text{Å}$	–	–	–	–	–	28.5° ± 5.1°
$h_m = 30\text{Å}$	–	15.8° ± 7.3°	20.6° ± 8.0°	26.4° ± 7.7°	30.0° ± 7.0°	–
DMPC	37.3°	–	–	–	–	–
DOPC	33.3°	–	–	–	–	–

However, a discrepancy between experimental and theoretical values is indisputable. The Melittin Section 4.4 revealed that the SLIM membrane with  $h_m = 30\text{Å}$  is rather thin compared to hydrophobic core measurements for DOPC by Nagle et al. [133], but only decreasing the membrane thickness leads to a tilt angle range in the experimental dimension. Im et al. proposed another possibility to explain these discrepancies: In NMR experiments tetramers of the M2 protein are analysed, in the simulations only monomers. To investigate the transferability of this argument on the SLIM model, Glycophorin A, a simpler but also well studied membrane protein was simulated [2]. The investigation of M2 oligomers should be a future project.

## 4.6. Glycophorin A

Glycophorin A (GpA), the primary sialoglycoprotein of human erythrocyte membranes forms a dimer in the membrane [137, 144]. The protein is comprised of 40 residues and structurally characterized both by solution NMR solubilized in aqueous detergent micelles by MacKenzie et al. [145] and by solid-state NMR in lipid bilayers by Smith et al. [146, 147]. For the simulations the transmembrane residues of the PDB 1afo was used [145] (Figure 4.18):

**PRO**<sub>71</sub>- **GLU**<sub>72</sub>- **ILE**<sub>73</sub>- **THR**<sub>74</sub>- **LEU**<sub>75</sub>- **ILE**<sub>76</sub>- **ILE**<sub>77</sub>- **PHE**<sub>78</sub>- **GLY**<sub>79</sub>- **VAL**<sub>80</sub>- **MET**<sub>81</sub>- **ALA**<sub>82</sub>- **GLY**<sub>83</sub>- **VAL**<sub>84</sub>- **ILE**<sub>85</sub>- **GLY**<sub>86</sub>- **THR**<sub>87</sub>- **ILE**<sub>88</sub>- **LEU**<sub>89</sub>- **LEU**<sub>90</sub>- **ILE**<sub>91</sub>- **SER**<sub>92</sub>- **TYR**<sub>93</sub>- **LEU**<sub>94</sub>- **ILE**<sub>95</sub>.

To investigate if the tilt angles of monomers and dimers behave differently in the same membrane,

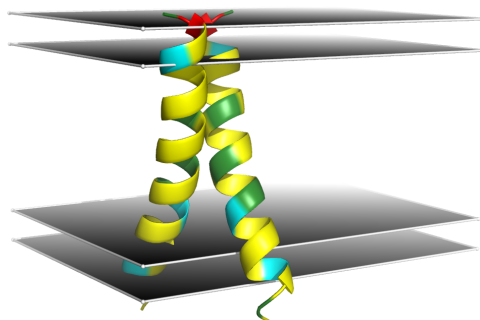


Figure 4.18.: The transmembrane domain of Glycophorin A mainly consists of *hydrophobic* amino acids (yellow) and *special* cases (green) flanked by *negative* charged (red) amino acids as well as *polar* residues (cyan) on either end of the hydrophobic part. For monomer and dimer simulations a orientation parallel to the membrane normal was used as starting conformation.

simulations of both monomers and dimers were performed for the transmembrane domain of GpA. The starting conformation for all simulations was parallel to the membrane normal (see also Figure 4.18). For surface tension values between  $\gamma = 20$  and  $\gamma = 50[\text{cal}/\text{mol}\text{\AA}^2]$  and a membrane thickness of  $h_m = 30\text{\AA}$ , 20 independent simulations with 10 million MC steps were performed. In analogy to Section 4.5, the first one million steps were discarded for the tilt angle analysis. The average tilt angles are depicted in Figure 4.19. The dimer simulations show a different behaviour. The angles range from  $21.43^\circ \pm 5.62^\circ$  to  $24.07^\circ \pm 8.55^\circ$  (see table 4.6) and therefore vary only  $2.64^\circ$  in contrast to the  $16.15^\circ$  of the monomer.

For the monomer, the tilt angles increase with higher surface tension values and range from  $14.08^\circ \pm 6.95^\circ$  ( $\gamma = 20[\text{cal}/\text{mol}\text{\AA}^2]$ ) to  $30.23^\circ \pm 8.82^\circ$  ( $\gamma = 50[\text{cal}/\text{mol}\text{\AA}^2]$ ) (see also table 4.6).

Table 4.6.: Tilt angles of Glycophorin A monomers and dimers, calculated with the SLIM model.

	Tilt angles calculated with the SLIM model			
	$\gamma = 20[\text{cal}/\text{mol}\text{\AA}^2]$	$\gamma = 30[\text{cal}/\text{mol}\text{\AA}^2]$	$\gamma = 40[\text{cal}/\text{mol}\text{\AA}^2]$	$\gamma = 50[\text{cal}/\text{mol}\text{\AA}^2]$
monomer	$14.08^\circ \pm 6.95^\circ$	$17.55^\circ \pm 8.29^\circ$	$23.87^\circ \pm 9.03^\circ$	$30.23^\circ \pm 8.82^\circ$
dimer	$21.43^\circ \pm 5.62^\circ$	$22.15^\circ \pm 6.07^\circ$	$22.93^\circ \pm 6.95^\circ$	$24.07^\circ \pm 8.55^\circ$

The average tilt angles are more sensitive to different surface tension values for the monomers than the

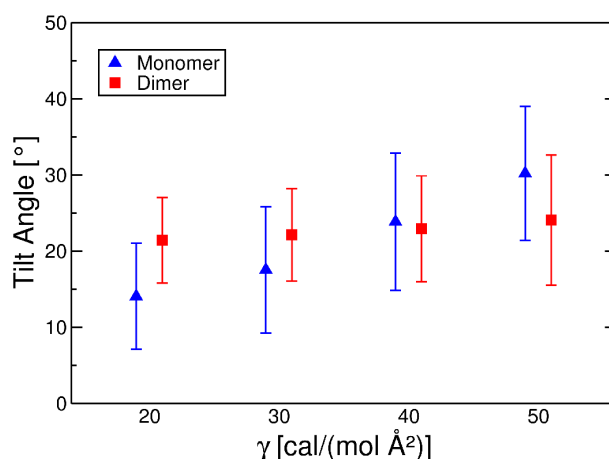


Figure 4.19.: Averaged tilt angles and standard deviations for a monomer and the dimer of the transmembrane domain of Glycophorin A for different surface tension coefficients  $\gamma$  [2].

dimers. These findings agree with those of Im et al. [111]. An explicit membrane study by Petrache et al. [148] found much larger tilt angles for dimeric transmembrane helices than for monomeric ones [2]. This suggests that surface tension values  $> 30[\text{cal}/\text{mol}\text{\AA}^2]$  may lead to a non realistic behaviour of GpA in the SLIM model. Interestingly Petrache et al. observed that the average explicit membrane thickness varies in monomer and dimer simulations. In dimer simulations, the thickness is up to  $2.4\text{\AA}$  smaller [148]. The SLIM membrane is not influenced by the inserted protein, therefore this effect should be modeled by a careful parameter selection in future simulations.

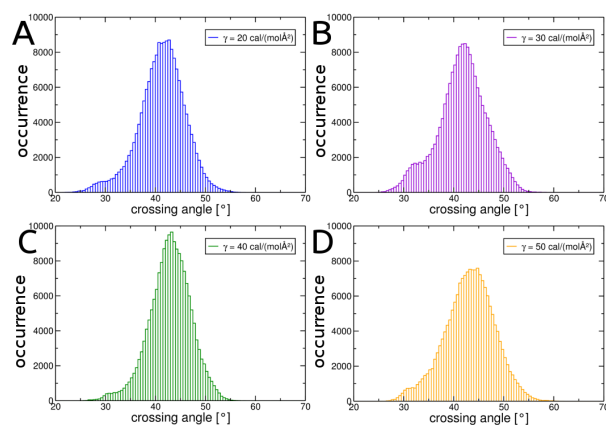


Figure 4.20.: Crossing angle of the Glycophorin A dimer. (A-D) Histograms of the crossing angles of simulations with different surface tension values  $\gamma$ . The crossing angle is defined as the angle between the principal axes of the backbone heavy atoms of the transmembrane domain (Leu26-Leu43) of the two chains.

For a dimer simulation, the orientation of the two proteins relative to each other is also very important. The crossing angle, defined by the angle between the principal axes of the backbone heavy atoms of the transmembrane domain (Leu26-Leu43) of the two chains, is with an average of  $41.2^\circ - 43.1^\circ$  (for different surface tension values) in good agreement to the experimental value of  $40^\circ$  measured by MacKenzie et al. [145]. Histograms for crossing angles are depicted in Figure 4.20.

## 4.7. Summary

Implicit membrane offer a computationally efficient method to study certain properties and interactions of membrane proteins. The new implicit membrane model SLIM (SIMONA layered implicit membrane) combines advantages of previously published models. Comparisons to Poisson-Boltzmann calculations show that SLIM outperforms other implicit membrane models regarding the accurate description of electrostatic interactions inside the membrane. The results show good quantitative and qualitative agreement of self-energy terms for single ions and a protein with a single charge as well for the interaction terms of two proteins inside the membrane. Simulations of three well-studied membrane proteins showed that known properties of these proteins are reproduced by the SLIM model.

Future investigations include the improvement of the efficiency of the simulations, using different Monte Carlo moves and a parallelized version of the code. The low computational cost of the implicit model enables the investigation of processes like protein assembly inside the membrane, which are out of reach for explicit membrane simulations. Different studies regarding the interactions between different membrane proteins, protein folding in membranes and dimerization of proteins are already in progress.

## 5. Black Lipid Bilayer Experiments

Artificial bilayer membrane (*in vitro*) experiments can help to shed light on the complex interactions between molecules and membranes. The earliest model system was the black lipid bilayer system (BLB), where a membrane is formed between two compartments filled with salt solution [149]. The method is named “black” lipid bilayer due to the fact that a membrane appears “black” when viewed by reflected light [150, 151]. In addition to the BLB, there are many other systems like detergent micelles, bicells, nanodiscs, vesicles, tethered lipid bilayer membranes and supported lipid bilayers [152–157] which are used in experiments nowadays.

In this chapter the experimental setup used for BLB experiments is discussed in Section 5.1. A general introduction to antimicrobial peptides and gold nanoparticles can be found at the beginning of Section 5.2 and 5.3. Furthermore, experimental results on membrane conductivity changes induced by Gramicidin A and S, as well as different sized gold nanoparticles are discussed.

### 5.1. Experimental Setup

BLB experiments [158] were performed in the lab of Prof. Dr. Dr. h.c. Dr. h.c. Roland Benz at the Julius Maximilian University of Würzburg. Except Gramicidin A all investigated compounds were provided by our co-workers, the Ulrich group at Karlsruhe Institute of Technology and the Simon group at the University of Aachen.

The schematic setting of the experiment is shown in Figure 5.1: The crucial component is the bilayer in the septum of an aqueous filled Teflon chamber. Using two electrodes, it is possible to apply an external potential. A signal amplifier and oscilloscope or strip chart recorder enable the measurement

of the membrane conductivity.

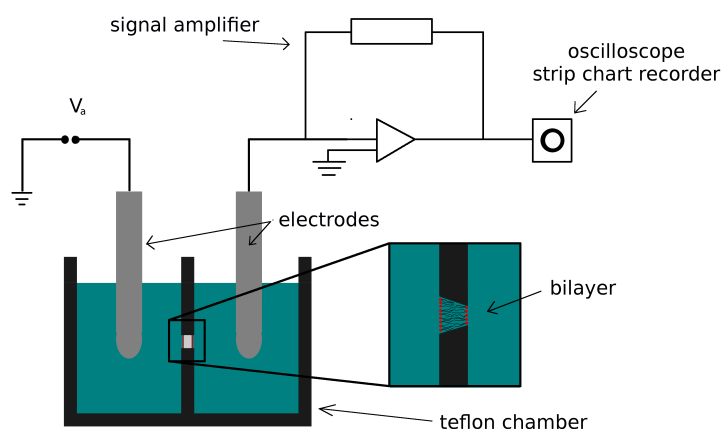


Figure 5.1.: Schematic setting of the bilayer experiments. The bilayer forms over a small hole in the septum of an aqueous filled Teflon chamber. Two electrodes enable to apply an external potential to the membrane. The measurement can be performed with an oscilloscope or strip chart recorder.

Figure 5.2 shows the measuring and membrane painting equipment. The Teflon chamber and the silver/silver-chloride electrodes (fig. 5.2(B)) are mounted in a Faraday cage on a vibration free table to shield the measurement from external perturbations (fig. 5.2(A)). On top of this cage is a Burr Brown operational amplifier, which allows the measurement of the membrane current by a strip chart recorder (fig. 5.2(E)).

The Teflon chamber has two compartments (named as *cis*-side and *trans*-side) each filled with 5ml salt solution and connected by a small hole with  $0.5\text{mm}^2$  surface area.

To form the membrane in the hole, two steps are necessary:

1. Pre-preparation with a 2% solution of the lipid
2. Painting of the membrane with a small Teflon loop and a 1% solution of the lipid

For the pre-preparation, a 2% solution of the lipid in chloroform was used. The lipid was applied to the hole in the septum before filling the compartments with the salt solution. After insertion of the Teflon chamber in the Faraday cage and the arrangement of the electrodes, the membrane was painted

with a 1% solution of the lipid and the aid of a small Teflon loop (fig. 5.2(C)+(D)). For production of this 1% solution, 50 $\mu$ l of a 4% solution was dried in a rotary evaporator, 200 $\mu$ l of the desired solvent and 20 $\mu$ l n-butanol were added.

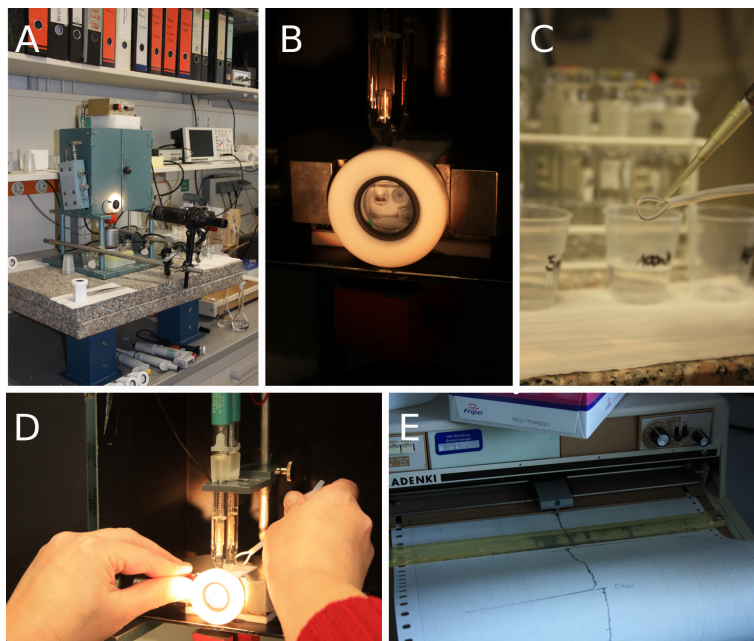


Figure 5.2.: Experimental setup for the black lipid bilayer experiments: (A) The measuring equipment is placed on a vibration free table. A Faraday cage contains the Teflon chamber with salt solution and two electrodes (B). A small Teflon loop (C) is used to paint the membrane (D). Current can be measured with the strip chart recorder (E).

Besides the lipid, the desired solvent for the 1% solution of the lipid used for the membrane painting effects membrane properties like thickness and capacity as well [159, 160]. Therefore different lipids and mixtures were used for the experiments. These contained diphytanoyl-phosphatidylcholine (DiphPC) (fig.5.3(A)) in n-decane or a mixture of DiphPC and diphytanoyl-phosphatidylglycerol (DiphPG) (fig.5.3(B)) in n-decan ( $C_{10}H_{22}$ ) as well as in hexadecan ( $C_{16}H_{34}$ ). Hexadecan is in a solid state below room temperature, therefore the temperature during the experiment is very crucial.

To apply a potential to the membrane, silver/silver-chloride electrodes were inserted into the aqueous salt solutions on both sides of the membrane (see Figure 5.2B). Asymmetries of the electrodes, which can occur due to careless storage or handling, were checked regularly.

The potential has to be changed several times during a single experiment and always refers to the

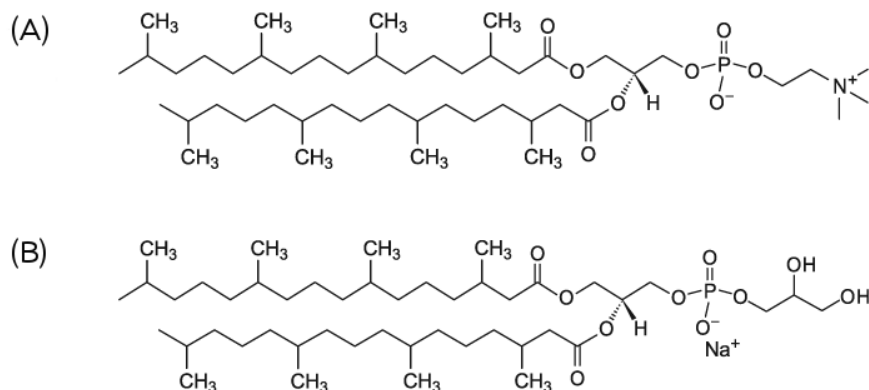


Figure 5.3.: Chemical structure of the lipids used in BLB experiments. (A) diphytanoyl-phosphatidylcholine (DiphPC) and (B) diphytanoyl-phosphatidylglycerol (DiphPG).

*cis*-side of the chamber; at the *trans*-site inverse polarity was applied. The membrane current was recorded by a strip chart recorder, using a current-to-voltage converter constructed with a Burr Brown operational amplifier.

Control experiments without addition of the solute were performed for all the measurements to avoid misinterpretation of data due to contaminations of the Teflon chamber with solutes from previous experiments. All experiments were repeated several times, further informations are given in each section.

### 5.1.1. Conductivity Measurements

After preparation of the Teflon chamber and painting of the membrane, control experiments without addition of the solute were performed. A membrane potential  $V_a$  was applied and the membrane current  $I$  was recorded up to 30 minutes. Then the voltage could be increased or the polarity reversed. The membrane conductivity can be calculated via equation 5.1.

$$G[S] = \frac{I[A]}{V_a[V]} \quad (5.1)$$

The unit for the conductivity  $G$  is *Siemens* [S] and defined as  $\frac{A}{V}$ .

For conductivity measurements itself, the solute was usually added to the *cis*-site of the chamber. After the solute was added, currents for different potentials were measured in serial. The experiment was

stopped when the bilayer dissolved.

### 5.1.2. Selectivity Measurements

The selectivity measurements began with the same set up as for conductivity measurements. After a control experiment a conductivity measurement with settings taken from a previous measurement was performed until an increase of the conductivity was observed. After that, the selectivity measurement was started.

The measuring instrument was changed to a voltmeter instead of the strip chart recorder to measure the membrane potential  $V_m$ . A salt concentration gradient was established in the Teflon chamber by adding a higher concentrated salt solution to the *cis*-side. To avoid hydrostatic pressure differences, the same amount of the stock solution was added to the *trans*-side of the membrane at the same time. Based on the concentration gradient, the ions diffuse through the membrane and form a potential difference until a new equilibrium is reached. With the measurement of the potential and the known concentration gradient, the analysis using the Goldman-Hodgkin-Katz equation was performed [161].

$$V_m = \frac{R \cdot T}{F} \cdot \ln \frac{P_c \cdot c_2 + P_a \cdot c_1}{P_c \cdot c_1 + P_a \cdot c_2} \quad (5.2)$$

R is the gas constant, T the absolute temperature and F the Faraday constant. With the membrane potential  $V_m$  and the salt concentrations  $c_1$  on the *cis*-side and  $c_2$  on the *trans*-side, the cation/anion permeability ratio between  $P_c$  and  $P_a$  can be determined.

$$\frac{P_a}{P_c} = \frac{c_1 \cdot e^{0.025 \cdot V_m} - c_2}{c_1 - c_2 \cdot e^{0.025 \cdot V_m}} \quad (5.3)$$

## 5.2. Antimicrobial Peptides

### 5.2.1. Introduction

In the 1940s and 50s antibiotics such as penicilin were dealt as miracle drugs, which were able to kill the bacteria that caused many of human-kinds worst infections [162]. Today the emergence of resistances

necessitate alternative drugs like peptide antibiotics [36]. Antimicrobial peptides, also called cationic host defence peptides, can show antibacterial, anti fungal, antiviral, anti protozoan and antiseptic properties and are found in all living cells [37].

Antimicrobial peptides are between 11 and 50 amino acids long and have a net positive charge of +2 to +7 proton charges [36]. In addition to at least two positively charged residues like arginine, lysine or histidine, they are composed of a large proportion of hydrophobic residues ( $\geq 30\%$ ) [37, 163]. Structurally, there are four different groups:  $\beta$ -sheet peptides stabilized by two to four disulfide bridges,  $\alpha$ -helical peptides, extended peptides and loop peptides with one single disulfide bond [164]. The  $\alpha$ -helical peptides are unstructured in solution and only fold into amphiphatic  $\alpha$ -helices upon contact with membranes [37].

Their activity is related to the cationic and amphiphilic nature of the peptides. They contact the anionic surface of the cytoplasmic membrane and insert themselves in a way that they initially straddle the interface of the hydrophilic head groups and the fatty acyl chains of the membrane phospholipids. After insertion they act by disrupting the physical integrity of the bilayer via membrane thinning, transient poration and/or disruption of the barrier function. Moreover, they can translocate across the membrane and act on internal targets [163]. Several models, like the barrel-stave, toroidal worm hole or carpet model are summarized in different reviews [165, 166].

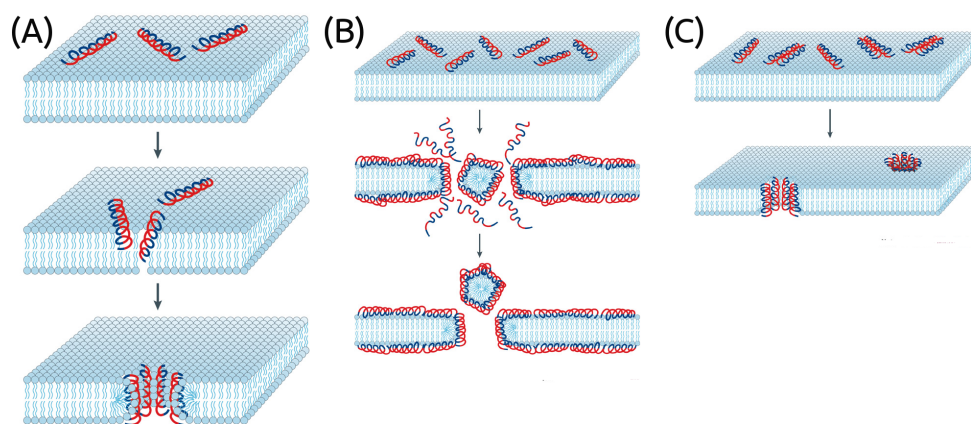


Figure 5.4.: Different models for membrane permeation of antimicrobial peptides (A) toroidal model (B) carpet model (C) barrel-stave model [166]. Copyright 2005 Nature Publishing Group.

## Gramicidin

Gramicidin, a polypeptide antibiotic, kills Gram-positive bacteria and is produced by the soil bacteria *Bacillus brevis* [167]. Gramicidin forms dimeric channels specifically for the transport of monovalent cations across membranes. It adopts several different conformations, most notably double helical (pore) and helical dimer (channels) forms, which have very different structural and functional characteristics. It has been the subject of a wide number of biophysical, biochemical and physiological investigations, and is probably one of the best studied and understood ion channels [168]. Gramicidin, more precisely Gramicidin D, is a mixture of 80% Gramicidin A (GramA), 6% Gramicidin B and 14 % Gramicidin C [169] linear pentadecapeptides. In contrast, Gramicidin S (GramS), discovered in 1942, is a cyclic peptide [170] which has activity against Gram-positive and Gram-negative bacteria [171, 172].

### 5.2.2. Experimental Results and Discussion

Within the scope of this thesis and the diploma thesis of Yvonne Klapper [173], a collaboration with both the group of Prof. Dr. Anne S. Ulrich from the Karlsruhe Institute of Technology in Karlsruhe and the group of Prof. Dr. Dr. h.c. Dr. h.c. Roland Benz at the Julius Maximilian University in Würzburg was arranged. Beside the bilayer expertise in the Benz group, the Ulrich BioNMR group focuses on peptides interacting with biological membranes. Peptides of the Ulrich group were investigated in the Benz lab. Complement computational studies with the SLIM model (section 4) [2] are still under investigation. Different studies of GramS in the literature show opposed results regarding the membrane activity: Heitz et al. [174] and Wu et al. [175] reported channel-like activity of GramS. In contrast Ashrafuzzaman et al. [176] suggest GramS induces defects in the phospholipid bilayer instead of forming pores.

Due to several reasons such as a known and simple structure or the availability in large quantities, Gramicidin A (GramA) [177, 178] is a widely used cation selective channel [179]. Hladky et al. performed lipid bilayer experiments to investigate channels induced by Gramicidin A and showed pore formation and increased conductivity already in the 1972 [180].

On the one hand, bilayer experiments with Gramicidin were performed to validate our experimental set up, and on the other hand to provide data for later simulations with the newly developed implicit

membrane model SLIM (Chapter 4).

### Gramicidin S

The cyclic peptide Gramicidin S (GramS) was investigated in five different conductivity measurements. The Teflon chamber was filled with 1M KCl in all experiments and the lipid mixture was DihPC/DiphPG(80:20)(in n-decan or hexadecan). For one experiment with a DiphPC (in n-decan) membrane 150mM KCl was used, due to parallel test experiments with the gold nanoparticles which are not stable in 1M KCl solution. The peptide was provided by the Ulrich group at the Karlsruhe Institute of Technology.

### Reference Measurement

At the beginning of all experiments, a reference measurement was performed. Figure 5.5 shows a representative snapshot out of a strip chart record of a reference measurement for GramS experiments.

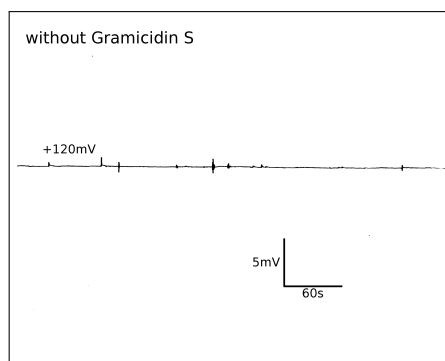


Figure 5.5.: Reference measurement for a bilayer conductivity experiment with GramS. A Dih-phPC/DiphPG lipid mixture in hexadecan was used for the membrane. The applied potential was  $V_a = +120mV$ .

### Conductivity Measurement

The conductivity measurements show the following results: While one experiment with a DiphPC (n-decan) membrane showed no increase of the conductivity with the peptide on the *cis*-side with an applied potential of maximum  $|V_a| = 100mV$  and an end concentration of 1mM, three experiments

with membranes composed out of a lipid mixture DiphPC/DiphPG(80:20) in n-decan or hexadecan showed an increase of the conductivity. The peptide concentration was higher - 1mM on both sides of the membrane and the applied potential was between  $|V_a| = 120mV$  and  $|V_a| = 180mV$ . In a fifth measurement the membrane converted to a multi-layer during the experiment (even very high applied voltages could not destroy the membrane), therefore no effect could be observed. In further experiments the membranes were observed during the measurement to directly stop experiments when a multi-layer was formed. A part of a strip chart record for the measurement with an increased conductivity is shown in Figure 5.6.

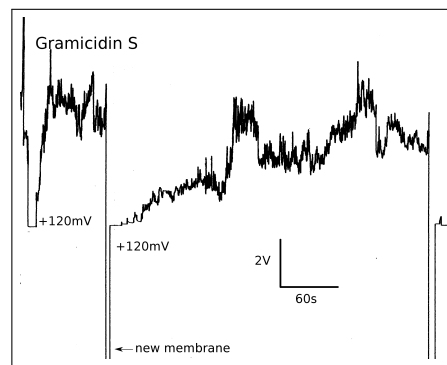


Figure 5.6.: Conductivity measurement for a membrane with DiphPC/DiphPG lipids in hexadecan and the peptide GramS. The increased conductivity was observed with an applied potential of  $V_a = +120mV$ .

Almost the same experimental set up like Wu et al. [175] was used and their results were confirmed. Heitz et al. [174] and Wu et al. [175] reported channel-like activity of GramS. In contrast Ashrafuzza-man et al. [176] suggested GramS induces defects in the phospholipid bilayer instead of forming pores. However the membrane activity of GramS is indisputable in all experiments and could be confirmed with these bilayer experiments.

### Gramicidin A

In bilayer experiments for the peptide Gramicidin A (Gram A; source: company Sigma-Aldrich) an increase of the conductivity could be observed in five out of six experiments. In all experiments a 1M KCl solution was used in combination with a membrane of DiphPC/DiphPG(80:20) lipids in n-decan or hexadecan.

### Reference Measurement

A reference measurement representative for all GramA experiments is shown in Figure 5.7. These were performed before all other measurements.

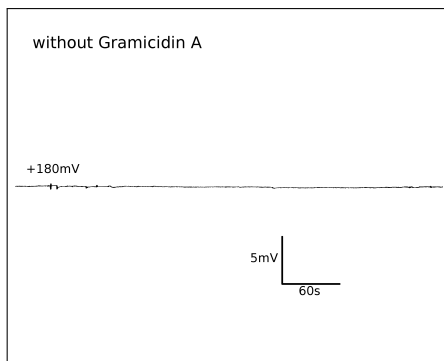


Figure 5.7.: Reference measurement for a bilayer conductivity experiment with GramA. A Dih-phPC/DiphPG lipid mixture in hexadecan was used for the membrane. The applied potential was  $V_a = +180mV$ .

### Conductivity Measurement

One of the six conductivity measurements with GramA was performed with a concentration of 0.1mM at the *cis*-side. The applied potential was only  $|V_a| = 80mV$  and the measuring time was comparatively short. No increase of the conductivity could be observed. A longer measuring time as well as higher applied voltages and higher peptide concentrations (end concentration between 0.1mM - 1mM) were tested in the other experiments. The remaining five conductivity measurements showed an enormous increase of the membrane conductivity. Three of them had a continuous increase while in two of the experiments single pores could be observed. A snapshot of the strip-chart record is shown in Figure 5.8.

An analysis for the pores observed within a snapshot of, for instance, three minutes can be performed. Every single line parallel to the y-axis characterizes the opening or closing of a pore. The pore size is determined by counting the small boxes on the strip chart record. The number of pores of the same size is counted and results in Figure 5.9. The measured current on the y-axis of the strip chart record can be converted (via equation 5.1) into the conductivity of the pore. In Figure 5.9, the maximum number of pores (28), observed within three minutes, shows a pore size of 5pS.

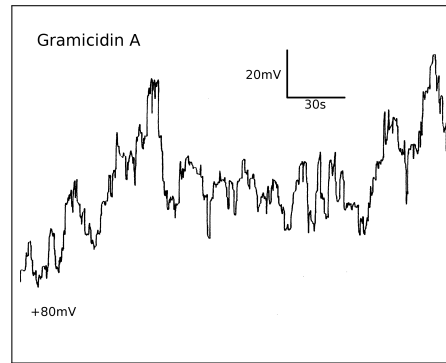


Figure 5.8.: Conductivity measurement for a membrane with DiphPC/DiphPG lipids in hexadecan and the peptide GramA. The increased conductivity was observed with an applied potential of  $V_a = +80mV$ .

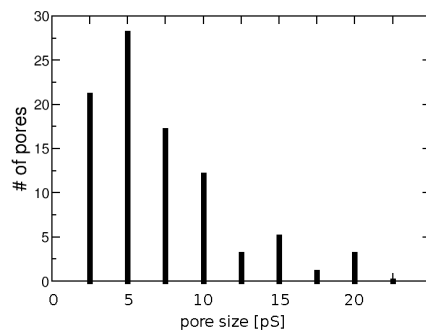


Figure 5.9.: The number of pores and their size in a snapshot (3 minutes) of a bilayer experiment with GramA.

The bilayer experiments showed pore forming of the peptide GramA as described first by Hladky et al. [180]. This assumes that bilayer experiments can be also used to investigate molecules where the behaviour with membranes is still unknown.

## 5.3. Gold Nanoparticles

### 5.3.1. Introduction

Nowadays gold nanoparticles (AuNPs) are widely used in chemistry and biology or technical and medical applications, but their history goes back to ancient rome where the particles were used to produce a red glass color [181]. In biomedical applications they are very promising candidates for diagnostics,

therapies for various diseases like cancer, Alzheimer, HIV and diabetes [182–187]. AuNPs are available in a wide range of sizes from 1 to more than 120nm [182]. The nanoparticles used in this thesis have a size between 1.4 and 15nm. Among a large number of different possibilities for synthesis and stabilization [182], the AuNPs provided by the Simon group in Aachen are stabilized with phosphine-ligands. Pan et al. reported unexpected cytotoxicity of ultrasmall AuNPs, stabilized with phosphine ligands [188]. They investigated nanoparticles from 0.8nm to 1.8nm and 15nm size and found cytotoxicity for particles between 1 and 2nm size [188]. In the following, results of black lipid bilayer experiments performed with nanoparticles of 1.4nm to 15nm size are presented and discussed.

The synthesis of AuNPs with different size and lipids was done by Annika Leifert and Janine Broda (both Simon group, university of Aachen). In the bilayer experiments, AuNPs stabilized with two different phosphine ligands, triphenylphosphine monosulfate (TPPMS) and triphenylphosphine trisulfate (TPPTS), were investigated. Chemical structures for both triphenylphosphine ligands are displayed in Figure 5.10. The ligands are bound via the phosphor atom to the gold surface.

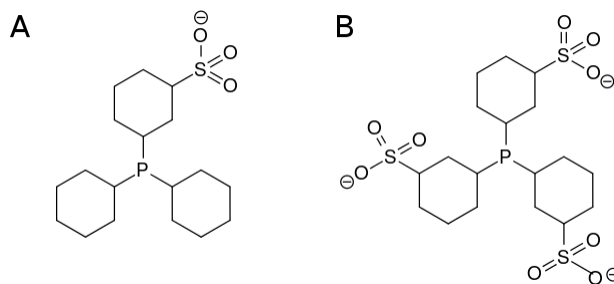


Figure 5.10.: Chemical structure of different ligands used to stabilize gold nanoparticles with a size between 1.4nm and 15nm. (A) Triphenylphosphine monosulfate (TPPMS) and (B) triphenylphosphine trisulfate (TPPTS).

### 5.3.2. Experimental Results

Bilayer experiments were performed as described in section 5.1. The salt solution was 5mM KCl due to instabilities of the gold nanoparticles with higher concentrated salt solutions. The investigated AuNPs are listed in table 5.1. Beside size and ligand, the concentrations of the probes received from Aachen is specified. These concentrations were important to calculate the amount of the probe which has to

be added to receive a distinct end concentration in the Teflon chamber.

Table 5.1.: Gold nanoparticles investigated in black lipid bilayer experiments. The table shows the different sizes and ligands as well as the label of the probes. The ligands triphenylphosphine monosulfate and triphenylphosphine trisulfate are abbreviated with TPPMS and TPPTS respectively. The column headings indicate the labels used in the following sections.

	<b>Au1.4MS</b>	<b>Au4.7MS</b>	<b>Au4.7TS</b>	<b>Au8.2MS</b>	<b>Au10.5TS</b>
size [nm]	1.4	4.7	4.7	8.2	10.5
ligand	TPPMS	TPPMS	TPPTS	TPPMS	TPPTS
concentration [mM]	22.1	25.0	21.8	9.3	71.4
	<b>Au10.6MS</b>	<b>Au10.7MS</b>	<b>Au12.0MS</b>	<b>Au12.1MS</b>	<b>Au15MS</b>
size [nm]	10.6	10.7	12.0	12.1	15
ligand	TPPMS	TPPMS	TPPMS	TPPMS	TPPMS
concentration [mM]	4.4	63.1	5.4	8.0	28.5

The probes for Au10.6MS and 10.7MS were analysed together as well as the probes for Au12.0MS and Au12.1MS. For the probe Au8.2MS, only one experiment was performed, so the analysis is not shown here. Before the experimental results are discussed, an excerpt of a reference measurement is shown.

### Reference Measurement

Reference measurements were performed at the beginning of each experiment. Since all experiments with AuNPs were performed with a membrane composed out of DiphPC lipids in n-decan, only one snapshot out of all reference measurements is shown in Figure 5.11. The applied potential was between  $|V_a| = 50mV$  and  $|V_a| = 150mV$  in the experiments. The snapshot shows a part of a measurement with  $V_a = -150mV$ .

When reference measurements showed no increase of the conductivity and the bilayer seemed to be still stable (visual inspection), the conductivity measurements were performed. In case that visual inspection showed a multi-layer membrane (the membrane is not black anymore), the membrane was destroyed, a new one inserted and the reference measurements repeated. Each time the observation of increased conductivity indicated that the Teflon chamber or other equipment was contaminated by membrane active compounds from previous experiments, the experiment was completely stopped and the preparation of the experimental set up was started again.

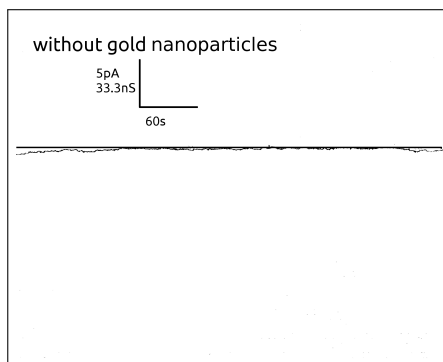


Figure 5.11.: Conductivity measurement without addition of gold nanoparticles. The strip-chart recording of a measurement with a DiphPC bilayer and an applied voltage of  $-150\text{mV}$  is shown as a representative snapshot for all reference measurements, which were performed at the beginning of every single experiment.

### Conductivity Measurements

Conductivity measurements were performed for different sized AuNPs stabilized by TPPMS. While all particles smaller than  $12\text{nm}$  showed no increase of the conductivity, the conductivity showed an increase in experiments with Au12MS, Au12.1MS and Au15MS. Representative snapshots out of the strip-chart records for experiments with TPPMS stabilized AuNPs are displayed in the following two paragraphs discussing these experiments.

#### Results for Au1.4MS, Au4.7MS and Au10.7MS

Four different conductivity measurements for Au1.4MS were performed. The end concentration was usually  $0.5\text{mM}$  at the *cis*-side of the membrane and was increased to  $1\text{mM}$  in one experiment. The maximum applied potential was  $100\text{mV}$ . Nevertheless, an increase of the conductivity was never observed for Au1.4MS. Figure 5.12 shows a part of the strip-chart recording for one of these measurements.

For Au4.7MS, only one experiment could be performed due to the restricted time in the lab. Again the end concentration was  $0.5\text{mM}$  at the *cis*-side of the membrane. The applied maximum potential was  $|V_a| = 150\text{mV}$ . Figure 5.13 shows a part of the strip chart record. Although only one measurement was performed, the result is shown here because of the possibility to compare TPPMS stabilized AuNPs directly with TPPTS stabilized particles of the same size. This comparison is made in the discussion in

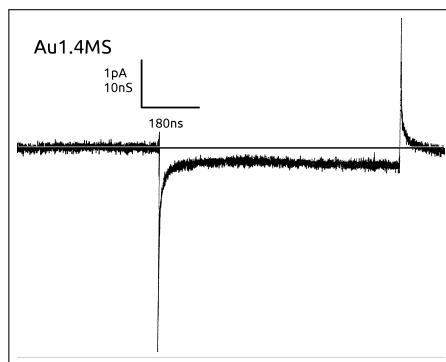


Figure 5.12.: Conductivity measurement for a DiphPC bilayer after addition of Au1.4MS. The applied voltage was  $V_a = 0mV$ ,  $V_a = -100mV$ ,  $V_a = 0mV$ . No increase of the conductivity was observed.

### Section 5.3.3.

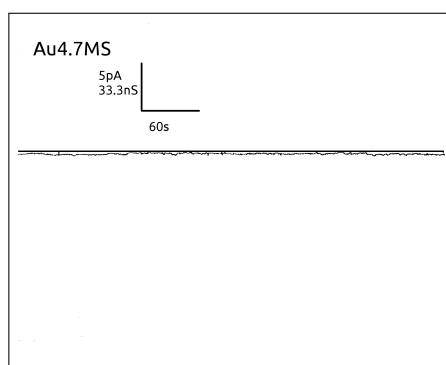


Figure 5.13.: Conductivity measurement with Au4.7MS. The applied voltage was  $-150mV$ .

For Au10.6MS and Au10.7MS, in total seven experiments were performed with an AuNP concentration of  $0.5mM$  at the *cis*-side. Two of the measurements had a maximum potential of  $|V_a| = 470mV$  and are not discussed further. The possibility to apply such a high voltage indicates the forming of a multi-layer during the experiment. Unfortunately, the membrane cannot be observed during experiments with AuNPs due to the red tinting of the solution after addition of the compound. Therefore the measurements were performed as usual but such high voltages were used as criterion to discard the measurement. The maximum potential in the remaining five experiments are in the same range as in other experiments with AuNPs, e.g. between  $100mV$  and  $180mV$ . All measurements show no increase of the conductivity. The increase of the concentration of the AuNPs to  $1mM$  in one of the experiments

also showed no effect. The strip chart record for an applied potential of  $-150\text{mV}$  and Au10.7MS is shown in Figure 5.14.

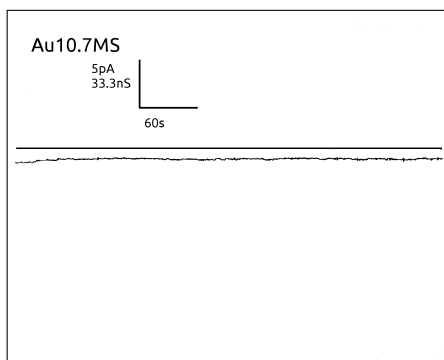


Figure 5.14.: Conductivity measurement with Au10.7MS. The applied voltage was  $V_a = -150\text{mV}$ . No increase of the conductivity was observed.

### Results for Au12MS and Au15MS

Six experiments with Au12MS and Au12.1MS were performed with an end concentration of  $0.5\text{mM}$  at the *cis*-side of the Teflon chamber. In one experiment the membrane seemed to be a multi-layer, but all the remaining five experiments show an increase of the conductivity. A snapshot for an experiment with Au12.0MS is shown in Figure 5.15.

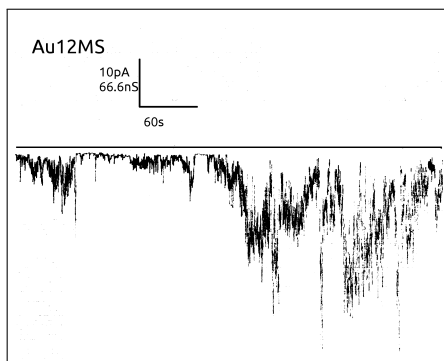


Figure 5.15.: Conductivity measurement with Au12MS. The applied voltage was  $V_a = -150\text{mV}$ . An increase of the conductivity was observed.

For the Au15MS, different results were obtained. While experiments in the first weeks in the lab showed an increase of the conductivity for four experiments, one experiment with the same solution

more than 1.5 years later showed no increase of the conductivity. Here it can be assumed that this result was due to the use of the old solution, but only one experiment is not really sufficient to interpret the result. The strip chart record for one of the first four experiments is shown in Figure 5.16. The applied potential was only  $|V_a| = 50\text{mV}$ . The end concentration of Au15MS was  $0.5\text{mM}$  at the *cis*-side.

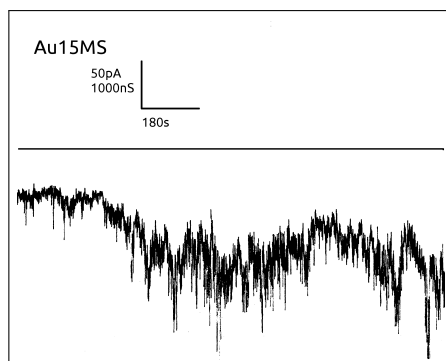


Figure 5.16.: Conductivity measurement with Au15MS. The applied voltage was  $V_a = -50\text{mV}$ . An increase of the conductivity was observed.

Conductivity measurements in bilayer experiments for TPPMS stabilized AuNPs show a size dependent effect. While particles smaller than  $12\text{nm}$  show no effect on the membrane conductivity, experiments with bigger nanoparticles lead to an increase of the conductivity.

### Results for Au4.7TS and Au10.5TS

To investigate if not only the size of the nanoparticles, but also the ligands with which they are stabilized is crucial for interactions between membrane and AuNPs, two TPPTS-stabilized nanoparticles with similar size to TPPMS-stabilized particles were investigated.

Four experiments with an end concentration of  $0.5\text{mM}$  Au4.7TS at the *cis*-side were performed. All experiments showed an increase of the conductivity. A snapshot is displayed in Figure 5.17.

With Au10.5TS three experiments were performed. The end concentration in the Teflon chamber was  $0.5\text{mM}$  at the *cis*-side. The applied maximum potential was  $|V_a| = 150\text{mV}$ .

These results of the bilayer experiments with TPPTS-stabilized nanoparticles show that also the lig-

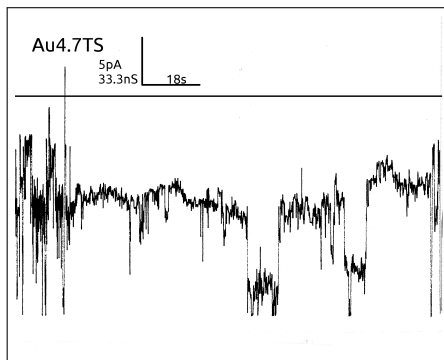


Figure 5.17.: The conductivity measurement with 0.5mM concentration of Au4.7MS at the *cis*-side of the Teflon chamber show an increase of the conductivity. The applied potential was  $V_a = -100mV$ .

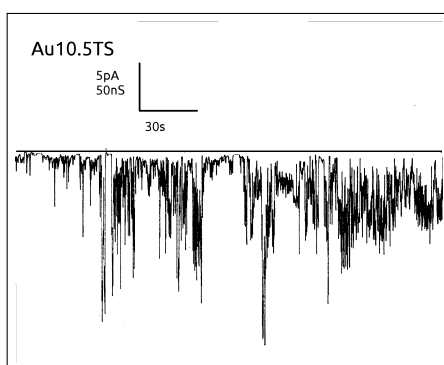


Figure 5.18.: Conductivity measurement of a DiphPC membrane with Au10.5TS. The concentration of the nanoparticles was 0.5mM at the *cis*-side. The applied potential was  $V_a = -150mV$ . An increase of the conductivity was observed.

ands play an important role in the interactions of membranes and ligand stabilized AuNPs. Both TPPTS-stabilized AuNPs show an increase of the membrane conductivity, whereas TPPMS-stabilized nanoparticles of the same size show no effect.

### Selectivity Measurements

The results of the conductivity measurements, which show size-dependent membrane interactions of AuNPs as well as different behaviour for different ligands stabilizing the AuNPs allows further investigation of the membrane influenced with AuNPs by selectivity measurements.

The selectivity measurements (see also Section 5.1.2) were performed four times for Au15MS and started with a conductivity measurement. After an increase of the conductivity the applied voltage was turned

of and a voltmeter was used instead of the strip chart recorder to measure the membrane potential. To establish a salt concentration gradient,  $100\mu\text{l}$  50mM KCl were added to the *cis*-side of the membrane and to avoid hydrostatic pressure differences  $100\mu\text{l}$  5mM KCl were added to the *trans*-side. The membrane potential was measured after five minutes and the procedure was repeated till the membrane broke. The results of the measurement are displayed in Figure 5.19.

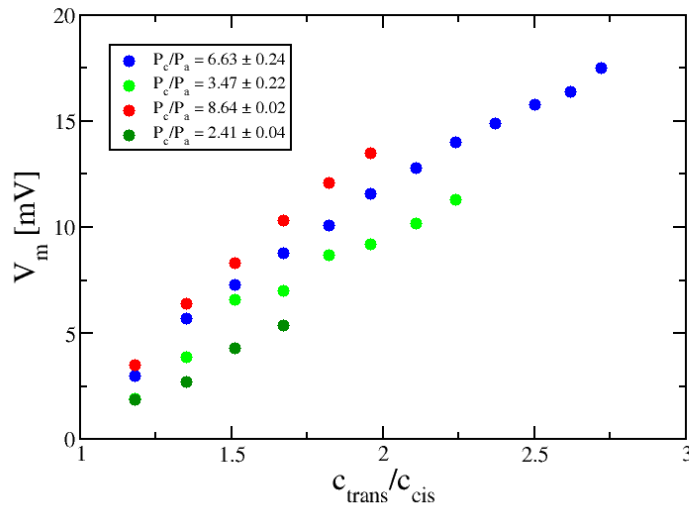


Figure 5.19.: The plot shows results for four selectivity measurements (coloured in different colours) of a DiphPC membrane with Au15MS. The average and variance of the permeability ratio between  $P_c$  and  $P_a$  is denoted in the legend.

The cation/anion permeability ratio is positive in all measurements. This indicates that the membrane is selective for cations.

### 5.3.3. Discussion

Gold nanoparticles are very promising for biomedical applications [182–187], but the knowledge about their interactions with other biomolecules and membranes is still limited and needs to be investigated. For instance, experiments by Pan et al. surprisingly showed size dependent cytotoxicity of TPPMS stabilized nanoparticles. Au1.4MS as well as Au1.4TS were highly toxic, while Au15MS was comparatively nontoxic [188].

In order to understand possible mechanisms, interactions with membranes must be investigated. There-

fore different gold nanoparticles stabilized with TPPMS ligands were used in bilayer experiments. They show a size dependent membrane activity: Experiments with DiphPC membranes and Au1.4MS, Au4.7MS, Au10.6MS or Au10.7MS show no increase of the membrane conductivity, while Au12.0MS and Au15.0MS increased the membrane conductivity. Gold nanoparticles with a similar size, stabilized with TPPTS, show a different behaviour. Experiments with Au4.7TS and Au10.5TS show membrane interactions leading to an increased conductivity, whereas TPPMS stabilized AuNPs of the same size had no effect. Therefore not only the size, but also the ligands on the gold cluster play an important role for size dependent interactions of gold nanoparticles with membranes.

In order to understand the membrane activity, a model was developed. The membrane in bilayer experiments is assumed to be between 5nm and 8nm thick [189] and is composed of a hydrophobic core embedded in two hydrophylic headgroup regions. The gold nanoparticle is a hydrophobic core stabilized by phosphine ligands. The TPPMS ligands carry one unit charge, TPPTS ligands carries three unit charges. For the different nanoparticles the number of ligands as function of the nanoparticles size was estimated. While a completely covered 1.4nm sized AuNP has 12 ligands, for bigger nanoparticles, the number of ligands  $n$  can be calculated by the following equation:

$$n = \frac{A_{AuNP}}{A_{TPPMS}} \quad (5.4)$$

where  $A_{AuNP}$  is the surface of the AuNP and  $A_{TPPMS} = 1.23nm^2$  is the area covered by a TPPMS ligand. For instance calculating the surface of Au15MS with a radius of 7.5nm, the surface results in  $A_{AuNP} = 706.86nm^2$ . The number of ligands on the surface of Au15MS is therefore  $n = \frac{706.86nm^2}{1.23nm^2} \approx 575$ . Numbers for all particle sizes used in the experiment can be found in table 5.2.

In addition to the maximum number of ligands  $n$ , the number of ligands inside the membrane is calculated under the assumption that the AuNP is in the center of the membrane. For a thickness of 5nm and 8nm, the numbers are shown in table 5.2. A visualisation of the number is displayed in Figure 5.20.

Since the transfer of charged groups from highly polar regions like water to hydrophobic regions like the membrane core is energetically unfavourable, these numbers suggest that nanoparticles with bound

Table 5.2.: This table shows the size and the corresponding maximum number  $n$  of ligands for AuNPs used in the bilayer experiments. Assuming that the AuNP sits in the membrane center and the bilayer is between 5nm (membrane-5) and 8nm (membrane-8) thick in the experiments, the number of ligands which should be inside the membrane is given by  $n_{membrane-5}$  and  $n_{membrane-8}$ .

size[nm]	$n$	$n_{membrane-5}$	$n_{membrane-8}$
1.4	12	12	12
4.7	56	56	56
10.6	287	135	217
12.0	368	153	245
15.0	575	192	307

ligands cannot enter the hydrophobic membrane region. Therefore the question arises if the ligands unbind before they enter the membrane.

Since for triphenylphosphine-stabilized AuNPs a dissociation equilibrium of bound and free ligand molecules in solution is known [190], the different behaviour of TPPMS and TPPTS in membrane activity can only be understood, if TPPTS ligands are more weakly bound than TPPMS. First stability test of our co-workers confirm this assumption: For TPPMS- and TPPTS-stabilized particles of the same size more TPPTS-stabilized AuNPs are dissociated in solution than particles stabilized with TPPMS ligands.

Both of these ligands are bound to the gold surface via a phosphorus atom. Since the electronegativity of phosphorus is 2.19 and the electronegativity of gold is 2.54, a small amount of negative charge will be induced in the gold surface. This would enable a cation transport through the membrane if the gold nanoparticles sat inside the membrane. The selectivity measurements in the bilayer experiments performed with Au15MS showed that the membrane is cation selective. Therefore the model is in good agreement with the experimental results.

All these findings support a mechanism that ligands dissociate when the particles enter the membrane and are consistent with the observation that small nanoparticles which cannot span the membrane show no effect.

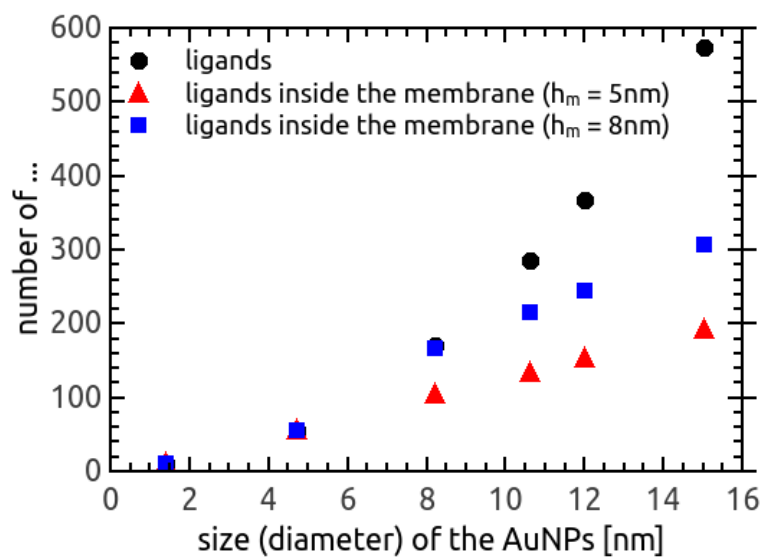


Figure 5.20.: The maximum number of ligands for AuNPs with different size (black circle) is shown. When the particle's center is assumed to be in the membrane center, for each particle size a different number of ligands is bound to the surface of the AuNP inside the membrane. These numbers are displayed for a 5nm (red triangle) and a 8nm (blue square) thick membrane.

## 6. Interaction Between the hERG Ion Channel and Gold Nanoparticles

*This work is published in Proceedings of the National Academy of Sciences (PNAS) as part of Leifert et al. [3].*

Gold nanoparticles are promising compounds for many applications in medical research. They are used in bioimaging, gene delivery, drug delivery and other therapeutic and diagnostic applications [183–187]. In pre-clinical testing, essentially all drug candidates are investigated together with the hERG channel. The hERG (human *ether-a-go-go*-related gene) [191] potassium channel is essential for normal electric activity in the human heart [192–194]. Due to the known interaction of many drug candidates [194], this testing was performed also for gold nanoparticles.

The Simon group in Aachen observed that phosphine-stabilized gold nanoparticles (AuNPs) irreversibly block hERG channels in patch-clamp experiments, whereas thiol-stabilized AuNPs of similar size had no effect on the channel function *in vitro*, and neither particle blocked the channel *in vivo* [3]. The nanoparticle is covered with ligands, but some experimental and theoretical results, discussed in this chapter, lead to the assumption that displacement of ligands and therefore the accessibility of the gold core surface is crucial for the blocking mechanism of phosphine-stabilized AuNPs. To test this assumption, docking simulations were performed.

The docking simulations for gold nanoparticles to the hERG channel were performed with SIMONA [54] and are discussed in Section 6.3. Section 6.1 explains the function of the hERG potassium channel

and summarizes the basics of the human ventricular action potential. Results of patch-clamp experiments by Leifert et al. [3] are summarized in 6.2. While basics for the gold nanoparticles in general can be found in Section 5.3 of the previous chapter, the input structures used for this study and simulation details are described in Section 6.3.

## 6.1. The hERG Channel and the Long QT Syndrome

The hERG potassium channel [191] is essential for normal electric activity in the heart [192–194]. The ion channel is voltage-gated and, together with other ion channels regulates the cardiac action potential and the heartbeat.

The human heart has four chambers, two atria and two ventricles, which contract consecutively in a cardiac cycle. During such a cycle, which corresponds a single heartbeat, electric currents can be measured with electrodes attached to the surface of the skin. The current can be displayed in an electrocardiogram (Figure 6.1A). In the scheme a P wave, a QRS complex and a T wave can be distinguished. While the P wave displays the atrial depolarisation, the QRS complex reflects the rapid depolarisation of both ventricles. The T wave indicates the repolarisation of the ventricles. Focusing on the ventricular action potential in Figure 6.1B, five different phases can be distinguished: While phase 0 describes the rapid depolarisation of the membrane, the repolarisation is divided into three phases. After a short rapid repolarisation (phase 1), the repolarisation plateau is reached (phase 2), followed by phase 3 which terminates the action potential and returns the potential to the resting level (phase 4) [194]. Therefore phase 0 corresponds to the QRS complex, while the T wave reflects the repolarisation in phase 1-3. The complete ventricular action is therefore described by the QT interval of the electrocardiogram.

The hERG channel is responsible for the rapid delayed rectifier  $K^+$  current in phase 3 [192–194]. Mutations or blocking of the channel cause the long QT syndrome [195]. A prolongation of this interval characterises the long QT syndrom [195], which causes arrhythmia, rapid irregular heart beats that can lead to fainting and sudden death [194]. The syndrome can be either a rare inborn heart condition or a side-effect of drugs.

In the past, promising drug candidates that passed initial cytotoxicity screens turned out to be highly

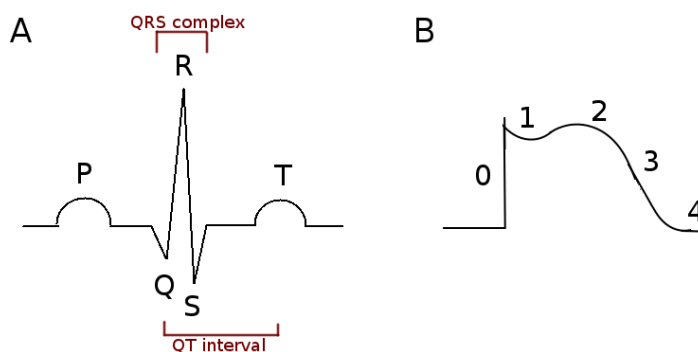


Figure 6.1.: (A) An electrocardiogram displays the cardiac cycle of a heartbeat. The P wave describes the depolarisation of the atria while the QRS complex refers to the depolarisation of the ventricles. The QT interval incorporates the depolarisation as well as the repolarisation of the ventricles and therefore describes the whole ventricular action potential. (B) The human ventricular action potential shows four different phases: a rapid depolarisation of the membrane (phase 0), repolarisation (phase 1 - 3) and the resting level (phase 4).

cardiotoxic in preclinical trials due to their interaction with the *hERG/K<sub>v</sub>11.1* channel [3, 194], thus several drugs had to be removed from the market [196]. Today, tests for hERG channel activity are a significant hurdle in the development of new drugs [197].

## 6.2. Experimental Results

Gold nanoparticles play an important role in medical research. They can be used in bioimaging, gene delivery, drug delivery and other therapeutic and diagnostic applications [183–187]. Due to the known interaction of the hERG channel with many drug candidates [194], a non-clinical testing strategy is recommended to determine if a delay of the ventricular repolarisation is caused by the compound in question [198].

Leifert et al. performed whole-cell patch-clamp recordings to evaluate the effect of phosphine-stabilized (TPPMS) AuNPs, Au1.4MS, on the hERG tail currents [3]. They found an irreversible blocking of the channel for Au1.4MS, while tests with TPPMS ligands only had no effect on the hERG current amplitudes [3]. Thiol-stabilized particles show no effect in patch-clamp experiments as well. It is assumed that the gold cores of thiol-stabilized AuNPs are shielded sufficiently to prevent interaction with biological targets, whereas Au1.4MS can shed off its weaker bound phosphine shell and thus

interact with biological target molecules [3]. A recent study by Pan et al. showed that cytotoxicity of Au1.4MS can be suppressed by an excess of TPPMS [199]. Additional patch-clamp experiments with a mixture of Au1.4MS and TPPMS or preincubated cells were performed. The addition of excess free TPPMS ligands abolished the hERG channel block by Au1.4MS, while a preincubation of the cells with TPPMS before application of Au1.4MS did not prevent the current inhibition [3]. Since a dissociation equilibrium of bound and free ligand molecules is known for triphenylphosphine-stabilized AuNPs [200] it can be assumed that an excess of TPPMS shifts the equilibrium and therefore makes the particle surface less accessible [3].

### **6.3. Docking Simulations**

Docking simulations are used to predict preferred orientations between a small molecule to a large protein target and to estimate binding affinities [201, 202]. To prove the hypothesis that the accessibility of the gold core surface is crucial for the blocking mechanism of Au1.4MS [3], such simulations were performed using SIMONA [54].

#### **6.3.1. Gold Nanoparticles**

In the experimental studies, 1.4nm sized nanoparticles with 55 gold atoms were used. The AuNPs are stabilized with triphenylphosphine monosulfate (TPPMS) (for the chemical structure see Chapter 5.3), wherefore the nanoparticles are labeled as Au1.4MS.

The TPPMS ligands were attached to the apex gold atoms of the cluster. Since SIMONA [54] uses classical force fields, binding and unbinding of ligands cannot be modelled, wherefore structures with varying numbers of ligands were generated. Due to a maximum number of twelve ligands for the Au1.4 molecules with  $n = 0, 2, 4, 6, 12$  were prepared, labeled as Au1.4MS( $n$ ) in the following.

To obtain the input structures in Figure 6.2, SIMONA [54] simulations had to be performed. A structure for the icosahedron Au<sub>55</sub> cluster was obtained from the Cambridge Cluster database [203, 204]. The TPPMS ligands were constructed with PyMol [205] and their charge distribution was calculated by Gesa Lüdemann using DFT calculations with Turbomole [76]. The desired number of ligands was added close to the gold cluster and relaxed with a distance constraint such that the distance of the

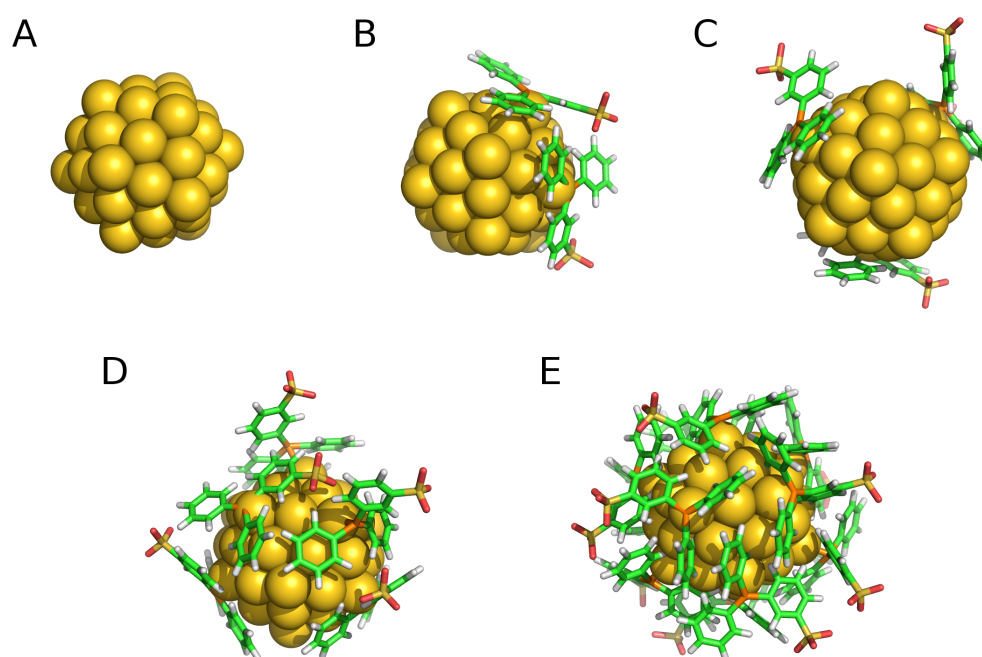


Figure 6.2.: Phosphine-stabilized gold nanoparticles with different numbers of ligands  $n = 0, 2, 4, 6, 12$ . The gold nanoparticle is comprised of 55 gold atoms and stabilized by triphenylphosphine monosulfate (TPPMS). The figure shows input structures for docking simulations without ligands (A), partially covered with two (B), four (C) or six (D) ligands. The completely covered nanoparticle with twelve ligands is displayed in the last panel (E).

phosphine atom of the ligand to the apex gold atom equals the usual bond length.

### 6.3.2. Homology Model for the hERG Channel

Despite enormous efforts, crystal structures of membrane-bound receptors and ion channels are still rare [4, 206, 207]. Therefore homology modelling is widely used to build structural protein models used to study interactions between small ligands and these channels [208, 209]. Due to homology to the Mammalian Shaker Kv1.2 potassium channel (PDB: 2a79) [210], Irene Meliciani constructed a model for the hERG channel which agrees well with the hERG consensus model [211]. Top and side view of the model are displayed in Figure 6.3.

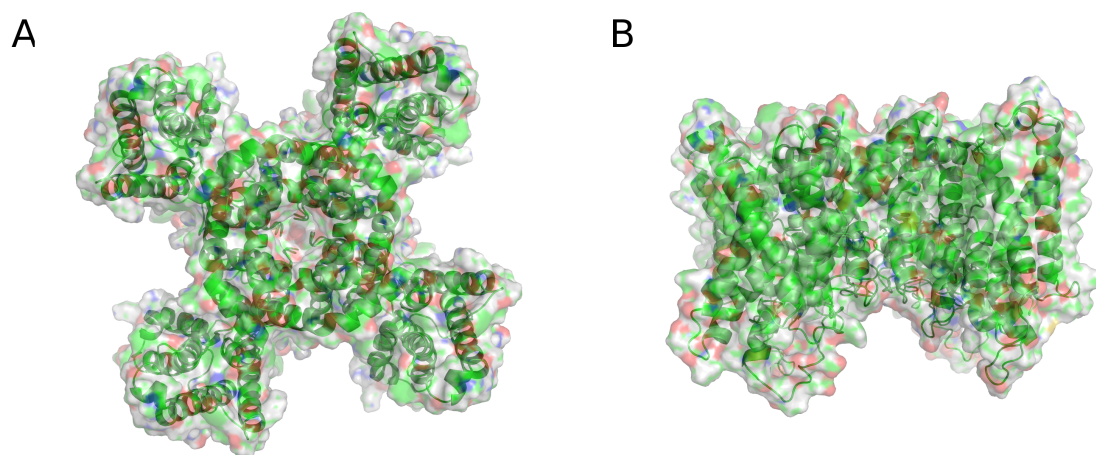


Figure 6.3.: Top (A) and side (B) view of the homology model to the Mammalian Shaker Kv1.2 potassium channel [210]. The top view of the channel shows the intracellular entry side.

### 6.3.3. Docking Results

For Au1.4MS(12) MC simulations with starting conformations on both the intra- and the extracellular entrances of the channel were performed. The nanoparticle explores the vicinity of the channel entrance of the pore but does not dock. Since parametrization at pH 7.4 results in a total charge of -11 for the hERG channel (the electrostatic potential is shown in 6.4) and -12 for Au1.4MS(12), docking is prevented by the large Coulomb repulsion.

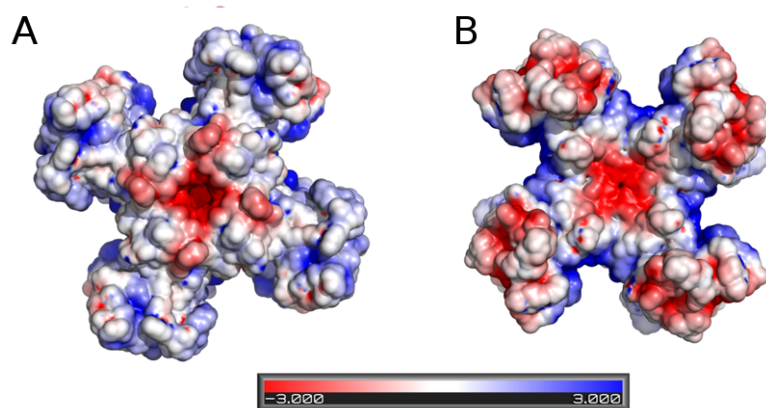


Figure 6.4.: The electrostatic potential on the molecular surface of the hERG channel parametrized at pH=7.4 was calculated using the adaptive Poisson-Boltzmann Solver (APBS) [212] tool in PyMol [205]. Panel A shows the entry side of the channel, Panel B the exit side.

As a result, additional simulations with a channel parametrized at pH 6.7 were performed. The total

charge for a pH 6.7 channel is zero. Figure 6.5 shows the electrostatic potential on the channel surface differs significantly from the pH 7.4 model. Simulations with Au1.4MS(12) show that the nanoparticle binds weakly to this channel at the lower pH value.

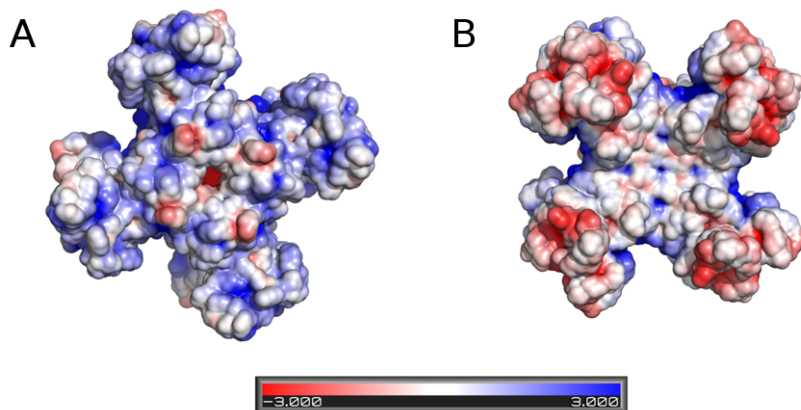


Figure 6.5.: The electrostatic potential on the molecular surface of the hERG channel parametrised at pH=6.7 was calculated using the adaptive Poisson-Boltzmann Solver (APBS) [212] tool in PyMol [205]. Panel A shows the entry side of the channel, Panel B the exit side.

The fact that Au1.4MS(12) binds to the hERG channel at pH=6.7 whereas Au1.4MS(12) shows no binding to the more negatively charged pH=7.4 channel suggests that displacement of ligands could lead to binding of the nanoparticles to the channel. Therefore Au1.4MS(8), Au1.4MS(6), Au1.4MS(4) and Au1.4MS(2) were simulated analogously to Au1.4MS(12) with the same simulation set up.

The results show that binding becomes increasingly likely as the number of ligands on the nanoparticles decreases and therefore confirm the hypotheses that the accessibility of the gold surface is crucial for the blocking mechanism. Interpolation between the docking results for the two channel models indicates that at least some ligands need to be displaced from the Au<sub>55</sub> core to obtain a stable complex between the channel and the AuNP, even if the complex environment of membrane and ions is not fully accounted for in the simulations [3].

#### 6.3.4. Summary

Patch-clamp experiments of the Simon group in Aachen showed that some gold nanoparticles irreversibly block the hERG channel. The atomic interactions that lead to this irreversible blocking of

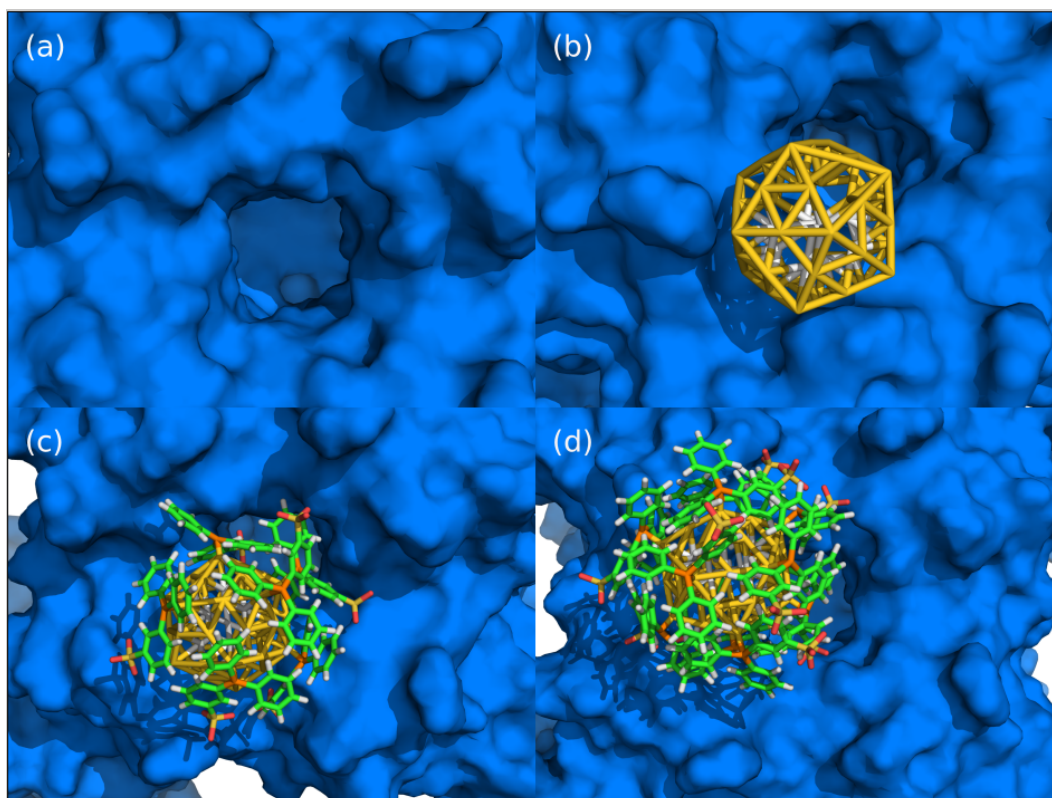


Figure 6.6.: (a) The hERG channel and snapshots for the docking simulations of (b) Au1.4MS(0), (c) Au1.4MS(6) and (d) Au1.4MS(12). The channel surface is coloured in blue, the ligand is coloured element specific (C: green, O: red, S: yellow, P: orange, H: white) (image similar to [3]).

the channel for triphenylphosphine monosulfonate stabilized nanoparticles were studied as part of this dissertation by docking simulations for gold nanoparticles coated with a different number of ligands. Interpolation between the docking results for two different channel models indicated that at least some ligands need to be displaced from the gold cluster to obtain a stable complex between the channel and the gold nanoparticle. These results complement the experimental observation of co-workers in Aachen. They found that a mixture of Au1.4MS with an excess of the phosphine ligands led to a disappearance of the channel blocking behavior [3]. This study demonstrates that binding modality of surface functional groups to nanoparticles have a strong influence on their interactions with biomolecules. Therefore safety regulations for using gold nanoparticles in industrial or medical products will have to be adapted [3].

## 7. Summary

Proteins are the nano-scale machinery of living cells and involved in many biological activities, such as catalysis of biochemical reactions, transport mechanisms, signaling or energy conversion. The unique structures into which many proteins fold enables them to fulfill this wide range of functions. Therefore, structural knowledge is crucial for determining the function of proteins or understanding the mechanism behind their function. Their three dimensional structure depends on the amino acid sequence and the physiological environment of the protein. Beside proteins in solution, around 20 to 30 % of all proteins are embedded in biological membranes. Experimental structure investigations, like NMR spectroscopy or X-ray crystallography, are especially challenging for the latter group due to the hydrophobic environment that the membrane presents. In addition, those experiments provide mostly static views of proteins and their interaction partners, while protein functions are inherent dynamic processes. A helpful tool for investigating protein structures and functions are computational methods. Nowadays, these methods are also common in drug development, because malfunction of proteins is the cause of many diseases.

The main focus of my thesis was theoretical and experimental investigations of biomolecular processes related to the interaction of proteins and gold nanoparticles with biological membranes and membrane-bound proteins. In order to perform the necessary simulations for this study, I participated in developing, implementing and validating computational methods that enable these studies. To characterize the influence of antimicrobial peptides and gold nanoparticles on the hydrophobic barrier established by a biological membrane, I performed and analyzed black lipid bilayer experiments. To understand the interactions of certain gold nanoparticles with the membrane bound hERG ion channel in more detail, I studied the requirements to form a stable complex between these two with atomistic si-

mulations. The results of these investigations will be explained in more detail in the rest of this chapter.

Since proteins and membranes play a fundamental role in this thesis, their composition and main functions are summarized in Chapter 2. Docking simulations and implicit membrane simulations were performed using the Monte Carlo software package SIMONA. The basic theory behind Monte Carlo simulations is reviewed in the beginning of Chapter 3. All Monte Carlo simulations I have presented in this thesis use a reduced set of degrees of freedom compared to explicit all-atom Molecular Dynamics simulations. Therefore, I validated a new dihedral potential implementation in combination with additional amino acid side chain degrees of freedom. I computed the free energy landscapes of dipeptides with this new method. These possess the expected minima for the well-known regions of secondary structure in good agreement with prior investigations by others. I compared the alanine dipeptide in more detail to explicit solvent simulations with a similar force field, where I found a comparable free energy landscape in the low-energy region, but steeper barriers. This can be explained by the existence of additional degrees of freedom for bond stretching and angle bending in Molecular Dynamics simulations, which allows the atoms to avoid Lennard-Jones clashes.

Encouraged by this result, I investigated the stability of several small proteins, a Villin headpiece mutant and the WW-domain. These two proteins were chosen because of their completely different secondary structure. While the native structure of both proteins is stabilized at low temperatures, folding and unfolding events could be observed at higher temperatures. In comparison to other methods, the computational effort to observe such events is extremely low. However, my simulations showed that the estimation of the folding temperatures is difficult, wherefore advanced techniques like Parallel Tempering should be used in the future. Since differences between the computed and experimental temperatures were observed, further studies have to determine the reason for that behavior.

An important aspect of this problem is the implicit treatment of the solvent. In the last paragraph of Chapter 3, I have compared three different models to describe the nonpolar contribution to the solvation free energy using optimized parameters for small organic molecules. This energy contribution is crucial for the correct estimation of hydration free energies, which are very important in drug development for the prediction of ligand binding affinities to target proteins. My analysis of the computed

---

---

hydration free energies using these models and optimized parameters showed that implicit models can outperform the TIP3P explicit water models in accurately estimating hydration free energies of small molecules [1], but they also highlighted that atoms with the same atom type but differing partial charge are one source of main error for these models. In a next step, hydration free energy comparisons for larger molecules should be performed to determine if the performance of these models also holds for macromolecules such as proteins. The analysis will also help to improve the large number of other implicit solvent models implemented in molecular simulation packages.

Membrane proteins are essential for many biological activities, but the complex hydrophobic environment makes experimental and computational studies challenging. I therefore participated in the development of an implicit membrane model SLIM (SIMONA layered implicit membrane), which combines advantages of other previous published models regarding the accurate modeling of electrostatic effects inside membranes. In Chapter 4, I have explained the underlying idea of this model and provide a comparison to Poisson-Boltzmann reference calculations to validate the accuracy of the model. The results highlight that the model captures all features of Poisson-Boltzmann electrostatics at a fraction of the computational cost. The features include good quantitative and qualitative agreement of self-energy terms for simple and complex molecular geometries, as well as the interaction of charged ions inside the membrane.

In the last part of Chapter 4, I have shown a comparison of simulation results of three well-studied membrane proteins to experimental and theoretical data. A diploma student of mine and I used Melittin of bee venom to compare the center of mass position of the protein relative to the membrane with experimental measurements. Tilt angles of a monomeric M2 transmembrane domain and both tilt and crossing angles of a Glycophorin A transmembrane dimer were compared to experiments and other computational studies. The results demonstrate that this new implicit membrane model is able to reproduce known properties of these proteins [2].

For the future, different Monte Carlo moves should be tested to improve the efficiency of the simulation protocol. Further optimizations can be done with a parallelization of the code to achieve better sampling and to reach converged results faster. The use of this implicit model will enable the investigation

of processes like protein assembly inside the membrane, which are out of reach for explicit membrane simulations due to the high computational cost. Currently, I use this model to investigate the interactions between different membrane proteins in cooperation with the Ulrich NMR group at the Karlsruhe Institute of Technology.

Chapter 5 describes the black lipid bilayer experiments we performed with antimicrobial peptides and differently sized gold nanoparticles in the lab of Prof. Dr. Dr. h.c. Dr. h.c. Roland Benz in Würzburg. Ultrasmall gold nanoparticles have recently been reported to show toxicity, but the mechanism behind this toxicity is still not understood. In this work I performed experiments to investigate the interaction of gold nanoparticles as function of their size and functionalization to address the obvious question how these particles interact with biological membranes as the natural barrier of the cell. Together with a diploma student, Yvonne Klapper, I used the bilayer experiments with antimicrobial peptides to establish a working experimental setup. I subsequently performed experiments with gold nanoparticles of different sizes to get a complete picture of the size-dependent cytotoxicity found by our co-workers from Aachen. I observed a size-dependent increase of the membrane conductivity in my experiments. In addition, I was able to show that gold nanoparticles stabilized with triphenylphosphine trisulfonate instead of triphenylphosphine monosulfonate show a different behavior in the experiments. I established a model for ligand displacement when the gold nanoparticles enter the membrane to explain the possible underlying process, which is supported by additional experiments of my co-workers. Future investigation of fluorescence labeled nanoparticles as well as further experiments with smaller triphenylphosphine trisulfonate stabilized nanoparticles will provide further insights into the effects these nanoparticles have on living cells.

Chapter 6 focuses on the docking simulations between triphenylphosphine monosulfonate stabilized gold nanoparticles and the hERG (human ether-a-go-go-related gene) potassium ion channel. The channel is crucial for normal activity of the human heart and used in pre-clinical testing for essentially all drug candidates. I performed docking simulations for gold nanoparticles coated with a different number of ligands and the hERG channel to study the atomic interactions that lead to irreversible

---

---

blocking of the channel for phosphine-stabilized nanoparticles. Interpolation between the docking results for two different channel models indicated that at least some ligands need to be displaced from the gold cluster to obtain a stable complex between the channel and the gold nanoparticle. My findings complement the experimental observation of my co-workers in Aachen that an excess of the phosphine ligands led to a disappearance of the channel blocking behavior of the gold nanoparticle. These results help to demonstrate that binding modality of surface functional groups to nanoparticles have a strong influence on their interactions with biomolecules. Therefore, safety regulations for using gold nanoparticles in industrial or medical products will have to be adapted [3].



## A. PBEQ-Solver Settings

PB calculations were performed with the PBEQ solver [115, 116]:

**! adjustable PBEQ parameters**

set EpsR = 2 ! dielectric constant for the reference environment

set EpsP = 2 ! dielectric constant for the protein interior

set EpsW = 80 ! solvent dielectric constant

set Conc = 0 ! salt concentration

set Focus = 1 ! to have a refined calculation focused on the site using a finer grid

set Dcelc = 1.0 ! the grid spacing in the finite-difference (centered on Xcen, Ycen, Zcen)

set Dcelf = 0.25 ! the grid spacing in the finite-difference (centered on Xcen, Ycen, Zcen)

set LEdge = 25 ! distance between a protein atom and a grid LEdge\*2 for coarse-grid calculations and LEdge/2 for fine-grid calculations (see below)

set Options = watr 1.4 reentrant ! Let's use the molecular surface

**! membrane stuff**

set Tmemb = 30 ! thickness of membrane (along Z)

set Zmemb = 0 ! center of membrane (along Z)

set epsM = 2 ! membrane dielectric constant

set Htmemb = 5 ! thickness of headgroup region

set epsH = 7 ! membrane headgroup dielectric constant



## B. SIMONA Simulations

PDB files were read in and processed by `pdb2gmx` from the GROMACS package [42, 74], using the Amber99SB\*-ILDN force field [58–60]. Structures were energetically minimized using GROMACS. Resulting structures were used as input structures for SIMONA [2, 54] simulations. No force field cutoffs were used during the simulations.

We gratefully thank the bwGRiD project[213] for the computational resources.



## C. Additional Software Used in This Thesis

- PyMol [205]
- Gimp [214]
- Xmgrace [215]
- QtiPlot [216]
- LibreOffice [217]
- Matplotlib [77]
- Bkchem [218]
- Open Babel [219]
- PDB2PQR [220]
- Inkscape [221]



# List of Figures

2.1. Peptide bond . . . . .	8
2.2. Amino acids . . . . .	9
2.3. Secondary structure: Helix and beta-sheet. . . . .	11
2.4. Tertiary Structure: Myoglobin. . . . .	12
2.5. Quaternary Structure: Haemoglobin. . . . .	13
2.6. Folding funnel. . . . .	14
2.7. Bilayer composition. . . . .	15
2.8. Phospholipid: DiphPC. . . . .	16
3.1. Explicit water and explicit membrane. . . . .	19
3.2. Metropolis Monte Carlo. . . . .	20
3.3. Atoms and dihedral angles in leucine residue. . . . .	25
3.4. Alanine dipeptide. . . . .	26
3.5. Free energy landscape of different dipeptides. . . . .	27
3.6. Comparison: Free energy plots alanine dipeptide (MC/MD). . . . .	28
3.7. Villin mutant 2F4K. . . . .	29
3.8. Structure comparison: 1VII and 2F4K. . . . .	30
3.9. Chemical structure norleucine. . . . .	30
3.10. 2F4K q-plot and free energy. . . . .	31
3.11. 2F4K RMSD with snapshots. . . . .	31
3.12. WW domain 2F21. . . . .	32
3.13. 2F21 q-plot and free energy. . . . .	32

3.14. 2F21 rmsd with snapshots. . . . .	33
3.15. HFEs - GBNP2. . . . .	37
3.16. HFEs of molecules with nitrogen atoms - GBNP3. . . . .	38
4.1. Dielectric slabs of an implicit membrane model. . . . .	43
4.2. Dielectric Slabs in the SLIM Model. . . . .	44
4.3. Comparison: GB/PB 1 Ion. . . . .	47
4.4. Comparison: GB/PB Magainin. . . . .	48
4.5. Comparison: GB/PB 2 Ions. . . . .	49
4.6. Melittin: Kink Angle Definition. . . . .	50
4.7. Melittin: Starting Conformations. . . . .	51
4.8. Melittin: Histogram and End Conformation. . . . .	52
4.9. Melittin: Snapshots of Melittin Kinks. . . . .	53
4.10. Melittin: Histograms Energy Contributions. . . . .	54
4.11. M2 Protein - Transmembrane Domain. . . . .	55
4.12. M2 Protein - Starting Conformations. . . . .	56
4.13. M2 Protein: Kink Angle Definition. . . . .	57
4.14. M2 Protein: Histograms Minimum Kink Angle. . . . .	57
4.15. M2 Protein: Histograms Standard Deviation Kink Angle. . . . .	58
4.16. M2 Protein: Phi-Psi-Plot . . . . .	59
4.17. M2 Protein: Tilt Angles. . . . .	60
4.18. Glycophorin A Dimer: Transmembrane Domain. . . . .	62
4.19. Glycophorin A: Tilt Angles. . . . .	63
4.20. Glycophorin A: Crossing Angle. . . . .	63
5.1. BLB: Schematic Setting. . . . .	66
5.2. BLB: Experimental Setup. . . . .	67
5.3. BLB: Lipids - DiphPC and DiphPG. . . . .	68
5.4. Antimicrobial Peptides: Models for Membrane Permeation. . . . .	70

5.5. Gramicidin S: Reference Measurement. . . . .	72
5.6. Gramicidin S: Conductivity Measurement. . . . .	73
5.7. Gramicidin A: Reference Measurement. . . . .	74
5.8. Gramicidin A: Conductivity Measurement. . . . .	75
5.9. Gramicidin A: Number of Pores. . . . .	75
5.10. Gold Nanoparticles: Ligands - TPPMS and TPPTS. . . . .	76
5.11. Gold Nanoparticles: Reference Measurement. . . . .	78
5.12. Gold Nanoparticles: Conductivity Measurement Au1.4MS. . . . .	79
5.13. Gold Nanoparticles: Conductivity Measurement Au4.7MS. . . . .	79
5.14. Gold Nanoparticles: Conductivity Measurement Au10.7MS. . . . .	80
5.15. Gold Nanoparticles: Conductivity Measurement Au12MS. . . . .	80
5.16. Gold Nanoparticles: Conductivity Measurement Au15MS. . . . .	81
5.17. Gold Nanoparticles: Conductivity Measurement Au4.7TS. . . . .	82
5.18. Gold Nanoparticles: Conductivity Measurement Au10.5TS. . . . .	82
5.19. Gold Nanoparticles: Selectivity Measurement Au15MS. . . . .	83
5.20. Gold Nanoparticles: Number of Ligands. . . . .	86
6.1. Ventricular Action Potential and Electrocardiogram . . . . .	89
6.2. Gold Nanoparticles Input. . . . .	91
6.3. hERG Channel Input. . . . .	92
6.4. Electrostatic Potential hERG, pH=7.4 . . . . .	92
6.5. Electrostatic Potential hERG, pH=6.7 . . . . .	93
6.6. Simulation Snapshots hERG/Au1.4MS Docking. . . . .	94



# Bibliography

- [1] Martin Brieg, Julia Setzler, and Wolfgang Wenzel. Small molecule hydration free energies: Closing the gap between explicit solvent and implicit generalized born based solvent models. submitted.
- [2] Julia Setzler, Carolin Seith, Martin Brieg, and Wolfgang Wenzel. Slim: An improved generalized born implicit membrane. in press.
- [3] Annika Leifert, Yu Pan, Anne Kinkeldey, Frank Schiefer, Julia Setzler, Olaf Scheel, Hera Lichtenbeld, Günter Schmid, Wolfgang Wenzel, Willi Jahnen-Dechent, and Ulrich Simon. Differential hERG ion channel activity of ultrasmall gold nanoparticles. *PNAS*, 110(20):8004–8009, May 2013.
- [4] Hartmut Michel. Crystallization of membrane proteins. *Trends in Biochemical Sciences*, 8(2): 56–59, February 1983.
- [5] Carl-Ivar Brändén and John Tooze. *Introduction to protein structure*. Garland, New York, 2. edition, 1999.
- [6] Bruce Alberts, Julian Lewis, and Dennis Bray. *Molecular biology of the cell*, 2000.
- [7] Christian B Anfinsen. Principles that Govern the Folding of Protein Chains. *Science*, 181(4096): 223–230, 1973.
- [8] H.M. Berman, J. Westbrook, Z. Feng, G. Gilliland, T.N. Bhat, H. Weissig, I.N. Shindyalov, and P.E. Bourne. The Protein Data Bank. *Nucleic Acids Research*, 28:235–242, 2000. URL [www.pdb.org](http://www.pdb.org).
- [9] F. Sanger. The terminal peptides of insulin. *Biochem J*, 45(5):563–574, 1949.

- [10] G.N. Ramachandran, C. Ramakrishnan, and V. Sasisekharan. Stereochemistry of polypeptide chain configurations. *Journal of Molecular Biology*, 7(1):95–99, July 1963.
- [11] Linus Pauling and Robert B Corey. The structure of synthetic polypeptides. *Proceedings of the National Academy of Sciences of the United States*, 37(5):241–250, 1951.
- [12] L Pauling and RB Corey. The structure of proteins: two hydrogen-bonded helical configurations of the polypeptide chain. *Proceedings of the National Academy of Sciences of the United States*, 37(4):205–211, 1951.
- [13] Linus Pauling and Robert Corey. The structure of hair, muscle, and related proteins. *Proceedings of the National Academy of Sciences of the United States*, 37(5):261–271, 1951.
- [14] Linus Pauling and Robert B Corey. The structure of fibrous proteins of the collagen- gelatin group. *Proceedings of the National Academy of Sciences of the United States*, 37(5):272–281, 1951.
- [15] Linus Pauling and Robert Corey. Atomic coordinates and structure factors for two helical configurations of polypeptide chains. *Proceedings of the National Academy of Sciences of the United States*, 37(5):235–240, 1951.
- [16] Linus; Robert Corey Pauling. Configurations of Polypeptide Chains with favored orientations around single bonds: two new pleated sheets. 37(11):729–740, 1951.
- [17] Linus Pauling and Robert Corey. The pleated sheet, a new layer configuration of polypeptide chains. *Proceedings of the National Academy of Sciences of the United States*, 37(5):251–256, 1951.
- [18] S T Walsh, H Cheng, J W Bryson, H Roder, and W F DeGrado. Solution structure and dynamics of a de novo designed three-helix bundle protein. *Proc. Natl. Acad. Sci. U.S.A.*, 96(10):5486 –5491, May 1999.
- [19] Marcus Jäger, Yan Zhang, Jan Bieschke, Houbi Nguyen, Maria Dendle, Marianne E. Bowman,

- 
- Joseph P. Noel, Martin Gruebele, and Jeffery W. Kelly. Structure-function-folding relationship in a WW domain. *PNAS*, 103(28):10648–10653, July 2006.
- [20] R Rodriguez, G China, N Lopez, T Pons, and G Vriend. Homology modeling, model and software evaluation: three related resources. *Bioinformatics*, 14(6):523–528, 1998.
- [21] HC Watson. The Stereochemistry of the protein myoglobin. *Progress in stereochemistry*, 4:299, 1969.
- [22] M.F. Perutz, G. Fermi, C. Poyart, J. Pagnier, and J. Kister. A novel allosteric mechanism in haemoglobin: Structure of bovine deoxyhaemoglobin, absence of specific chloride-binding sites and origin of the chloride-linked bohr effect in bovine and human haemoglobin. *Journal of Molecular Biology*, 233(3):536–545, October 1993.
- [23] Cyrus Levinthal. How to Fold Graciously. In J T P DeBrunner and E Munck, editors, *Mossbauer Spectroscopy in Biological Systems Proceedings of a meeting held at Allerton House*, pages 22–24. University of Illinois Press, 1969.
- [24] J. N. Onuchic, P. G. Wolynes, Z. Luthey-Schulten, and N. D. Socci. Toward an outline of the topography of a realistic protein-folding funnel. *PNAS*, 92(8):3626–3630, April 1995. PMID: 7724609.
- [25] Ken A. Dill and Hue Sun Chan. From levinthal to pathways to funnels. *Nat Struct Mol Biol*, 4(1):10–19, January 1997.
- [26] Alan R Fersht. Nucleation mechanisms in protein folding. *Current Opinion in Structural Biology*, 7(1):3–9, February 1997.
- [27] O.B. Ptitsyn. Stages in the mechanism of self-organization of protein molecules. *Dokl Akad Nauk SSSR*, 210(5):1213–1215, June 1973. PMID: 4721708.
- [28] B. Robson and R.H. Pain. Analysis of the code relating sequence to conformation in proteins: Possible implications for the mechanism of formation of helical regions. *Journal of Molecular Biology*, 58(1):237–257, May 1971.
-

- [29] Donald B. Wetlaufer. Nucleation, rapid folding, and globular intrachain regions in proteins. *PNAS*, 70(3):697–701, March 1973. PMID: 4351801.
- [30] Peter S. Kim and Robert L. Baldwin. Specific intermediates in the folding reactions of small proteins and the mechanism of protein folding. 51(1):459–489, 1982. PMID: 6287919.
- [31] L Stryer, JM Berg, and JL Tymoczko. *Biochemistry*. W.H. Freeman and Company, New York, 5th edition, 2002. ISBN 0-7167-3051-0.
- [32] G Guidotti. Membrane proteins. 41(1):731–752, 1972. PMID: 4263713.
- [33] B Alberts, A Johnson, and J Lewis. Biochemistry. In *Molecular Biology of the Cell*. New York, 4th edition, 2002.
- [34] Tom Waigh. *Applied Biophysics: A Molecular Approach for Physical Scientists*. John Wiley & Sons, September 2007. ISBN 9780470513163.
- [35] Harvey Lodish, Arnold Berk, S. Lawrence Zipursky, Paul Matsudaira, David Baltimore, and James Darnell. Biomembranes: Structural organization and basic functions, 2000.
- [36] Robert EW Hancock. Peptide antibiotics. *The Lancet*, 349(9049):418 –422, February 1997.
- [37] Robert E.W Hancock and Gill Diamond. The role of cationic antimicrobial peptides in innate host defences. *Trends in Microbiology*, 8(9):402 –410, September 2000.
- [38] Guy G. Dodson, David P. Lane, and Chandra S. Verma. Molecular simulations of protein dynamics: new windows on mechanisms in biology. *EMBO Rep*, 9(2):144 –150, February 2008.
- [39] David E. Shaw, Paul Maragakis, Kresten Lindorff-Larsen, Stefano Piana, Ron O. Dror, Michael P. Eastwood, Joseph A. Bank, John M. Jumper, John K. Salmon, Yibing Shan, and Willy Wriggers. Atomic-level characterization of the structural dynamics of proteins. *Science*, 330(6002):341 –346, October 2010.
- [40] Neil P. King, William Sheffler, Michael R. Sawaya, Breanna S. Vollmar, John P. Sumida, Ingemar André, Tamir Gonen, Todd O. Yeates, and David Baker. Computational design of self-assembling protein nanomaterials with atomic level accuracy. *Science*, 336(6085):1171 –1174, June 2012.

- 
- [41] Ron O. Dror, Robert M. Dirks, J.P. Grossman, Huafeng Xu, and David E. Shaw. Biomolecular simulation: A computational microscope for molecular biology. 41(1):429–452, 2012.
- [42] Berk Hess, Carsten Kutzner, David van der Spoel, and Erik Lindahl. GROMACS 4: Algorithms for highly efficient, load-balanced, and scalable molecular simulation. *J. Chem. Theory Comput.*, 4(3):435–447, March 2008.
- [43] David A. Case, Thomas E. Cheatham, Tom Darden, Holger Gohlke, Ray Luo, Kenneth M. Merz, Alexey Onufriev, Carlos Simmerling, Bing Wang, and Robert J. Woods. The amber biomolecular simulation programs. 26(16):1668–1688, 2005.
- [44] B. R. Brooks, C. L. Brooks, A. D. Mackerell, L. Nilsson, R. J. Petrella, B. Roux, Y. Won, G. Archontis, C. Bartels, S. Boresch, A. Caffisch, L. Caves, Q. Cui, A. R. Dinner, M. Feig, S. Fischer, J. Gao, M. Hodoscek, W. Im, K. Kuczera, T. Lazaridis, J. Ma, V. Ovchinnikov, E. Paci, R. W. Pastor, C. B. Post, J. Z. Pu, M. Schaefer, B. Tidor, R. M. Venable, H. L. Woodcock, X. Wu, W. Yang, D. M. York, and M. Karplus. CHARMM: the biomolecular simulation program. 30(10):1545–1614, 2009.
- [45] Loup Verlet. Computer "Experiments" on classical fluids. i. thermodynamical properties of lennard-jones molecules. *Phys. Rev.*, 159(1):98–103, July 1967.
- [46] R.O. Dror, M.O. Jensen, and D.E. Shaw. Elucidating membrane protein function through long-timescale molecular dynamics simulation. In *Annual International Conference of the IEEE Engineering in Medicine and Biology Society, 2009. EMBC 2009*, pages 2340–2342, 2009.
- [47] Fatemeh Khalili-Araghi, James Gumbart, Po-Chao Wen, Marcos Sotomayor, Emad Tajkhorshid, and Klaus Schulten. Molecular dynamics simulations of membrane channels and transporters. *Current Opinion in Structural Biology*, 19(2):128–137, April 2009.
- [48] Phillip J. Stansfeld and Mark S.P. Sansom. Molecular simulation approaches to membrane proteins. *Structure*, 19(11):1562–1572, November 2011.
- [49] Morten Jensen, Vishwanath Jogini, David W. Borhani, Abba E. Leffler, Ron O. Dror, and
-

- David E. Shaw. Mechanism of voltage gating in potassium channels. *Science*, 336(6078):229–233, April 2012.
- [50] Yibing Shan, Anton Arkhipov, Eric T. Kim, Albert C. Pan, and David E. Shaw. Transitions to catalytically inactive conformations in EGFR kinase. *PNAS*, 110(18):7270–7275, April 2013.
- [51] Anton Arkhipov, Yibing Shan, Rahul Das, Nicholas F. Endres, Michael P. Eastwood, David E. Wemmer, John Kuriyan, and David E. Shaw. Architecture and membrane interactions of the EGF receptor. *Cell*, 152(3):557–569, January 2013.
- [52] Lipid membranes. URL [http://www.mmk.su.se/~sasha/Lipid\\_membranes.html](http://www.mmk.su.se/~sasha/Lipid_membranes.html).
- [53] Nicholas Metropolis, Arianna W. Rosenbluth, Marshall N. Rosenbluth, Augusta H. Teller, and Edward Teller. Equation of state calculations by fast computing machines. 21(6):1087–1092, June 1953.
- [54] T. Strunk, M. Wolf, M. Brieg, K. Klenin, A. Biewer, F. Tristram, M. Ernst, P. J. Kleine, N. Heilmann, I. Kondov, and W. Wenzel. SIMONA 1.0: An efficient and versatile framework for stochastic simulations of molecular and nanoscale systems. 2012.
- [55] T. Herges and W. Wenzel. An all-atom force field for tertiary structure prediction of helical proteins. *Biophysical Journal*, 87(5):3100–3109, November 2004.
- [56] Abhinav Verma and Wolfgang Wenzel. A free-energy approach for all-atom protein simulation. 96(9):3483–3494, May 2009.
- [57] Bernhard Fischer, Kaori Fukuzawa, and Wolfgang Wenzel. Receptor-specific scoring functions derived from quantum chemical models improve affinity estimates for in-silico drug discovery. 70(4):1264–1273, 2008.
- [58] Viktor Hornak, Robert Abel, Asim Okur, Bentley Strockbine, Adrian Roitberg, and Carlos Simmerling. Comparison of multiple amber force fields and development of improved protein backbone parameters. 65(3):712–725, 2006.

- [59] Robert B. Best and Gerhard Hummer. Optimized molecular dynamics force fields applied to the Helix-Coil transition of polypeptides. *J. Phys. Chem. B*, 113(26):9004–9015, July 2009.
- [60] Kresten Lindorff-Larsen, Stefano Piana, Kim Palmo, Paul Maragakis, John L Klepeis, Ron O Dror, and David E Shaw. Improved side-chain torsion potentials for the amber ff99SB protein force field. *Proteins*, 78(8):1950–1958, June 2010.
- [61] Pawel Grochowski and Joanna Trylska. Continuum molecular electrostatics, salt effects, and counterion binding-A review of the Poisson-Boltzmann theory and its modifications. 89(2):93–113, 2008.
- [62] W. C. Still, A. Tempczyk, R. C. Hawley, and T. Hendrickson. Semianalytical treatment of solvation for molecular mechanics and dynamics. 112(16):6127–6129, 1990.
- [63] Martin Brieg and Wolfgang Wenzel. PowerBorn: a Barnes-Hut tree implementation for accurate and efficient born radii computation. *J. Chem. Theory Comput.*, 9(3):1489–1498, March 2013.
- [64] Jianhan Chen and Charles L. Brooks Iii. Implicit modeling of nonpolar solvation for simulating protein folding and conformational transitions. *Phys. Chem. Chem. Phys.*, 10(4):471–481, January 2008.
- [65] David Eisenberg and Andrew D. McLachlan. Solvation energy in protein folding and binding. *Nature*, 319(6050):199–203, January 1986.
- [66] T. Ooi, M. Oobatake, G. Némethy, and H. A. Scheraga. Accessible surface areas as a measure of the thermodynamic parameters of hydration of peptides. *PNAS*, 84(10):3086–3090, May 1987.
- [67] Martin Zacharias. Continuum solvent modeling of nonpolar solvation: Improvement by separating surface area dependent cavity and dispersion contributions. *J. Phys. Chem. A*, 107(16):3000–3004, April 2003.
- [68] Ronald M. Levy, Linda Y. Zhang, Emilio Gallicchio, and Anthony K. Felts. On the nonpolar hydration free energy of proteins: Surface area and continuum solvent models for the Solute-Solvent interaction energy. *J. Am. Chem. Soc.*, 125(31):9523–9530, August 2003.

- [69] Robert C. Rizzo, Tiba Aynechi, David A. Case, and Irwin D. Kuntz. Estimation of absolute free energies of hydration using continuum methods: Accuracy of partial charge models and optimization of nonpolar contributions. *J. Chem. Theory Comput.*, 2(1):128–139, January 2006.
- [70] Jason A. Wagoner and Nathan A. Baker. Assessing implicit models for nonpolar mean solvation forces: The importance of dispersion and volume terms. *PNAS*, 103(22):8331–8336, May 2006.
- [71] Devleena Shivakumar, Yuqing Deng, and Benoît Roux. Computations of absolute solvation free energies of small molecules using explicit and implicit solvent model. *J. Chem. Theory Comput.*, 5(4):919–930, April 2009.
- [72] Jennifer L. Knight and Charles L. Brooks. Surveying implicit solvent models for estimating small molecule absolute hydration free energies. 32(13):2909–2923, 2011.
- [73] Doree Sitkoff, Kim A. Sharp, and Barry Honig. Accurate calculation of hydration free energies using macroscopic solvent models. *J. Phys. Chem.*, 98(7):1978–1988, February 1994.
- [74] H.J.C. Berendsen, D. van der Spoel, and R. van Drunen. GROMACS: a message-passing parallel molecular dynamics implementation. *Computer Physics Communications*, 91(1-3):43–56, September 1995.
- [75] Elmar Krieger and Gert Vriend. Models@Home: distributed computing in bioinformatics using a screensaver based approach. *Bioinformatics*, 18(2):315–318, February 2002.
- [76] Reinhart Ahlrichs, Michael Bär, Marco Häser, Hans Horn, and Christoph Kölmel. Electronic structure calculations on workstation computers: The program system turbomole. *Chemical Physics Letters*, 162(3):165–169, October 1989.
- [77] John D. Hunter. Matplotlib: A 2D graphics environment. 9(3):90–95, 2007.
- [78] J. Vymetal and J. Vondrasek. The DF-LCCSD (t0) correction of the [phi]/[psi] force field dihedral parameters significantly influences the free energy profile of the alanine dipeptide. 2011.
- [79] Michael Feig. Is alanine dipeptide a good model for representing the torsional preferences of protein backbones? 4(9):1555–1564, September 2008.

- [80] K. Lindorff-Larsen, S. Piana, R. O. Dror, and D. E. Shaw. How fast-folding proteins fold. 334 (6055):517–520, October 2011.
- [81] Jan Kubelka, Thang K. Chiu, David R. Davies, William A. Eaton, and James Hofrichter. Sub-microsecond protein folding. *Journal of Molecular Biology*, 359(3):546–553, June 2006.
- [82] C. James McKnight, Paul T. Matsudaira, and Peter S. Kim. NMR structure of the 35-residue villin headpiece subdomain. 4(3):180–184, March 1997.
- [83] Nana Heilmann. Simulation kleiner Proteine mittels einer Monte-Carlo Methode, 2013.
- [84] W. Kabsch. A solution for the best rotation to relate two sets of vectors. 32(5):922–923, September 1976.
- [85] Samuel S. Cho, Yaakov Levy, and Peter G. Wolynes. P versus q: Structural reaction coordinates capture protein folding on smooth landscapes. *PNAS*, 103(3):586–591, January 2006.
- [86] Jeffrey K. Noel, Paul C. Whitford, and José N. Onuchic. The shadow map: A general contact definition for capturing the dynamics of biomolecular folding and function. 116(29):8692–8702, July 2012.
- [87] Stefano Piana, Kresten Lindorff-Larsen, and David E. Shaw. Atomic-level description of ubiquitin folding. *PNAS*, 110(15):5915–5920, April 2013.
- [88] Ulrich H.E. Hansmann. Parallel tempering algorithm for conformational studies of biological molecules. *Chemical Physics Letters*, 281(1-3):140–150, December 1997.
- [89] William L. Jorgensen. The many roles of computation in drug discovery. *Science*, 303(5665):1813–1818, March 2004.
- [90] David L. Mobley and Ken A. Dill. Binding of small-molecule ligands to proteins: "What you see" is not always "What you get". *Structure*, 17(4):489–498, April 2009.
- [91] Michael K. Gilson and Huan-Xiang Zhou. Calculation of protein-ligand binding affinities\*. 36 (1):21–42, 2007.

- [92] David L. Mobley, Ken A. Dill, and John D. Chodera. Treating entropy and conformational changes in implicit solvent simulations of small molecules. *J. Phys. Chem. B*, 112(3):938–946, January 2008.
- [93] B. Roux and T. Simonson. Implicit solvent models. *Biophys. Chem.*, 78(1-2):1–20, April 1999.
- [94] Michael S. Lee, Freddie R. Salsbury, and Charles L. Brooks. Novel generalized born methods. 116(24):10606, June 2002.
- [95] Christopher J. Fennell, Charlie Kehoe, and Ken A. Dill. Oil/Water transfer is partly driven by molecular shape, not just size. *J. Am. Chem. Soc.*, 132(1):234–240, January 2010.
- [96] Feng Dong, Jason A. Wagoner, and Nathan A. Baker. Assessing the performance of implicit solvation models at a nucleic acid surface. 10(32):4889–4902, 2008.
- [97] Jianhan Chen, Charles L Brooks III, and Jana Khandogin. Recent advances in implicit solvent-based methods for biomolecular simulations. *Current Opinion in Structural Biology*, 18(2):140–148, April 2008.
- [98] Junmei Wang, Romain M. Wolf, James W. Caldwell, Peter A. Kollman, and David A. Case. Development and testing of a general amber force field. 25(9):1157–1174, 2004.
- [99] Junmei Wang, Wei Wang, Peter A. Kollman, and David A. Case. Automatic atom type and bond type perception in molecular mechanical calculations. 25(2):247–260, October 2006.
- [100] Araz Jakalian, Bruce L. Bush, David B. Jack, and Christopher I. Bayly. Fast, efficient generation of high-quality atomic charges. AM1-BCC model: I. method. 21(2):132–146, 2000.
- [101] Araz Jakalian, David B Jack, and Christopher I Bayly. Fast, efficient generation of high-quality atomic charges. AM1-BCC model: II. parameterization and validation. 23(16):1623–1641, December 2002.
- [102] Ivan Kondov and Rüdiger Berlich. Protein structure prediction using particle swarm optimization and a distributed parallel approach. In *Proceedings of the 3rd workshop on Biologically inspired algorithms for distributed systems*, BADS '11, pages 35–42, New York, NY, USA, 2011. ACM.

- [103] M. J. D. Powell. An efficient method for finding the minimum of a function of several variables without calculating derivatives. *The Computer Journal*, 7(2):155–162, January 1964.
- [104] David L. Mobley, Christopher I. Bayly, Matthew D. Cooper, Michael R. Shirts, and Ken A. Dill. Small molecule hydration free energies in explicit solvent: An extensive test of fixed-charge atomistic simulations. 5(2):350–358, 2009.
- [105] Jana Chocholousová and Michael Feig. Balancing an accurate representation of the molecular surface in generalized born formalisms with integrator stability in molecular dynamics simulations. 27(6):719–729, April 2006.
- [106] Michael R. Shirts and John D. Chodera. Statistically optimal analysis of samples from multiple equilibrium states. 129(12), September 2008.
- [107] Wendell M. Latimer, Kenneth S. Pitzer, and Cyril M. Slansky. The free energy of hydration of gaseous ions, and the absolute potential of the normal calomel electrode. 7(2):108–111, February 1939.
- [108] R. M. Lynden-Bell and J. C. Rasaiah. From hydrophobic to hydrophilic behaviour: A simulation study of solvation entropy and free energy of simple solutes. 107:1981, 1997.
- [109] David L. Mobley, Alan E. Barber, Christopher J. Fennell, and Ken A. Dill. Charge asymmetries in hydration of polar solutes. 112(8):2405–2414, February 2008.
- [110] Velin Z. Spassov, Lisa Yan, and Sándor Szalma. Introducing an implicit membrane in generalized Born/Solvent accessibility continuum solvent models. *J. Phys. Chem. B*, 106(34):8726–8738, August 2002.
- [111] Wonpil Im, Michael Feig, and Charles L. Brooks. An implicit membrane generalized born theory for the study of structure, stability, and interactions of membrane proteins. *Biophys J*, 85(5):2900–2918, November 2003.
- [112] Martin B. Ulmschneider, Jakob P. Ulmschneider, Mark S. P. Sansom, and Alfredo Di Nola.

- A generalized born implicit-membrane representation compared to experimental insertion free energies. *Biophys J*, 92(7):2338 –2349, April 2007.
- [113] Seiichiro Tanizaki and Michael Feig. A generalized born formalism for heterogeneous dielectric environments: application to the implicit modeling of biological membranes. *J Chem Phys*, 122(12):124706, March 2005.
- [114] Hugh Nymeyer and Huan-Xiang Zhou. A method to determine dielectric constants in nonhomogeneous systems: Application to biological membranes. *Biophysical Journal*, 94(4):1185 –1193, February 2008.
- [115] Wonpil Im, Dmitrii Beglov, and Benoît Roux. Continuum solvation model: Computation of electrostatic forces from numerical solutions to the poisson-boltzmann equation. *Computer Physics Communications*, 111(1-3):59 –75, June 1998.
- [116] Sunhwan Jo, Miklos Vargyas, Judit Vasko-Szedlar, Benoît Roux, and Wonpil Im. PBEQ-Solver for online visualization of electrostatic potential of biomolecules. *Nucl. Acids Res.*, 36(suppl 2):W270 –W275, January 2008.
- [117] J Gesell, M Zasloff, and S J Opella. Two-dimensional  $^1\text{H}$  NMR experiments show that the 23-residue magainin antibiotic peptide is an alpha-helix in dodecylphosphocholine micelles, sodium dodecylsulfate micelles, and trifluoroethanol/water solution. *J. Biomol. NMR*, 9(2):127 –135, February 1997.
- [118] Simon Bernéche, Mafalda Nina, and Benoît Roux. Molecular dynamics simulation of melittin in a dimyristoylphosphatidylcholine bilayer membrane. 75(4):1603 –1618, October 1998.
- [119] Michal Bachar and Oren M. Becker. Melittin at a membrane/water interface: Effects on water orientation and water penetration. 111(18):8672 –8685, November 1999.
- [120] M Bachar and O M Becker. Protein-induced membrane disorder: a molecular dynamics study of melittin in a dipalmitoylphosphatidylcholine bilayer. *Biophys. J.*, 78(3):1359 –1375, March 2000.

- [121] D. Anderson, T. C. Terwilliger, W. Wickner, and D. Eisenberg. Melittin forms crystals which are suitable for high resolution x-ray structural analysis and which reveal a molecular 2-fold axis of symmetry. *J. Biol. Chem.*, 255(6):2578 –2582, March 1980.
- [122] T. C. Terwilliger and D. Eisenberg. The structure of melittin. i. structure determination and partial refinement. *J. Biol. Chem.*, 257(11):6010 –6015, October 1982.
- [123] T C Terwilliger and D Eisenberg. The structure of melittin. II. interpretation of the structure. *J. Biol. Chem.*, 257(11):6016 –6022, June 1982.
- [124] G von Heijne. Proline kinks in transmembrane alpha-helices. *J. Mol. Biol.*, 218(3):499 –503, April 1991.
- [125] P Y Chou and G D Fasman. Prediction of the secondary structure of proteins from their amino acid sequence. *Adv. Enzymol. Relat. Areas Mol. Biol.*, 47:45 –148, 1978.
- [126] H Vogel and F Jahnig. The structure of melittin in membranes. *Biophys J*, 50(4):573 –582, October 1986.
- [127] A. Pastore, T. S. Harvey, C. E. Dempsey, and I. D. Campbell. The dynamic properties of melittin in solution. *Eur Biophys J*, 16(6):363 –367, February 1989.
- [128] C E Dempsey. The actions of melittin on membranes. *Biochim. Biophys. Acta*, 1031(2):143 –161, May 1990.
- [129] K Hristova, C E Dempsey, and S H White. Structure, location, and lipid perturbations of melittin at the membrane interface. *Biophys J*, 80(2):801 –811, February 2001.
- [130] J. P. Bradshaw, C. E. Dempsey, and A. Watts. A combined x-ray and neutron diffraction study of selectively deuterated melittin in phospholipid bilayers: effect of pH. 11(2):79 –86, January 1994.
- [131] Horst Vogel. Comparison of the conformation and orientation of alamethicin and melittin in lipid membranes. *Biochemistry*, 26(14):4562 –4572, July 1987.

- [132] E Habermann and H Kowallek. Modifications of amino groups and tryptophan in melittin as an aid to recognition of structure-activity relationships. *Hoppe-Seyler's Z. Physiol. Chem.*, 351(7): 884 –890, July 1970.
- [133] John F. Nagle and Stephanie Tristram-Nagle. Structure of lipid bilayers. *Biochimica et Biophysica Acta (BBA) - Reviews on Biomembranes*, 1469(3):159 –195, November 2000.
- [134] Carolin Seith. Entwicklung eines impliziten Membranmodells für biomolekulare Simulationen, 2013.
- [135] R Bazzo, M J Tappin, A Pastore, T S Harvey, J A Carver, and I D Campbell. The structure of melittin. a  $^1\text{H}$ -NMR study in methanol. *Eur. J. Biochem.*, 173(1):139 –146, April 1988.
- [136] A Naito, T Nagao, K Norisada, T Mizuno, S Tuzi, and H Saitó. Conformation and dynamics of melittin bound to magnetically oriented lipid bilayers by solid-state  $(^{31}\text{P})$  and  $(^{13}\text{C})$  NMR spectroscopy. *Biophys. J.*, 78(5):2405 –2417, May 2000.
- [137] Isaiah T Arkin. Structural aspects of oligomerization taking place between the transmembrane alpha-helices of bitopic membrane proteins. *Biochim. Biophys. Acta*, 1565(2):347 –363, October 2002.
- [138] L J Holsinger, D Nichani, L H Pinto, and R A Lamb. Influenza a virus m2 ion channel protein: a structure-function analysis. *J Virol*, 68(3):1551 –1563, March 1994.
- [139] Leslie J. Holsinger and Robert Alams. Influenza virus m2 integral membrane protein is a homotetramer stabilized by formation of disulfide bonds. *Virology*, 183(1):32 –43, July 1991.
- [140] L H Pinto, L J Holsinger, and R A Lamb. Influenza virus m2 protein has ion channel activity. *Cell*, 69(3):517 –528, May 1992.
- [141] J Wang, S Kim, F Kovacs, and T A Cross. Structure of the transmembrane region of the m2 protein h(+) channel. *Protein Sci.*, 10(11):2241 –2250, November 2001.
- [142] O.G. Mouritsen and M. Bloom. Mattress model of lipid-protein interactions in membranes. *Biophysical Journal*, 46(2):141 –153, August 1984.

- [143] F.A. Kovacs, Jeffrey K. Denny, Z. Song, J.R. Quine, and T.A. Cross. Helix tilt of the m2 transmembrane peptide from influenza a virus: an intrinsic property. *Journal of Molecular Biology*, 295(1):117–125, January 2000.
- [144] J. L. Popot and D. M. Engelman. Helical membrane protein folding, stability, and evolution. 69 (1):881–922, 2000.
- [145] K R MacKenzie, J H Prestegard, and D M Engelman. A transmembrane helix dimer: structure and implications. *Science*, 276(5309):131–133, April 1997.
- [146] Steven O. Smith, Roy Jonas, Mark Braiman, and Barbara J. Bormann. Structure and orientation of the transmembrane domain of glycophorin a in lipid bilayers. *Biochemistry*, 33(20):6334–6341, May 1994.
- [147] Steven O. Smith, David Song, Srinivasan Shekar, Michel Groesbeek, Martine Ziliox, and Saburo Aimoto. Structure of the transmembrane dimer interface of glycophorin a in membrane bilayers. *Biochemistry*, 40(22):6553–6558, June 2001.
- [148] H I Petrache, A Grossfield, K R MacKenzie, D M Engelman, and T B Woolf. Modulation of glycophorin a transmembrane helix interactions by lipid bilayers: molecular dynamics calculations. *J. Mol. Biol.*, 302(3):727–746, September 2000.
- [149] Paul Mueller, Donald O. Rudin, H. Ti Tien, and William C. Wescott. Reconstitution of cell membrane structure in vitro and its transformation into an excitable system. *Nature*, 194(4832):979–980, June 1962.
- [150] H T Tien. Thickness and molecular organization of bimolecular lipid membranes in aqueous media. *J. Mol. Biol.*, 16(2):577–580, April 1966.
- [151] H. T. Tien, S. Carbone, and E. A. Dawidowicz. Formation of "Black" lipid membranes by oxidation products of cholesterol. *Nature*, 212(5063):718–719, November 1966.
- [152] Renate Naumann, Alfred Jonczyk, Ralf Kopp, Jan van Esch, Helmut Ringsdorf, Wolfgang Knoll,

- and Peter Graeber. Incorporation of membrane proteins in solid-supported lipid layers. 34(18): 2056–2058, 1995.
- [153] I. G. Denisov, Y. V. Grinkova, A. A. Lazarides, and S. G. Sligar. Directed self-assembly of monodisperse phospholipid bilayer nanodiscs with controlled size. *J. Am. Chem. Soc.*, 126(11): 3477–3487, March 2004.
- [154] Annela M. Seddon, Paul Curnow, and Paula J. Booth. Membrane proteins, lipids and detergents: not just a soap opera. *Biochimica et Biophysica Acta (BBA) - Biomembranes*, 1666(1-2):105–117, November 2004.
- [155] Silvia Cavagnero, H. Jane Dyson, and Peter E. Wright. Improved low pH bicelle system for orienting macromolecules over a wide temperature range. *J Biomol NMR*, 13(4):387–391, April 1999.
- [156] Jere P. Segrest. Amphipathic helices and plasma lipoproteins: Thermodynamic and geometric considerations. *Chemistry and Physics of Lipids*, 18(1):7–22, January 1977.
- [157] Timothy H. Bayburt, Yelena V. Grinkova, and Stephen G. Sligar. Self-assembly of discoidal phospholipid bilayer nanoparticles with membrane scaffold proteins. *Nano Lett.*, 2(8):853–856, August 2002.
- [158] R Benz, K Janko, W Boos, and P Lauger. Formation of large, ion-permeable membrane channels by the matrix protein (porin) of escherichia coli. 511(3):305–319, August 1978.
- [159] R. Benz and K. Janko. Voltage-induced capacitance relaxation of lipid bilayer membranes effects of membrane composition. *Biochimica et Biophysica Acta (BBA) - Biomembranes*, 455(3):721–738, December 1976.
- [160] J.R. Elliott and D.A. Haydon. The interaction of n-octanol with black lipid bilayer membranes. *Biochimica et Biophysica Acta (BBA) - Biomembranes*, 557(1):259–263, October 1979.
- [161] R. Benz, K. Janko, and P. Laeuger. Ionic selectivity of pores formed by the matrix protein

- (porin) of *Escherichia coli*. *Biochimica et Biophysica Acta (BBA) - Biomembranes*, 551(2):238–247, March 1989.
- [162] Resistance to antibiotics. *Science*, 264(5157):360–393, April 1994.
- [163] Robert E. W. Hancock and Hans-Georg Sahl. Antimicrobial and host-defense peptides as new anti-infective therapeutic strategies. *Nat Biotech*, 24(12):1551–1557, December 2006.
- [164] Robert E.W Hancock and Robert Lehrer. Cationic peptides: a new source of antibiotics. *Trends in Biotechnology*, 16(2):82–88, February 1998.
- [165] Burkhard Bechinger. The structure, dynamics and orientation of antimicrobial peptides in membranes by multidimensional solid-state NMR spectroscopy. *Biochimica et Biophysica Acta (BBA) - Biomembranes*, 1462(1-2):157–183, December 1999.
- [166] Kim A. Brogden. Antimicrobial peptides: pore formers or metabolic inhibitors in bacteria? *Nat Rev Micro*, 3(3):238–250, March 2005.
- [167] Rollin D. Hotchkiss and René J. Dubos. Fractionation of the bactericidal agent from cultures of a soil bacillus. 132(2):791–792, 1940.
- [168] B. A. Wallace. Recent advances in the high resolution structures of bacterial channels: gramicidin a. 121(2):123–141, 1998.
- [169] S. Weinstein, B. A. Wallace, E. R. Blout, J. S. Morrow, and W. Veatch. Conformation of gramicidin a channel in phospholipid vesicles: a <sup>13</sup>C and <sup>19</sup>F nuclear magnetic resonance study. *PNAS*, 76(9):4230–4234, September 1979. PMID: 92025.
- [170] G. F. Gause and M. G. Brazhnikova. Gramicidin s and its use in the treatment of infected wounds. 154(3918):703–703, December 1944.
- [171] Leslie H. Kondejewski, Susan W. Farmer, David S. Wishart, Robert E.w. Hancock, and Robert S. Hodges. Gramicidin s is active against both gram-positive and gram-negative bacteria. 47(6):460–466, 1996.

- [172] G M Schmidt, D C Hodkin, and B M Oughton. A crystallographic study of some derivatives of gramicidin s. *Biochem. J.*, 65(4):744–750, 1957.
- [173] Yvonne Klapper. Untersuchung der Eigenschaften von Biomolekülen in Membranen und in wässriger Lösung, 2010.
- [174] Frédéric Heitz, Fatiha Kaddari, Nicole Van Mau, Jean Verducci, Hanta Raniri Sehen, and René Lazaro. Ionic pores formed by cyclic peptides. *Biochimie*, 71(1):71–76, January 1989.
- [175] Manhong Wu, Elke Maier, Roland Benz, and Robert E. W. Hancock. Mechanism of interaction of different classes of cationic antimicrobial peptides with planar bilayers and with the cytoplasmic membrane of escherichia coli. *Biochemistry*, 38(22):7235–7242, June 1999.
- [176] Md. Ashrafuzzaman, O.S. Andersen, and R.N. McElhaney. The antimicrobial peptide gramicidin s permeabilizes phospholipid bilayer membranes without forming discrete ion channels. *Biochimica et Biophysica Acta (BBA) - Biomembranes*, 1778(12):2814–2822, December 2008.
- [177] Reinhard Sarges and Bernhard Witkop. Gramicidin a. VI. the synthesis of valine- and isoleucine-gramicidin a. *J. Am. Chem. Soc.*, 87(9):2020–2027, May 1965.
- [178] Reinhard Sarges and Bernhard Witkop. Gramicidin a. v. the structure of valine- and isoleucine-gramicidin a. *J. Am. Chem. Soc.*, 87(9):2011–2020, May 1965.
- [179] Alan Finkelstein and Olaf Sparre Andersen. The gramicidin a channel: A review of its permeability characteristics with special reference to the single-file aspect of transport. *J. Membrin Biol.*, 59(3):155–171, October 1981.
- [180] S.B. Hladky and D.A. Haydon. Ion transfer across lipid membranes in the presence of gramicidin a: I. studies of the unit conductance channel. *Biochimica et Biophysica Acta (BBA) - Biomembranes*, 274(2):294–312, August 1972.
- [181] David A. Giljohann, Dwight S. Seferos, Weston L. Daniel, Matthew D. Massich, Pinal C. Patel, and Chad A. Mirkin. Gold nanoparticles for biology and medicine. 49(19):3280–3294, 2010.

- [182] Elodie Boisselier and Didier Astruc. Gold nanoparticles in nanomedicine: preparations, imaging, diagnostics, therapies and toxicity. *Chem. Soc. Rev.*, 38(6):1759–1782, May 2009.
- [183] Rachela Popovtzer, Ashish Agrawal, Nicholas A. Kotov, Aron Popovtzer, James Balter, Thomas. E. Carey, and Raoul Kopelman. Targeted gold nanoparticles enable molecular CT imaging of cancer. *Nano Lett.*, 8(12):4593–4596, December 2008. ISSN 1530-6984.
- [184] Byoungjin Kim, Gang Han, Bhushan J. Toley, Chae-kyu Kim, Vincent M. Rotello, and Neil S. Forbes. Tuning payload delivery in tumour cylindroids using gold nanoparticles. *Nat Nano*, 5(6):465–472, June 2010.
- [185] David A. Giljohann and Chad A. Mirkin. Drivers of biodiagnostic development. *Nature*, 462(7272):461–464, November 2009.
- [186] Marie-Christine Daniel and Didier Astruc. Gold nanoparticles: Assembly, supramolecular chemistry, quantum-size-related properties, and applications toward biology, catalysis, and nanotechnology. *Chem. Rev.*, 104(1):293–346, January 2004.
- [187] Pooja M. Tiwari, Komal Vig, Vida A. Dennis, and Shree R. Singh. Functionalized gold nanoparticles and their biomedical applications. 1(1):31–63, June 2011.
- [188] Yu Pan, Sabine Neuss, Annika Leifert, Monika Fischler, Fei Wen, Ulrich Simon, Guenter Schmid, Wolfgang Brandau, and Willi Jahnen-Dechent. Size-dependent cytotoxicity of gold nanoparticles. 3(11):1941–1949, 2007.
- [189] H.T. Tien. Black lipid membranes: Thickness determination and molecular organization by optical methods. *Journal of Theoretical Biology*, 16(1):97–110, July 1967.
- [190] Günter Schmid. Developments in transition metal cluster chemistry - the way to large clusters. In *Clusters*, number 62 in Structure and Bonding, pages 51–85. Springer Berlin Heidelberg, January 1985. ISBN 978-3-540-15731-1, 978-3-540-39647-5.
- [191] J. W. Warmke and B. Ganetzky. A family of potassium channel genes related to eag in drosophila and mammals. *PNAS*, 91(8):3438–3442, April 1994.

- [192] Michael C Sanguinetti, Changan Jiang, Mark E Curran, and Mark T Keating. A mechanistic link between an inherited and an acquired cardiac arrhythmia: HERG encodes the IKr potassium channel. *Cell*, 81(2):299–307, April 1995.
- [193] M C Trudeau, J W Warmke, B Ganetzky, and G A Robertson. HERG, a human inward rectifier in the voltage-gated potassium channel family. *Science*, 269(5220):92–95, July 1995.
- [194] Michael C. Sanguinetti and Martin Tristani-Firouzi. hERG potassium channels and cardiac arrhythmia. *Nature*, 440(7083):463–469, March 2006.
- [195] Mark E Curran, Igor Splawski, Katherine W Timothy, G. Michael Vincen, Eric D Green, and Mark T Keating. A molecular basis for cardiac arrhythmia: HERG mutations cause long QT syndrome. *Cell*, 80(5):795–803, March 1995.
- [196] Wilhelm Haverkamp, Günter Breithardt, A. John Camm, Michiel J. Janse, Michael R. Rosen, Charles Antzelevitch, Denis Escande, Michael Franz, Marek Malik, Arthur Moss, and Rashmi Shah. The potential for QT prolongation and pro-arrhythmia by non-anti-arrhythmic drugs: Clinical and regulatory implications report on a policy conference of the european society of cardiology. *Cardiovasc Res*, 47(2):219–233, August 2000.
- [197] Bernard Fermini, Anthony A. Fossa, Bernard Fermini, and Anthony A. Fossa. The impact of drug-induced QT interval prolongation on drug discovery and development, the impact of drug-induced QT interval prolongation on drug discovery and development. *Nat Rev Drug Discov*, 2, 2(6, 6):439, 439–447, June 2003.
- [198] Icilio Cavero and William Crumb. ICH S7B draft guideline on the non-clinical strategy for testing delayed cardiac repolarisation risk of drugs: a critical analysis. 4(3):509–530, May 2005.
- [199] Yu Pan, Annika Leifert, David Ruau, Sabine Neuss, Joerg Bornemann, Guenter Schmid, Wolfgang Brandau, Ulrich Simon, and Willi Jahnen-Dechent. Gold nanoparticles of diameter 1.4 nm trigger necrosis by oxidative stress and mitochondrial damage. 5(18):2067–2076, 2009.
- [200] J. F. Hainfeld, D. N. Slatkin, T. M. Focella, and H. M. Smilowitz. Gold nanoparticles: a new x-ray contrast agent. *Br J Radiol*, 79(939):248–253, March 2006.

- [201] R. D. Taylor, P. J. Jewsbury, and J. W. Essex. A review of protein-small molecule docking methods. *J Comput Aided Mol Des*, 16(3):151–166, March 2002.
- [202] Graham R. Smith and Michael J.E. Sternberg. Prediction of protein-protein interactions by docking methods. *Current Opinion in Structural Biology*, 12(1):28–35, February 2002.
- [203] Jonathan P. K. Doye and David J. Wales. Global minima for transition metal clusters described by Sutton-Chen potentials. *New J. Chem.*, 22(7):733–744, January 1998.
- [204] The cambridge energy landscape database. URL <http://www-wales.ch.cam.ac.uk/CCD.html>.
- [205] Schrödinger, LLC. The PyMOL molecular graphics system, version 1.3r1. August 2010.
- [206] Christian Ostermeier and Hartmut Michel. Crystallization of membrane proteins. *Current Opinion in Structural Biology*, 7(5):697–701, October 1997.
- [207] Charles R. Sanders and Frank Sönnichsen. Solution NMR of membrane proteins: practice and challenges. 44(S1):S24–S40, 2006.
- [208] Alexander Hillisch, Luis Felipe Pineda, and Rolf Hilgenfeld. Utility of homology models in the drug discovery process. *Drug Discovery Today*, 9(15):659–669, August 2004.
- [209] Claudio N. Cavasotto and Sharangdhar S. Phatak. Homology modeling in drug discovery: current trends and applications. *Drug Discovery Today*, 14(13-14):676–683, July 2009.
- [210] Stephen B. Long, Ernest B. Campbell, and Roderick MacKinnon. Crystal structure of a mammalian voltage-dependent shaker family k<sup>+</sup> channel. *Science*, 309(5736):897–903, August 2005. ISSN 0036-8075, 1095-9203.
- [211] Anna Stary, Sören J. Wacker, Lars Boukharta, Ulrich Zachariae, Yasmin Karimi-Nejad, Johan Aqvist, Gert Vriend, and Bert L. de Groot. Toward a consensus model of the hERG potassium channel. 5(3):455–467, 2010.
- [212] Nathan A. Baker, David Sept, Simpson Joseph, Michael J. Holst, and J. Andrew McCammon. Electrostatics of nanosystems: Application to microtubules and the ribosome. *PNAS*, 98(18):10037–10041, August 2001.

- [213] BW-Grid member of the german d-grid initiative, funded by the ministry for education and research (bundesministerium fuer bildung und forschung) and the ministry for science, research and arts baden-wuerttemberg (ministerium fuer wissenschaft, forschung und kunst baden-wuerttemberg). URL <http://www.bw-grid.de/das-bwgrid/>.
- [214] GIMP - the GNU image manipulation program. URL <http://www.gimp.org/>.
- [215] Grace home. URL <http://plasma-gate.weizmann.ac.il/Grace/>.
- [216] QtiPlot. URL <http://soft.proindependent.com/qtiplot.html>.
- [217] LibreOffice. URL <https://www.libreoffice.org/>.
- [218] BKChem. URL <http://bkchem.zirael.org/>.
- [219] Noel M. O'Boyle, Michael Banck, Craig A. James, Chris Morley, Tim Vandermeersch, and Geoffrey R. Hutchison. Open babel: An open chemical toolbox. 3(1):33, October 2011.
- [220] Todd J. Dolinsky, Jens E. Nielsen, J. Andrew McCammon, and Nathan A. Baker. PDB2PQR: an automated pipeline for the setup of Poisson-Boltzmann electrostatics calculations. *Nucl. Acids Res.*, 32(suppl 2):W665–W667, July 2004. PMID: 15215472.
- [221] Inkscape. draw freely. URL <http://inkscape.org/>.

# Acknowledgments

Herzlichen Dank an...

... **Prof. Dr. Wolfgang Wenzel**. Danke, dass ich deiner Arbeitsgruppe meine Doktorarbeit anfertigen durfte! Danke für die vielen neuen Ideen, Anstöße und Diskussionen, die diese Arbeit vorangetrieben haben. Danke auch für die immer währende Unterstützung bei unserer Experimentidee und die Möglichkeit verschiedene Konferenzen besuchen zu können.

... **Herrn Prof. Dr. Gerd Schön** für die freundliche Übernahme des Korreferates.

... **Herrn Professor Roland Benz**. Es war eine tolle Zeit in Ihrem Labor, in der ich viel gelernt habe. Die freundliche, lockere Atmosphäre, die vielen wissenschaftlichen Diskussionen sowie die exklusive Stadtführung und die Abendessen werden mir immer in guter Erinnerung bleiben! Ich hoffe wir sehen uns mal wieder bei einem Symposium der AG Benz'ler! Danke für alles!

... **Frau Prof. Anne Ulrich und Herrn Prof. Ulrich Simon** für die wirklich interessanten Kollaborationen!

... **Janine Broda, Annika Leifert und Evgeni B. Starikov** für die gute Zusammenarbeit.

... **Martin und Caro**, die viel mehr als nur Arbeitskollegen für mich waren! Danke für die wirklich tolle Zusammenarbeit!!

... **Yvonne**, mit der ich die Kollaboration für die Bilayer Experimente in Würzburg angestoßen habe und viel Zeit in verschiedenen Laboren, im Hotel, im Zug und im Büro verbracht habe.

... **Chrii, Ange, Kerstin, Mari, Elke und alle anderen AG Benz'ler**. Vielen vielen Dank für die tolle Zeit bei euch in Würzburg! Egal ob mit der "zickigen Membran" im Labor, informativen

Diskussionen am Bilayer, im Büro oder am Telefon, ob bei Spiele- oder Rockband Abenden,... es war eine unvergessliche Zeit! Danke dafür!!

... **Martin, Timo und Moritz**, die so viele Fehler im Programm behoben haben und immer hilfsbereit waren, wenn mal wieder was nicht funktioniert hat.

... **Priya**, die mir in den letzten Jahre die Zeit im Büro verschönert hat!

... **Aina, Benni, Sabine, Jasmin, Robert, Kerrin, Thomas, Markus, Simon, Erika, Christine und Patricia** für eine schöne Zeit am INT!

... **das Tour de Oststadt Team + die Kochgruppe :-)**. Danke auch an die gesamte AG Wenzel.

... **Martin, Caro, Timo+Marina, Moritz+Eva, Nana, Cooks und Louisa** für die vielen lustigen Aktionen und Unternehmungen abends und am Wochenende!

... **meine Korrekturleser Martin, Wolfgang, Christian und Marina**.

... **Arne, Fabio, Holger, Juli, Schuh**. Vielen Dank für die vielen lustigen Stunden im Studium, die Lerncamps und eure Freundschaft. Jetzt haben wir alle unsere Doktorarbeit geschrieben, wer hätte das vor 10 Jahren gedacht ;-)

... **Arthur, Christian, Dominik+Sabine mit Sophie+Clara, Ewa, Frank+Jasmin mit Alexa, Gabi, Hanna+Markus, Juli+Martin mit Sophie+Felix, Julia, Katja, Mareike, Marina, Matthias, Patty, Rebekka, Sanne, Sebi+Alex, Simon II., Steffi, Stephanie, Tob**. Schön, dass ihr immer für mich da seid und mir auch nicht böse seid, wenn ich es mal wieder nicht schaffe mich regelmäßig zu melden!

... **meine Familie**. Vorallem an Papa, der mich immer unterstützt und an mich glaubt! An meine Brüder Flo, Domi, Luky und Matthi, mit Ami, Sylv und Jannis! Schön, dass es euch alle gibt!! Danke auch an Mama, Omi und Opi!

... **Martin**. Du bist immer für mich da und einfach der Beste :-) Danke für alles!!!

$$x^2 + 2\left(\frac{3}{5}\sqrt[3]{x^2} - y\right)^2 - 1 = 0$$

## List of publications

1. **Setzler J.**, *Modelle und Untersuchungen der Löslichkeit von Wirkstoffkandidaten in der Medikamentenentwicklung*, (2008) (diploma thesis)
2. Tanabe T., Noda K., Miyagi S., Kurita N., Tanaka S., **Setzler J.**, Wenzel W., Starikov E. B., Cuniberti G. *Resonant neutral particle emission in collisions of electrons with protonated peptides with disulfide bonds at high energies*, Chemical Physics Letters 504, 83-87 (2011)
3. Leifert A., Pan Y., Kinkeldey A., Schiefer F., **Setzler J.**, Scheel O., Lichtenbeld H., Schmid G., Wenzel W., Jahnen-Dechent W., Simon U., *Differential hERG ion channels activity of ultrasmall gold nanoparticles*, Proceedings of the National Academy of Sciences 110, 20, 8004-8009 (2013)
4. **Setzler J.**, Seith C., Brieg M., Wenzel W. *SLIM: An Improved Generalized Born Implicit Membrane Model*, Journal of Computational Chemistry, in press
5. Brieg M., **Setzler J.**, Wenzel W. *Small Molecule Hydration Free Energies: Closing the Gap between Explicit Solvent and Implicit Generalized Born Based Solvent Models*, submitted
6. **Setzler J.**, Broda J., Leifert A, Steitz J., Benz R., Wenzel W., Simon U. *Size-Dependent Interactions between Gold Nanoparticles and Lipid Bilayer Membranes*, in preparation
7. Heilmann N., Wolf M., **Setzler J.**, Brieg M., Wenzel W. *Complete Computational Characterization of Protein Folding Equilibrium at the All Atom Level*, in preparation

## Conference contributions and invited talks

1. Schröder T, Quintilla A., Setzler J., BIRTHALAN E., Wenzel W., Bräse S. *Joint experimental and theoretical investigation of the propensity of peptoids as drug carriers*, Proceedings of the 4th WSEAS Conference on Mathematics in Biology (MABE08) (2008)
2. Setzler J., seminar talk W. Klopper, Karlsruhe 2008
3. Setzler J., Quintilla A., Klapper Y., Wenzel W., *Molecular Dynamics Simulations and Transport of Small Molecules Across Membranes*, CFN SummerSchool 2009, Bad Herrenalb

4. Setzler J., Klapper Y., Leifert A., Strunk T., Ulrich A.S., Jahnen-Dechent W., Simon U., Benz R., Wenzel W., *Joint Experimental and Theoretical Investigation of the Interaction Between Antimicrobial Peptides, Gold Nanoparticles and Membranes*, Meeting of the German Biophysical Society 2010, Bochum
5. Setzler J., Klapper Y., Leifert A., Strunk T., Ulrich A.S., Simon U., Benz R., Wenzel W., *Joint Experimental and Theoretical Investigation of the Interaction Between Antimicrobial Peptides, Gold Nanoparticles and Membranes*, *Biophys J* 100, 210a (2011)
6. Setzler J., Klapper Y., Leifert A., Strunk T., Ulrich A.S., Simon U., Benz R., Wenzel W., *Joint Experimental and Theoretical Investigations of the Interaction between Antimicrobial Peptides, Gold Nanoparticles and Membranes*, *Computer Simulation and Theory of Macromolecules* 2011, Hünfeld
7. Setzler J., *Interactions of small ligand stabilized gold nanoparticles with hERG potassium ion channels*, invited talk, *Biotechnology Symposium* 2011, Karlstadt
8. Setzler J., Brieg M., Heilmann N., Seith C., Wenzel W., *Studying protein folding with atomistic Monte Carlo simulations in implicit solvent*, Meeting of the German Biophysical Society 2012, Göttingen
9. Setzler J., Broda J., Leifert A., Simon U., Benz R., Wenzel W., *Size-Dependent Interaction Between Gold Nanoparticles and Lipid Bilayer Membranes*, *Biophys J* 104, 426a (2013)
10. Heilmann N., Setzler J., Brieg M., Strunk T., Wolf M., Seith C., Wenzel W., *Thermodynamic Characterization of Protein Folding Equilibriums at the All Atom Level*, *Biophys J* 104, 369a-370a (2013)
11. Brieg M., Setzler J., Wenzel W., *A reparametrized implicit solvent model for accurate computation of hydration free energies*, *Biophys J* 104, 507a (2013)
12. Setzler J., Brieg M., Seith C., Wenzel W., *Modeling Peptide Conformations and Insertion in an Implicit Membrane Model*, Joint Meeting of the British and German Biophysical Society, 2013, Hünfeld

13. Brieg M., Setzler J., Wenzel W., *A Reparametrized Implicit Solvent Model for Accurate Computation of Hydration Free Energies*, Joint Meeting of the British and German Biophysical Society, 2013, Hünfeld
14. Setzler J., Brieg M., Seith C., Wenzel W. *Modeling Membrane Proteins with a new Implicit Membrane Model*, Workshop on Computer Simulation and Theory of Macromolecules 2013, Hünfeld
15. Brieg M., Setzler J., Wenzel W. *A Reparametrized Implicit Solvent Model for Accurate Computation of Hydration Free Energies*, Workshop on Computer Simulation and Theory of Macromolecules 2013, Hünfeld
16. Heilmann N., Setzler J., Wolf M., Strunk T., Brieg M., Wenzel W. *Thermodynamic Characterization of Protein Folding Using Monte Carlo Methods*, Workshop on Computer Simulation and Theory of Macromolecules 2013, Hünfeld
17. Brieg M., Setzler J., Wenzel W. *Assessment of Nonpolar Term in Implicit Solvent Models to Estimate Small Molecule Hydration Free Energies*, Biophys J 106, 408a (2014)
18. Setzler J., Brieg M., Seith C., Wenzel W. *Modeling Membrane Proteins with SLIM, a new Implicit Membrane Model*, Biophys J 106, 89a (2014)
19. Heilmann N., Wolf M., Strunk T., Setzler J., Brieg M., Wenzel W. *Thermodynamic Characterization of Protein Folding using Monte Carlo Methods*, Biophys J 106, 260a (2014)
20. Setzler J., Brieg M., Wenzel W. *Assessment of Nonpolar Terms in Implicit Solvent Models to Estimate Small Molecule Hydration Free Energies*, Workshop on Computer Simulation and Theory of Macromolecules 2014, Hünfeld